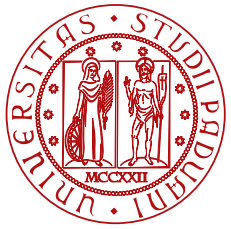

UNIVERSITÀ
DEGLI STUDI
DI PADOVA

MASTER THESIS IN PHYSICS

Andreev Scattering and Chirality Blockade in Weyl Semimetals

MASTER CANDIDATE

Brian Moglia

Student ID 2058318

SUPERVISOR

Prof. Luca Dell'Anna

University of Padova

CO-SUPERVISOR

Dott. Francesco Buccheri

Politecnico di Torino

ACADEMIC YEAR
2023/2024

Abstract

The study of topological effects in quantum materials has been one of the hottest research topics in condensed matter physics in recent years. Thanks to their high degree of tunability, such systems can even be used to study, from a condensed matter point of view, particles that have never been observed in high energy physics experiments, such as *Weyl fermions*. In particular, this thesis is focused on 3D materials known as Weyl semimetals, that under suitable conditions present a *vanishing bulk gap* in a finite number of points (the so-called Weyl nodes) and peculiar topological surface states known as Fermi arcs. Weyl systems exhibit a variety of interesting features, like the equivalent of the field theory Adler-Bell-Jackiw anomaly (here known as *Chiral anomaly*) and many related phenomena, such as negative magnetoresistence, anomalous Hall effect, and non-local transport.

The focus of this work is on the transport properties of these materials. We will concentrate on the analytical description of a junction between a Weyl semimetal and a BCS superconductor, with particular emphasis on the Andreev reflection process. The latter is anticipated to be strongly dependent on the orientation angle of the Weyl nodes relative to the junction plane. Specifically, Andreev reflection is not expected to occur for Weyl nodes that are parallel to the junction plane, due to the topological properties of the materials, a phenomenon known as the *Chirality Blockade*.

The thesis is structured into four main sections: the first section outlines the foundational concepts we will exploit, including basic principles of topology in physics, introduction of the Berry parameters, the Weyl fermions Hamiltonian, definition of Weyl semimetals and their topological properties, the most renown materials that present Weyl semimetals characteristics, along with a review of standard BCS theory and an introduction to the BTK model for junction description, with the most famous results. The second section reviews the existing literature on the subject, with a particular focus on what was done in two papers and highlighting the main differences of our approach. The third section offers a detailed analytical exposition of the model that we derived, in order to provide the theoretical background and notation necessary to understand the results. We exploit a four-band model Hamiltonian to represent both the Weyl semimetal and the superconductor, which, within the Bogoliubov-de Gennes framework, is characterized by eight degrees of freedom. Subsequently, we apply a unitary transformation to render the Weyl semimetal Hamiltonian block-diagonal. Next, we extend the previous work to accommodate any orientation of Weyl nodes relative to the junction interface and with that we establish the matching conditions necessary to derive the Transfer Matrix that connects all incoming and outgoing wavefunctions. This results in a linear system of equations, the solution of

which provides the probability of each process to occur. The concluding section focuses on presenting and interpreting the results and drawing final insights. Specifically, we will demonstrate how the probability of each process varies with the orientation of Weyl nodes and the impurity potential at the interface. We will highlight the existence of the chirality blockade effect, which leads to the total suppression of the Andreev reflection probability. This allows us to determine a critical angle beyond which the chirality blockade becomes effective. With these results, we will explore potential applications of this type of junction and the resulting emergent phenomena.

Contents

1 Introduction

1.1 Notions of Topology in Physics

Topological phases possess a property to which an integer-valued parameter can be assigned, which remains solely based on global characteristics in which phases cannot be altered by local perturbations such as disorder and scattering. The integer linked to a specific topological phase is termed a **topological invariant**. The chronologically first and most renowned example of a topological phase is the integer quantum Hall effect. This involved a system of electrons moving in two dimensions under a strong perpendicular magnetic field (a time-reversal broken system). This resulted in the quantisation of the transverse conductance of the system. It was soon understood that this effect had a topological explanation the physically measured transverse current was associated with a topological invariant, the first Chern number, which is the integral of the Berry curvature over the Brillouin zone. The topological phase on each plateau was safeguarded by a bulk gap, and the current was carried by metallic surface or edge states [6]. However, it has been recently recognized that gaplessness is *not* a necessary condition for topological protection. Band topology can be defined even if the gap closes at certain points in the Brillouin zone. An example of such a phase is the Weyl semi-metal phase, first predicted in the pyrochlore iridates [33]. This represents a new state of matter, whose low-energy excitations are Weyl fermions. Unlike topological insulators, these materials exhibit gapless states both in the bulk and at the surface.

Various classes of topological phases are characterized by different topological indices, such as the Chern number, which will be formally introduced in Section 1.1.2. The Chern

number can be likened to the *genus* of a closed surface. The genus of a closed manifold intuitively represents "the number of holes" in a shape. For instance, a sphere has a genus of 0, a doughnut has a genus of 1, and a pretzel has a genus of 3, as illustrated in Figure 1.1.

Figure 1.1: Genus illustration as the "number of holes" in closed manifolds. Figure from [31].

An essential theorem in topology states that the genus of these topological objects remains unchanged under any continuous transformation. Hence, the "number of holes" in these baked goods serves as a primary example of a topological invariant.

To better understand all this, let us start by introducing some mathematical objects that will help us understand what topological phases are.

1.1.1 BERRY PHASE, POTENTIAL AND CURVATURE

Let us examine a generic time-dependent Schrödinger problem, where both the Hamiltonian and the state are functions of a vector in a parameter space $\mathbf{R}(t)$, where the time dependence is sufficiently smooth. The time-dependent Schrödinger equation is

$$i\hbar\frac{d}{dt}|\Psi(t)\rangle = \hat{H}(\mathbf{R}(t))|\Psi(t)\rangle \tag{1.1}$$

where H has the eigensystem

$$\hat{H}(\mathbf{R})\,|\Phi_n(\mathbf{R})\rangle = E_n(\mathbf{R})\,|\Phi_n(\mathbf{R})\rangle \tag{1.2}$$

where $|\Phi_n(\mathbf{R})\rangle$ are generic wavefunctions in parameter space $\mathbf{R}$ and with band index n. Following [6], we rewrite the state $|\Psi\rangle$ as

$$|\tilde{\Psi}(t)\rangle = \sum_n C_n(t)e^{-\frac{iT}{\hbar}\int_0^t dt' E_n(\mathbf{R}_{t'})}\,|\Phi_n(\mathbf{R}_t)\rangle \tag{1.3}$$

Then it is a matter of writing down the time evolution of the C coefficients, which is found to be

$$\dot{C}_n(t) = i\dot{\gamma}_n(t)C_n(t) + \sum_{m\neq n}(\ldots) \tag{1.4}$$

where γ_n is a real quantity called **Berry phase** defined as

$$\gamma_n(t) = i\int_0^t dt'\dot{\mathbf{R}}_{t'}\langle\Phi_n(\mathbf{R}_{t'}|\nabla_R\Phi_n(\mathbf{R}_{t'})\rangle \tag{1.5}$$

Then it can be shown that [6], if the evolution is **adiabatic** and the gap between eigenvalues is preserved, the final state is proportional to the initial state, up to a phase factor. Explicitly, we have

$$|\Psi(t)\rangle \approx e^{i\gamma_0(t)}e^{-\frac{i}{\hbar}\int_0^t dt' E_0(\mathbf{R}(t'))}|\Phi_0(\mathbf{R}(t))\rangle \tag{1.6}$$

where $\gamma_0(t)$ has the form we stated before. This is what we call a *geometrical phase* factor, as it is independent from the parametrization of the curve described by $\mathbf{R}(t)$. Let's define the **Berry vector potential**

$$\mathbf{A}_n(\mathbf{R}) = i\langle\Phi_n(\mathbf{R})\mid\nabla_{\mathbf{R}}\Phi_n(\mathbf{R})\rangle \tag{1.7}$$

that depends on the phase we choose for $|\Phi_n(\mathbf{R})\rangle$ in the same way the magnetic potential depends on the gauge choice:

$$\left|\Phi_n'(\mathbf{R})\right\rangle = e^{-i\Lambda(\mathbf{R})}|\Phi_n(\mathbf{R})\rangle \quad \rightarrow \quad \mathbf{A}_n' = \mathbf{A}_n + \nabla_{\mathbf{R}}\Lambda(\mathbf{R}) \tag{1.8}$$

which becomes irrelevant if we move on a closed loop. Therefore, *on a closed path the Berry potential and the Berry phase are gauge-invariant.*

We now define the so-called **Berry curvature** as

$$\begin{aligned}\Omega^n_{\alpha\beta}(\mathbf{R}) &= -2\,\mathrm{Im}\left\langle\partial_\alpha\Phi_n(\mathbf{R})\mid\partial_\beta\Phi_n(\mathbf{R})\right\rangle \\ &= i\left[\left\langle\partial_\alpha\Phi_n(\mathbf{R})\mid\partial_\beta\Phi_n(\mathbf{R})\right\rangle - \left\langle\partial_\beta\Phi_n(\mathbf{R})\mid\partial_\alpha\Phi_n(\mathbf{R})\right\rangle\right]\end{aligned} \tag{1.9}$$

which has the parallel meaning of the Magnetic field. This is evident in three dimensions, where one can rewrite the Berry curvature as

$$\Omega_n(\mathbf{R}) = \nabla_{\mathbf{R}}\times\mathbf{A}_n(\mathbf{R}) \tag{1.10}$$

which is also manifestly gauge invariant since it holds the identity

$$\nabla_{\mathbf{R}}\times\nabla_{\mathbf{R}}\Lambda(\mathbf{R}) = 0.$$

Now, the Berry phase can be written as a surface integral of the Berry curvature using Stokes theorem

$$\gamma_n = \oint_{\mathscr{C}=\partial\mathscr{S}} d\mathbf{R}\cdot\mathbf{A}_n(\mathbf{R}) = \int_{\mathscr{S}} d\Sigma\cdot\Omega_n(\mathbf{R}) \tag{1.11}$$

where $\mathscr{S}$ is an arbitrary surface enclosed by the path $\mathscr{C}$.

1.1.2 CHERN NUMBER

Let $\mathscr{M}$ be a generic **closed** manifold, the Chern number is defined as

$$\mathrm{Ch} := \frac{1}{2\pi}\int_{\mathscr{M}} d\Sigma\cdot\Omega_n(\mathbf{R}) = n \in \mathbb{Z} \tag{1.12}$$

If we perturb the system via an adiabatic transformation, the Chern number cannot change and therefore, being an interger, it is called a **topological invariant** and it is used to probe in which topological phase we are in, with $\mathrm{Ch} = 0$ usually being labelled as the trivial phase.

1.1.3 THE NON-DEGENERATE BAND CROSSING

Consider the Hamiltonian

$$H = d\cdot\sigma = d_x\sigma^x + d_y\sigma^y + d_z\sigma^z \tag{1.13}$$

with $d = d(\mathbf{k})$ in three dimensions. The eigenvalues are of the form

$$E_\nu(d) = \nu d$$

where $d = |d|$ and $\nu = \pm$ is a band index. It describes a generic situation in which there is a *non-degenerate* level crossing with three parameters to tune to close the band gap.

We can write the Berry curvature in the vector d components as

$$\Omega_{d_a d_b} = \frac{1}{2d^3}\varepsilon_{abc}d_c \tag{1.14}$$

We can easily define a vector

$$\begin{aligned}\Omega_a &= \frac{1}{2}\varepsilon_{abc}\Omega_{k_a k_b} = \frac{d_a}{2d^3} \\ \Omega &= \frac{\hat{d}}{2d^2}\end{aligned} \tag{1.15}$$

I there exists a point such that $d = 0$, the last equation represents the field generated by a **monopole** in d parameter space of strength $\frac{1}{2}$.

Integrating the Berry curvature on a closed sphere around the monopole, as we have just seen, one obtains the Chern number $\rightarrow$ Ch $= 1$.

1.1.4 Explicit example with a Magnetic system

As we said, the Berry potential and curvature mathematically resemble magnetic potential and field.

Let's start from the Hamiltonian of a spin $1/2$ electron in a magnetic field

$$\hat{H}(\mathbf{R}(t)) = g\mu_B \hat{\mathbf{S}} \cdot \mathbf{B}(t) := \mathbf{R}(t) \cdot \vec{\sigma} \tag{1.16}$$

where $\mathbf{R}(\mathbf{t})$ absorbs the coefficients. Now we express $\mathbf{R}$ using spherical coordinates and write down the eigenstates of the spin in direction $\mathbf{R}$ as

$$\left|\Phi_{+1/2}(\mathbf{R})\right\rangle = \begin{pmatrix} \cos\theta/2 \\ e^{i\phi}\sin\theta/2 \end{pmatrix} \quad \left|\Phi_{-1/2}(\mathbf{R})\right\rangle = \begin{pmatrix} e^{-i\phi}\sin\theta/2 \\ -\cos\theta/2 \end{pmatrix} \tag{1.17}$$

These expressions are valid near the North pole ($\theta = 0$) but singular at $\theta = \pi$ due to the undetermined exponential in ϕ. We now calculate the Berry potential in both cases, using spherical coordinates.

$$\mathbf{A} = A_R\hat{\mathbf{R}} + A_\theta\hat{\theta} + A_\phi\hat{\phi} \tag{1.18}$$

From its definition, we obtain

$$\mathbf{A}^N_\pm = \left(0, 0, \mp\frac{1-\cos\theta}{2R\sin\theta}\right) \quad \mathbf{A}^S_\pm = \left(0, 0, \pm\frac{1+\cos\theta}{2R\sin\theta}\right) \tag{1.19}$$

each possessing a vortex at the southern (-) and northern (+) poles. In three dimensions, we can easily compute the Berry curvature as the curl of $\mathbf{A}$, leading to

$$\Omega_\pm = \mp\frac{1}{2}\frac{\hat{\mathbf{R}}}{R^2} \tag{1.20}$$

which has a singularity at the origin and is regular everywhere else, exactly matching the result in Eq. (1.15) of the previous section.

Now, this represents the expected magnetic monopole, i.e. the flux of the magnetic field exiting from such an object through a spherical surface satisfies $\nabla \cdot B = 4\pi q_M \delta(\mathbf{R})$ with $q_M = \pm\frac{1}{2}$ being the "magnetic charge" of the monopole.

Again, integrating this on a sphere around the monopole, one obtains the Chern number $\rightarrow \text{Ch} = \frac{4\pi q_M}{2\pi} = \pm 1$, analogously with the d-space generic case..

1.2 WEYL SEMIMETALS

1.2.1 SEMIMETALS DEFINITION

We shall start this section by defining the main properties of semimetals. Metals are known for their gapless energy bands and a non-zero density of states (DOS) at the Fermi energy, whereas semiconductors and insulators exhibit a gap in both the DOS and energy bands around the Fermi energy. In contrast, semimetals have, at least at some points in momentum space, gapless energy bands (like metals), but feature zero DOS at the Fermi level (like semiconductors and insulators). A schematic representation is depicted in Figure 1.2.

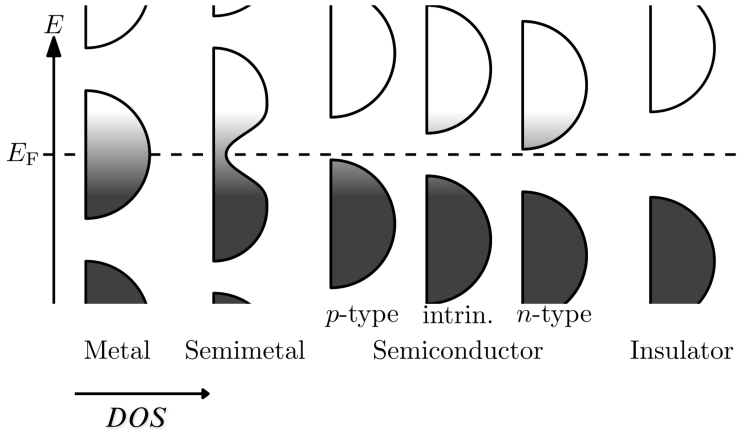

Figure 1.2: A comparison of the density of states (DOS) of different materials. E_F is the Fermi energy. From [34].

For 3D semimetals, the DOS usually vanishes at the Fermi energy following a parabolic power law. As previously stated, Weyl semimetals are materials that exhibit a gapless energy spectrum at a finite number of points in momentum-space, referred to as Weyl nodes,

where the DOS also vanishes. Particles with energies close to these Weyl nodes behave like Weyl fermions, which have never been observed in high energy physics experiments.

Before delving into the study of 3D Weyl semimetals, it is beneficial to recall the concept of a Weyl fermion.

1.2.2 THE WEYL EQUATION

Let's start from the Dirac equation

$$(\not{\partial} + m)\Psi = 0 \tag{1.21}$$

where Ψ is a Dirac spinor living in a 4-dimensional space S which naturally splits into two invariant subspaces

$$W_{\pm} = \frac{1 \pm \gamma^5}{2} S \tag{1.22}$$

whose elements are called Weyl spinors. Hence, we can depict the Dirac spinor in a chiral representation:

$$\Psi = \begin{pmatrix} \phi \\ \chi \end{pmatrix} \tag{1.23}$$

γ^5 is called the chirality operator, because its eigenstates are precisely the two Weyl spinors and its eigenvalues are ± 1, the associated chiralities. This is easily seen from the form of the operator

$$\gamma^5 = \begin{pmatrix} \mathbf{I} & 0 \\ 0 & -\mathbf{I} \end{pmatrix} \tag{1.24}$$

where $\mathbf{I}$ is the 2x2 identity.

In the chiral representation the Dirac equation is expressed as a system of two coupled equations for Weyl spinors:

$$\begin{aligned} i(\partial_0 - \boldsymbol{\sigma} \cdot \partial)\,\phi &= m\chi \\ i(\partial_0 + \boldsymbol{\sigma} \cdot \partial)\,\chi &= m\phi \end{aligned} \tag{1.25}$$

In the **zero-mass limit** the two equations decouple, and we obtain a pair of independent Weyl equations:

$$\begin{aligned} i(\partial_0 - \sigma\cdot\partial)\,\phi = 0 \\ i(\partial_0 + \sigma\cdot\partial)\,\chi = 0 \end{aligned} \tag{1.26}$$

Once we move to momentum space, the Hamiltonian for each Weyl equation takes the form:

$$H_\pm = \mp\vec{p}\cdot\vec{\sigma} \tag{1.27}$$

Thus Weyl fermions propagate parallel (or antiparallel) to their spin, which defines their helicity, which, for massless particles, is the same as their chirality.

It now becomes evident that this formulation exactly corresponds to the form previously seen in Eq. (1.13) for generic d-space parameters. Consequently, an intriguing connection between Dirac theory and condensed matter physics emerges. If we succeed in engineering a system in which the Hamiltonian locally takes the form of the Weyl Hamiltonian, likely some *topological phenomena* will arise.

1.2.3 Symmetries in Dirac-like Hamiltonians

This part focuses on highlighting the primary differences that may arise in materials characterized by Dirac-like Hamiltonians.

We can formulate Dirac-like Hamiltonians in the notation of γ matrices, which has the advantage that it is independent from the representation and the attached physical meaning (spin and orbital degrees of freedom). We start from the Dirac Lagrangian

$$L_D = \bar{\Psi}\left(i\gamma^\mu\partial_\mu - m\right)\Psi \tag{1.28}$$

where $\bar{\Psi} = \Psi^\dagger\gamma^0$ and the γ matrices satisfy the algebra

$$\{\gamma^\mu,\gamma^\nu\} = 2\eta^{\mu\nu} \tag{1.29}$$

with metric $\eta = \mathrm{diag}(1,-1,-1,-1)$. The corresponding Hamiltonian is

$$H = \int d^3\mathbf{r}\Psi^\dagger\left[\sum_j i\gamma^0\gamma^j\partial_j + m\gamma^0\right]\Psi \tag{1.30}$$

Following [27], parity P is a unitary operator that inverts momentum and space coordinates (they are vectors), but not spin (it is a pseudovector) of an electron. It is implemented by a complex phase η satisfying $\eta\eta^* = 1$ and by the matrix γ^0

$$P\Psi(t,\mathbf{r})P = \eta\gamma^0\Psi(t,-\mathbf{r}) \tag{1.31}$$

We note in passing that anti-fermions receive an extra -1 under parity . Time reversal is an **antiunitary** operator that flips the spin and the sign of the momentum, but not of the space coordinate. Defining a spin-up and -down spinor $\xi^{\pm}$, one can flip the spin using

$$\xi^{-s} = -i\sigma^y K\xi^s \tag{1.32}$$

where K implements complex conjugation. Time-reversal on the Dirac bi-spinor is implemented by the matrix $-\gamma^1\gamma^3$ and acts on the full Dirac field as

$$T\Psi(t,\mathbf{r})T = -\gamma^1\gamma^3\Psi(-t,\mathbf{r}) \tag{1.33}$$

FInally, charge conjugation takes a particle with a given spin orientation and momentum to a hole with the same spin orientation and momentum. It acts as

$$C\Psi(t,\mathbf{r})C = -i\gamma^2 K\Psi(t,\mathbf{r}) = -i\gamma^2\left[\Psi^\dagger(t,\mathbf{r})\right]^T = -i\left[\bar{\Psi}\gamma^0\gamma^2\right] \tag{1.34}$$

The following table shows the result of C, P and T on some of the most common Lagrangian terms:

	$\bar{\Psi}\Psi$	$i\bar{\Psi}\gamma^5\Psi$	$\bar{\Psi}\gamma^\mu\Psi$	$\bar{\Psi}\gamma^\mu\gamma^5\Psi$	∂_μ	$\bar{\Psi}\gamma^\mu\partial_\mu\Psi$	$\bar{\Psi}\sigma^{\mu\nu}\Psi$
P	+1	-1	$(-1)^\mu$	$-(-1)^\mu$	$(-1)^\mu$	+1	$(-1)^\mu(-1)^\nu$
T	+1	-1	$(-1)^\mu$	$(-1)^\mu$	$-(-1)^\mu$	-1	$-(-1)^\mu(-1)^\nu$
C	+1	+1	-1	+1	+1	-1	-1
CPT	+1	+1	-1	-1	-1	+1	+1

With the notation

$$\sigma^{\mu\nu} = \frac{i}{2}[\gamma^\mu,\gamma^\nu] \tag{1.35}$$

and

$$(-1)^\mu \equiv \begin{cases} +1 & \mu = 0 \\ -1 & \mu = 1,2,3 \end{cases} \tag{1.36}$$

We see that the Hamiltonian (1.30) is even under inversion and also under time reversal. The mass term is even with respect to T and P. Following [14], we add the axial vector perturbation $\bar{\Psi}\gamma^\mu\gamma^5\Psi$, so that the Hamiltonian takes the form

$$H = \int d^3\mathbf{r}\Psi^\dagger \left[-\sum_j i\gamma^0\gamma^j\partial_j + m_0\gamma^0 + b_\mu\gamma^0\gamma^\mu\gamma^5 \right] \Psi \tag{1.37}$$

Now, let us rewrite this in the Weyl (or chiral) representation

$$\begin{aligned} &\gamma^0 = \tau^x \quad \gamma^j = -i\tau^y\sigma^j \\ &\gamma^5 \equiv i\gamma^0\gamma^1\gamma^2\gamma^3 = i\tau^x\left(-i\tau^y\right)^3\sigma^x\sigma^y\sigma^z = \tau^z \end{aligned} \tag{1.38}$$

The parity operation is written in the Weyl representation as

$$P\Psi(t,\mathbf{r})P = \gamma^0\Psi(t,-\mathbf{r}) = \tau^x\Psi(t,-\mathbf{r}) \tag{1.39}$$

Time-reversal is represented as

$$T\Psi(t,\mathbf{r})T = -\gamma^1\gamma^3\Psi(-t,\mathbf{r}) = i\sigma^y\Psi(-t,\mathbf{r}) \tag{1.40}$$

and charge conjugation is represented as

$$C\Psi(t,\mathbf{r})C = -i\gamma^2K\Psi(t,\mathbf{r}) = -\tau^y\sigma^y\Psi^*(t,\mathbf{r}) \tag{1.41}$$

With $b = (b_0, \mathbf{b})$, the Hamiltonian in the chiral representation reads

$$H = \tau^z\left[\sigma\cdot(\mathbf{k}) + b_0\right] + m_0\tau^x + \sigma\cdot\mathbf{b} \tag{1.42}$$

In matrix form, this is

$$H = \begin{pmatrix} H_+(\mathbf{k}, b_0, \mathbf{b},) & m_0 \\ m_0 & H_-(\mathbf{k}, b_0, \mathbf{b}) \end{pmatrix} \tag{1.43}$$

where

$$\begin{aligned} &H_+(\mathbf{k}, b_0, \mathbf{b}) = (\mathbf{k}+\mathbf{b})\cdot\sigma + b_0 \\ &H_-(\mathbf{k}, b_0, \mathbf{b}) = -(\mathbf{k}-\mathbf{b})\cdot\sigma - b_0 = -H_+(\mathbf{k}, b_0, -\mathbf{b}) \end{aligned} \tag{1.44}$$

where here the $\pm$ signs stand for high- and low-energy bands respectively. With this notation, it also becomes evident that the $\sigma\cdot\mathbf{b}$ term has the form of the spin-orbit coupling (SOC) we already encountered in Eq. (1.16).

Time reversal acts as

$$\begin{aligned} T\left[H\left(\mathbf{k},b_0,\mathbf{b}\right)\right] &= \sigma_y H^*\left(-\mathbf{k},b_0,\mathbf{b}\right)\sigma_y = \tau^z\left[\sigma\cdot\left(\mathbf{k}\right)+b_0\right]+m_0\tau^x-\sigma\cdot\mathbf{b} \\ &= H\left(\mathbf{k},b_0,-\mathbf{b}\right) \end{aligned} \tag{1.45}$$

as we can see, if $\mathbf{b}\neq 0$ time-reversal symmetry is broken.

Instead, for the parity operation, one obtains

$$\begin{aligned} P\left[H\left(\mathbf{k},b_0,\mathbf{b}\right)\right] &= \tau_x H\left(-\mathbf{k},b_0,\mathbf{b}\right)\tau_x = \tau^z\left[\sigma\cdot\mathbf{k}-b_0\right]+m_0\tau^x-\sigma\cdot\mathbf{b} \\ &= H\left(\mathbf{k},-b_0,\mathbf{b}\right) \end{aligned} \tag{1.46}$$

which means that if $b_0\neq 0$ inversion symmetry is broken.

By tuning the parameters m_0, b, b_0 in the Hamiltonian (1.42), one can see the emergence of different types of materials satisfying different symmetries. In Figure 1.3, the energy bands for some examples of possible configurations of parameters m_0, b, b_0 are plotted.

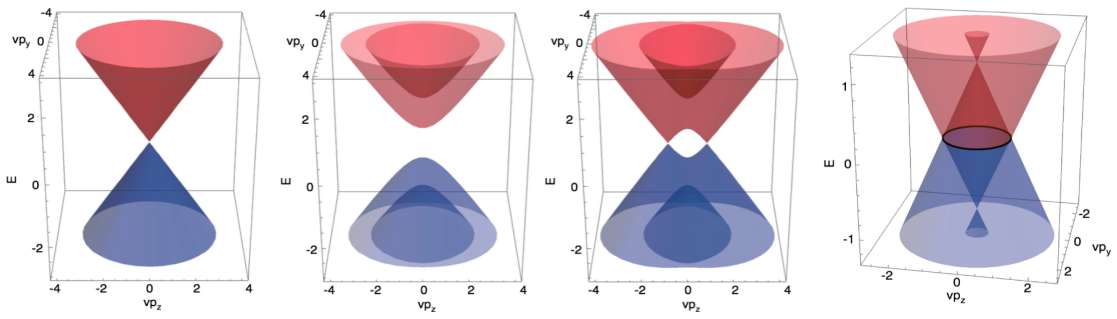

Figure 1.3: (left to right) Energy spectra for the Dirac semimetal ($m_0 = b = b_0 = 0$), magnetic semiconductor ($m_0 = 1, b = 0.5, b_0 = 0$), Weyl semimetal ($m_0 = 0.5, b = 1, b_0 = 0$), and nodal-line semimetal ($m_0 = 0, b = 0, b_0 = 1$) for the Hamiltonian in Eq. (1.42). From [18].

We see that the generic effect of having $m_0 \neq 0$ is to open a gap between the energy bands farther away from the Fermi energy and those closer to it. Then, in the case where $b < m_0$ one obtains a semiconductor (here labelled as "magnetic" due to the fact that the $\sigma\cdot\mathbf{b}$ term is of the form of a SOC), while for the case in which $b > m_0$, one has two distinct non-degenerate band crossing points (i.e. gapless energy spectrum) separated by a distance of $\Delta k_W = 2\sqrt{b^2-m_0^2}$. This type of materials are a first example of what we will refer to as *Weyl semimetals* (WSM). Other types of semimetals can be obtained, for example the nodal-line semimetals (right panel in Figure 1.2) which exhibit a closed "line" of points in which the energy gap closes, and Dirac semimetals (left panel in Figure 1.2) that exhibit degenerate points in which the energy gap closes, i.e. degenerate energy bands for the H_+ and H_- blocks of the Hamiltonian.

1.2.4 WEYL SEMIMETALS DEFINITION

In the previous section, we have seen an example of a model that is able to show two non-degenerate points in which the energy bands touch. As already mentioned, Weyl semimetals are defined to be topological materials in which there is a finite number (usually much larger than 2) of these band touching points. But we still have not explained what happens around this points and why we refer to them as topological materials.

To answer the first question, we can discuss the generic dispersion near the band touching points $\pm k_W$. Any generic 2x2 Hamiltonian can be written in the form

$$H(\mathbf{k}) = d_0\ \sigma_0 + d\cdot\sigma = d_0\ \sigma_0 + d_x\sigma^x + d_y\sigma^y + d_z\sigma^z \tag{1.47}$$

where each component is $d_j = d_j(\mathbf{k})$ for $i = x,y,z$ (in 3D) and d_0 represents a chemical potential term, which we set to $d_0 = 0$ for the moment. We can perform an expansion around the band touching point $\mathbf{k} = \delta\mathbf{k} + \mathbf{k}_W$, which gives

$$H(\mathbf{k}) \sim \sum_{j=x,y,z} \mathbf{v}_j\cdot\delta\mathbf{k}\ \sigma_j \tag{1.48}$$

where $\mathbf{v}_j = \nabla_k d_j(\mathbf{k})\big|_{\mathbf{k}=\mathbf{k}_W}$ (with $j = x,y,z$) are effective velocities which are typically nonvanishing in the absence of additional symmetries. We see that around $\mathbf{k}_W$ the Hamiltonian is linear in $\delta\mathbf{k}$ and vanishes for $\mathbf{k} = \mathbf{k}_W \to \delta\mathbf{k} = 0$. This means that around the band touching points, Hamiltonians of the form (1.48) describe particle behaving as *Weyl fermions*. From now on, let us therefore refer to these points as **Weyl nodes**. This is still not enough to define a Weyl semimetal. Indeed, Weyl nodes can be found in other materials like Dirac semimetals (in 3D) and graphene-like materials (in 2D).

We have seen in the previous model Hamiltonian (1.42), that the case when $m = b = b_0 = 0$ corresponds to the so-called Dirac semimetal, which is composed of a pair of degenerate linear bands, therefore with two degenerate Weyl nodes at $\mathbf{k} = \mathbf{k}_W = 0$. We note that in this limit, both P and T symmetries are preserved. Instead, if we break, for example, T-reversal symmetry by adding a SOC perturbation like $\mathbf{b}\cdot\sigma$ (see Eq. (1.16)), the two degenerate bands become split into two, therefore showing two different Weyl nodes at the momenta $\mathbf{k} = \pm\mathbf{k}_W \neq 0$. It can be shown that the appearance of a finite number of Weyl nodes can be achieved also by breaking P [24].

Therefore, we include in the definition of Weyl semimetals the fact that they are materials in which either T or P are broken or, more generally, the Weyl Hamiltonian is not invariant under the combined transformation TP.

1.2.5 TOPOLOGICAL PROPERTIES OF WEYL SEMIMETALS

We still have not answered why Weyl semimetals are defined as topological materials. The Berry flux piercing any surface enclosing a Weyl node at $\mathbf{k}_W$ is what we defined as Chern number. For any Hamiltonian like the one in Eq. (1.48), the Chern number takes the form

$$\mathrm{Ch} = \mathrm{sign}\,(\mathbf{v}_x \cdot \mathbf{v}_y \times \mathbf{v}_z) \tag{1.49}$$

If we consider the sphere surrounding a Weyl node at $|\mathbf{k}| = \pm k_W$, it has a non-vanishing Chern number $\mathrm{Ch} = \pm 1$. In Figure 1.4 there is a plot of the Chern number in a region with two Weyl points.

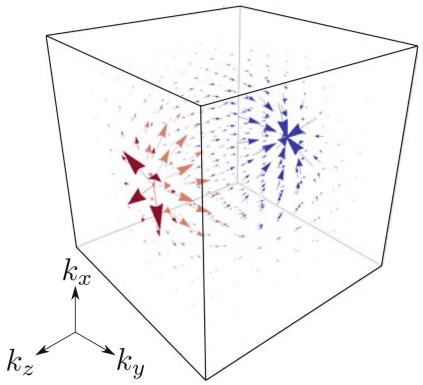

Figure 1.4: Berry fluxes around Weyl points of opposite chiralities.

However, it is possible to show that a closed surface covering the entire Brillouin zone *must have net Chern number zero* [1]. Therefore, the net Chern number of all Weyl points in the Brillouin zone must vanish. The Berry phase

$$\gamma_n = \int_{S_{BZ}} d^2\Sigma_{\mathbf{k}} \cdot \Omega_n(\mathbf{k}) = 0 \tag{1.50}$$

over the Brillouin zone (BZ) vanishes, but can be expressed as an integral over the surfaces of the excluded volumes (see Figure 1.5)

$$\gamma_n = \sum_i \oint_{\partial U_i} d\Sigma_{\mathbf{k}} \cdot \Omega_n(\mathbf{k}) = -2\pi \sum_i C_i \tag{1.51}$$

which must vanish to match the previous equation.

[1] see for example [35], page 10.

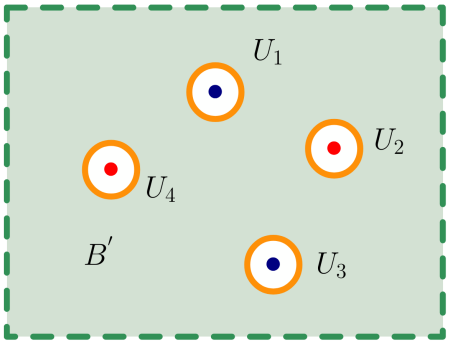

Figure 1.5: BZ depiction for the integral domain in Eq. (1.51). The orange circles are the closed contours defined as ∂U_i, which in a 3D scheme would represent the surface of the spheres enclosing Weyl nodes. The dots are indeed the Weyl nodes, with color matching their chirality.

Hence, in order to have the total chirality of the BZ equal to zero, we can state that **Weyl nodes always have to come in pairs**. This argument can be seen as a heuristic proof of the *Nielsen-Ninomiya theorem*. The theorem in a more complete form states that any local, Hermitian, and translationally invariant lattice action in even-dimensional spacetime possesses an equal number of left- and right-handed chiral fermions [25].

1.2.6 Robustness of Weyl Semimetals

Let us introduce a small perturbation to the system of the form

$$\Delta(\mathbf{k}) \cdot \sigma \tag{1.52}$$

It is evident that the action of this perturbation is just that of a shift of the position of the Weyl nodes that are now at $\mathbf{k}'_W = \mathbf{k}_W + \Delta(\mathbf{k})$ and we can still expand around $\mathbf{k} = \delta\mathbf{k} + \mathbf{k}'_W$, which gives

$$H(\mathbf{k}) \sim \sum_{j=x,y,z} \mathbf{v}'_j \cdot \delta\mathbf{k}\, \sigma_j \tag{1.53}$$

where now we have that $\mathbf{v}'_j = \nabla_k \left[d_j(\mathbf{k}) + \Delta_j(\mathbf{k}) \right] \big|_{\mathbf{k}=\mathbf{k}_W}$ (with $j = x,y,z$). We see that the Hamiltonian is still linear in $\delta\mathbf{k}$ and vanishes for $\mathbf{k} = \mathbf{k}'_W$.

The limiting case is when the perturbation reaches the value of $\Delta(\mathbf{k}) = -\mathbf{k}_W$, then we obtain that the Weyl nodes merge into one degenerate point at $\mathbf{k}'_W = 0$, i.e. we do not have a Weyl semimetal anymore, but we now in a Dirac semimetal phase.

Nevertheless, perturbations only caused by noise or impurities of this scale are highly improbable, whereas they can be induced by external magnetic fields that, via SOC, alter

the orientation and separation of the Weyl nodes. This is why we define Weyl semimetals to be **robust** under perturbations.

1.2.7 CHIRAL ANOMALY

The basic idea of the chiral anomaly is that the conservation laws $\partial_\mu j^\mu = 0$ and $\partial_\mu j_5^\mu = 0$ cannot be satisfied simultaneously. Now the axial vector current of the Dirac theory is given by, $J_5^\mu = \psi\gamma^\mu\gamma_5\psi$. So in a WSM with chiral symmetry, we should have $\partial_\mu J_5^\mu = 0$ and consequently, the conservation of chiral charge at the Weyl nodes. This charge, apart from a prefactor, is the Chern number C at that Weyl node in the WSM, i.e. a closed surface integral of Berry curvature in k-space around the Weyl node. The non-zero chiral charge is an outcome of the band touching at Weyl node and singularity of the Berry curvature there.

By coupling the Weyl fermions to an external electromagnetic field we obtain an effective "axionic" θ term in the action given by [18]

$$S_\theta = \frac{e^2}{32\pi^2}\int d^4x\theta(x)\varepsilon^{\mu\nu\alpha\beta}F_{\mu\nu}F_{\alpha\beta} \tag{1.54}$$

where the axion field $\theta(x) = 2b_\mu x^\mu = 2\mathbf{b}\cdot\mathbf{r} - 2b_0 t$ and $b_\mu = b_0, b_i$ are the parameters that break the parity (b_0) and time-reversal (b_i) that we have already encountered in the model Hamiltonian in the previous section. The action in Eq. (1.54) can be derived from the (4+1)-dimensional Chern-Simons action obtained from the electromagnetic coupling in Dirac Hamiltonians via the procedure of dimensional reduction, see [28]. The axial current for a single Weyl cone of chirality χ is given by

$$\partial_\mu \mathbf{j}_\chi^\mu = -\chi\frac{e^3}{4\pi^2\hbar^2}\mathbf{E}\cdot\mathbf{B}, \tag{1.55}$$

where E is an electric and B a magnetic field and thus the current would not be conserved when E and B have a parallel component. This obvious *contradiction to current conservation* can be resolved by considering the complete system consisting of pairs of Weyl cones of opposite chirality and hence, current conservation is restored in total, i.e.

$$\begin{gathered}\frac{\partial}{\partial t}(n_R + n_L) = 0, \Longrightarrow \frac{\partial}{\partial t}(n_R - n_L) \neq 0 \\ \frac{\partial}{\partial t}(n_R - n_L) = \pm\frac{e^2}{h^2}\mathbf{E}\cdot\mathbf{B}\end{gathered} \tag{1.56}$$

where n_R and n_L denote the number of fermions at the right and left chirality Weyl nodes. This implies that by applying parallel electric and magnetic fields, we can change

the difference in their numbers, or if we really have an isolated Weyl node, we can *change the number of particles*. However, in any real system, one always has total particle number conservation. Due to the anomaly term, one obtains charge pumping between the nodes: n_R decreases and n_L increases or vice-versa, at a rate given by the anomaly. However, the total number of particles remains the same. If we had a single Weyl node, the chiral anomaly would increase the number of particles in the node and therefore charge conservation would be broken. However, by the previously announced Nielsen-Ninomiya theorem, Weyl nodes always have to come in pairs, and particle number conservation is preserved.

1.2.8 A COMPARISON WITH GRAPHENE

The study of Dirac physics in condensed matter systems gained renewed attention within the physics community following the well-known discovery of the exfoliation technique of graphene monolayers in 2004 [26]. It showed how a single two-dimensional (2D) sheet scratched off a non-conducting three dimensional (3D) graphite lump can show unique conducting properties such as large electron mobility, thermal conductivity or huge tensile strengths. A simplified Hamiltonian of such system can be constructed from a tight-binding model (by which electrons in an orbital localized around a lattice site can move/tunnel to a different orbital localized around an adjacent lattice site) consisting of nearest-neighbour hopping of electrons in the underlying *honeycomb lattice*. Dispersion near the band crossings of such monolayers is linear and results in **Dirac fermions** for the low energy excitations. Due to this point degeneracy between conduction and valence band, graphene is dubbed as a **semimetal**. Considering low-energy physics around these points, one comes up with a continuum model that resembles a *massless* Dirac Hamiltonian. Typically, a continuum model for graphene is given as $H = \hbar v_F (\sigma_x k_x + \sigma_y k_y)$. Like $S = 1/2$ spins with spin-up and spin-down eigenstates, here the σ 's have two eigenvectors corresponding to two sublattices of the honeycomb lattice of graphene and thus σ 's are called the *pseudo-spins*. For comparison, Weyl semimetals (WSMs) may be thought as 3D analogues of graphene, although a WSM has both gapless surface and bulk states, unlike graphene-based topological insulators. We have already seen that the dispersion spectrum of the 3D bulk WSM system have discrete k-points, called Weyl points (or nodes), is gapless. In addition to that, there are also *gapless conducting surface states*, localized only within the surface of the WSM. These surface states will be the topic of the next section.

The major difference between graphene-based 3D systems and WSMs emerges when we add a $\Delta\sigma_z$ term to the graphene Hamiltonian. The $\Delta \neq 0$ term can be induced, for

example, by an external electric field [15]. We see that the spectrum becomes **gapped out** due to inversion symmetry breaking. But in a 3D WSM, with generic bulk Hamiltonian $H = c_0(k)\sigma_0 + \sigma_x v_x p_x + \sigma_y v_y p_y + \sigma_z v_z p_z$, such gaping out is not possible, as degeneracies at Weyl nodes are accidental in nature. This, as we already pointed out, makes them more **robust**. One can only shift the position of those Weyl nodes, but they cannot be knocked out, unless pairs of nodes with opposite chiralities are made to coincide, as described by the Nielsen-Ninomiya theorem in Section 1.2.5.

1.2.9 Fermi Arcs

Surface states are typically associated with band insulators and exist within the bulk band gap, being exponentially localized near the surface. For gapless bulk systems like WSMs, we assume translational invariance and label surface states by crystal momenta within the 2D surface Brillouin zone (sBZ). We require regions of the sBZ free of bulk states at the same energy. Considering a pair of Weyl nodes at the chemical potential ($E_F = 0$) at momenta $\pm\mathbf{k}_W$ in the sBZ, surface states can exist at all momenta except at the projection of the Weyl points onto the sBZ (Figure 1.7 top left). At these points, surface states can leak into the bulk and are not well defined. At other energies, the momentum region occupied by bulk states grows (Figure 1.7 bottom). These bulk states enable surface states that are impossible in strictly 2D systems or on the surface of any 3D insulator with a finite energy gap throughout the Brillouin zone. We will not focus on the theoretical framework that describes these surface states, which can be found in many references, for example [1].

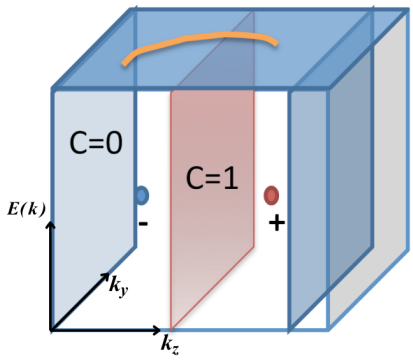

Figure 1.6: Fermi arcs connecting two opposite chirality Weyl nodes. The plane showing $C = 1$ is at $k_z = 0$, while those showing $C = 0$ are at $k_z = \pm\frac{\pi}{a}$. From [1].

The surface states all disperse in the same direction and inherit the chiral nature of the

Chern insulator edge states. Concurrently, the bulk Fermi surface now encloses a non-zero volume, and their projection onto the sBZ forms a pair of filled discs enclosing the Weyl node momenta. How do the Fermi arc surface states connect to the projection of the bulk Fermi surface? In the top right of Figure 1.7, a plot of both surface (pink) and bulk bands projected onto the sBZ is shown.

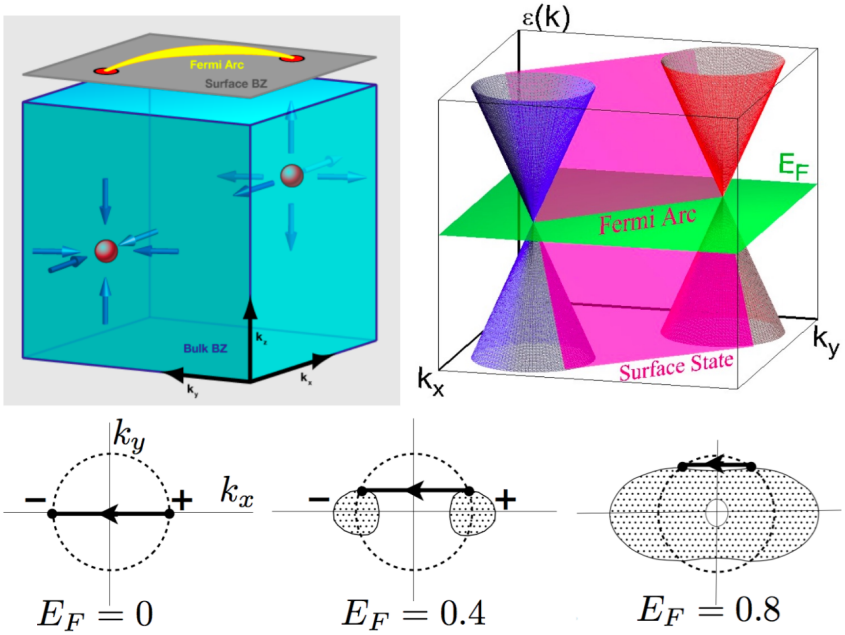

Figure 1.7: (top left) Chern number, Weyl points and surface Fermi arcs. (top right) Connection of surface states to bulk Weyl points. (bottom) Evolution of Fermi arc with chemical potential in a particular microscopic model on raising the chemical potential from the nodal energy ($E = 0$). Fermi arcs are tangent to the bulk Fermi surface projections, and may persist even after they merge into a trivial bulk Fermi surface. From [1].

1.2.10 MATERIALS

As discussed above, the appearance of a Weyl semimetal phase is possible only if the product of parity and time reversal is not a symmetry. One wants a material that is close to a band inversion transition and which breaks either T or P symmetry. However, unlike the case of some Dirac systems the existence of Weyl nodes is accidental which can make a systematic search for them challenging. Moreover, because the band touchings can occur at a generic momentum positions they can be over looked in band structure calculations.

INVERSION SYMMETRY BREAKING MATERIALS

A large number of materials that are WSMs through the inversion symmetry breaking mechanism have recently been predicted and discovered, such as TaAs,TaP, NbAs and NbP. Although such systems are predicted to have 24 Weyl points, this family of materials are completely stoichiometric without any additional doping, external strain or pressure needed to fine tune the state. Signatures of the Weyl state were seen by ARPES in TaAs and related materials soon afterwards. The node structure of the TaAs family is shown in Figure 1.8

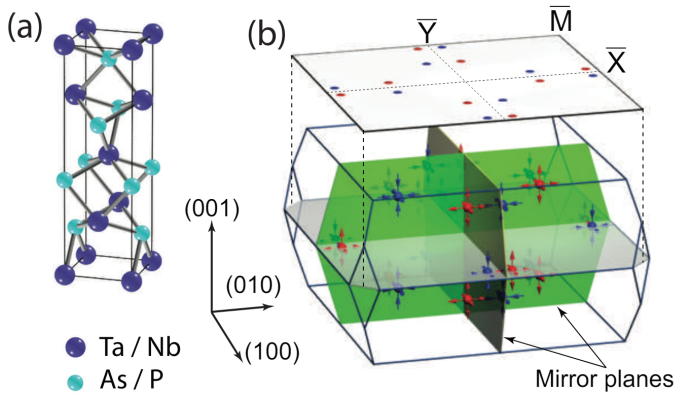

Figure 1.8: (a) Crystal structure of the non-centrosymmetric lattice in the TaAs-family of compounds. (b) The first Brillouin zone showing twelve pairs of Weyl points. The red and blue spheres represent the Weyl points with $C = \pm 1$ chirality. From [4]

Although these materials have been successfully realized, the quest for a more optimal family of WSM materials persists.. We note that the 24 Weyl nodes in the TaAs family of compounds give rise to potentially complicated transport and spectroscopic properties. Moreover, in the TaAs material class, all Weyl physics occur in a narrow range of energies. This requires careful material preparation to ensure the Fermi level falls in this range. In this regard, Weyl semimetals with larger characteristic energy scales are desirable.

TIME REVERSAL BREAKING (MAGNETIC) WEYL SEMIMETALS

An ongoing search has been for materials that are good examples of a WSM through the T breaking mechanism. Half Heusler compounds often exhibit magnetic ordering. The materials $X\mathrm{CrTe}(X = \mathrm{K}, \mathrm{Rb})$ studied here contain transition metal elements Cr, which possesses magnetic moment due to its partially filled $3d$ shell. With the inclusion of Spin-Orbit Coupling (SOC), the band structure will depend on the magnetization direction. The

SOC term will appear in the Hamiltonian in the form

$$H_{SOC} \simeq \boldsymbol{\sigma} \cdot \mathbf{B} \tag{1.57}$$

and, as discussed in the previous section, this term will break T-reversal symmetry, therefore leading to the creation of two separate Weyl nodes. This class of materials is therefore much better suited (compared to the 24 nodes TaAs class) for studying the transport properties of Weyl semimetals. The electronic bands of KCrTe for different magnetizations are shown below:

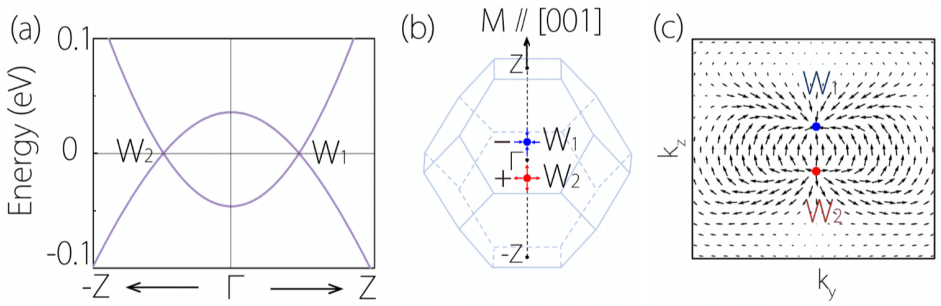

Figure 1.9: . (a) Band structure along $\Gamma - Z$ path. W_1 and W_2 are the two Weyl points. (b) Location of the Weyl points in the bulk Brillouin zone for magnetization along [001]. (c) Distribution of Berry curvature field in the $k_x = 0$ plane. From [20]

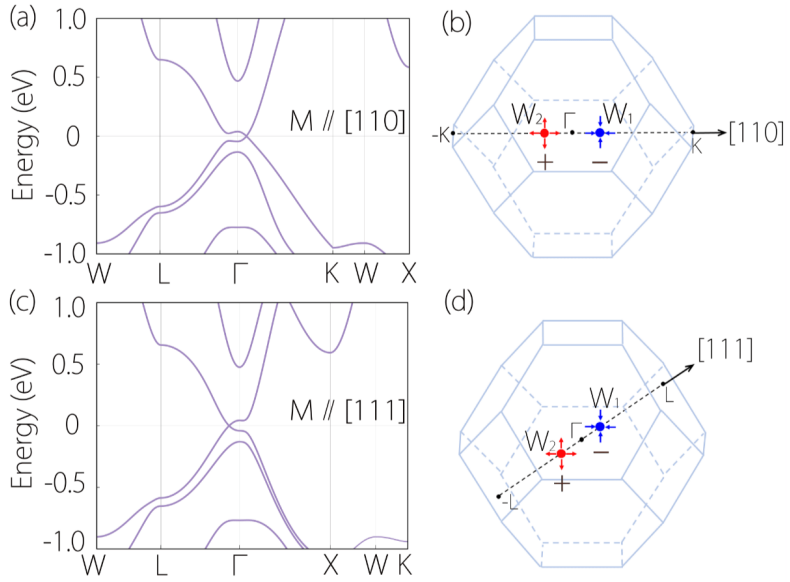

Figure 1.10: Band structures of KCrTe and distribution of the two Weyl points in BZ for magnetization vector along (a)-(b) [110] and (c)-(d) [111] directions. From [20]

From these results, we see that the position of the Weyl points can be flexibly moved by controlling the magnetization direction. This movement will also affect surface Fermi arcs as well as transport properties, as we will verify through this thesis.

In addition to this, the *X*CrTe class of materials exibits Weyl points which are exactly located at the Fermi level enforced by the band filling condition. In addition, there is no other trivial bands around the Fermi level, generating a 'clean' environment to study intrinsic Weyl features.

1.3 SUPERCONDUCTOR THEORY

1.3.1 BCS THEORY AND BOGOLIUBOV-DE GENNES FORMALISM

The Bogoliubov equations represent a formulation of the self-consistent mean field method for the description superconductors [36]. The presence of the impurities, the scattering centers, or the spatially varying interactions result in a position dependent Hamiltonian. These effects are included in the Hamiltonian via the spatially varying scalar potential $U(\mathbf{r})$ and the pairing potential $\Delta(\mathbf{r})$.

The Hamiltonian is given by

$$\hat{H} = \hat{H}_0 + \hat{H}_1 \tag{1.58}$$

where $\hat{H}_0$ denotes the kinetic energy operator and $\hat{H}_1$ denotes the interaction energy operator:

$$\begin{aligned} \hat{H}_0 &= \int d\mathbf{r} \sum_{\sigma} \hat{\Psi}^{\dagger}(\mathbf{r}\sigma) \left[\frac{1}{2m} \left(-i\hbar\nabla - \frac{e\mathbf{A}}{c} \right)^2 + U_0(\mathbf{r}) - \mu \right] \hat{\Psi}(\mathbf{r}\sigma) \\ \hat{H}_1 &= -\frac{1}{2} V \int d\mathbf{r} \sum_{\sigma\sigma'} \hat{\Psi}^{\dagger}(\mathbf{r}\sigma) \hat{\Psi}^{\dagger}\left(\mathbf{r}\sigma'\right) \hat{\Psi}\left(\mathbf{r}\sigma'\right) \hat{\Psi}(\mathbf{r}\sigma) \end{aligned} \tag{1.59}$$

Here, m is the mass of the Fermi liquid quasiparticles, $\mathbf{A}$ is the vector potential, e is the electric charge, c is the speed of light, $U_0(\mathbf{r})$ is the external potential due to the impurities, the scatterings from surfaces etc, μ is the chemical potential, σ denotes the spin direction and V is assumed to be the constant (BCS approximation) net interaction between quasiparticles (pairing interaction and Coulomb interaction). The Ψ s and $\Psi^{\dagger}$ s are the annihilation and the creation field operators obeying the fermion anticommutation rules and are given by

$$\begin{aligned} \hat{\Psi}(\mathbf{r}\sigma) &= \sum_{\mathbf{k}} e^{i\mathbf{k}\cdot\mathbf{r}} \hat{a}_{\mathbf{k}\sigma} \\ \hat{\Psi}^{\dagger}(\mathbf{r}\sigma) &= \sum_{\mathbf{k}} e^{-i\mathbf{k}\cdot\mathbf{r}} \hat{a}^{\dagger}_{\mathbf{k}\sigma} \end{aligned} \tag{1.60}$$

where we have assumed that the single particle states are plane waves in unit volume ($\mathcal{V} = 1$). In the superconducting state the excited states at a point $\mathbf{r}$ with spin $\uparrow$ or $\downarrow$ are a linear combination of electrons and holes, thus the field operators transform into

$$\begin{aligned}
\hat{\Psi}(\mathbf{r}\uparrow) &= \sum_n \left[\hat{\gamma}_{n\uparrow} u_n(\mathbf{r}) - \hat{\gamma}^\dagger_{n\downarrow} v^*_n(\mathbf{r})\right] \\
\hat{\Psi}(\mathbf{r}\downarrow) &= \sum_n \left[\hat{\gamma}_{n\downarrow} u_n(\mathbf{r}) + \hat{\gamma}^\dagger_{n\uparrow} v^*_n(\mathbf{r})\right], \\
\hat{\Psi}^\dagger(\mathbf{r}\uparrow) &= \sum_n \left[\hat{\gamma}^\dagger_{n\uparrow} u^*_n(\mathbf{r}) - \hat{\gamma}_{n\downarrow} v_n(\mathbf{r})\right] \\
\hat{\Psi}^\dagger(\mathbf{r}\downarrow) &= \sum_n \left[\hat{\gamma}^\dagger_{n\downarrow} u^*_n(\mathbf{r}) + \hat{\gamma}_{n\uparrow} v_n(\mathbf{r})\right]
\end{aligned} \tag{1.61}$$

where $\hat{\gamma}^\dagger_{n\uparrow}$ creates a quasiparticle in the state n with the spin up while $\hat{\gamma}_{n\downarrow}$ annihilates a quasiparticle with the spin down. These expressions are basically the Bogoliubov transformations for the field operators.

The term $V\hat{\Psi}^\dagger\hat{\Psi}^\dagger\hat{\Psi}\hat{\Psi}$ is replaced by a bilinear form according to the mean field method. This leads to an effective Hamiltonian of the form

$$\begin{aligned}
\hat{H}_{eff} = \int d\mathbf{r} \Bigg[&\sum_\sigma \hat{\Psi}^\dagger(\mathbf{r}\sigma)\hat{H}_0\hat{\Psi}(\mathbf{r}\sigma) + U(\mathbf{r})\hat{\Psi}^\dagger(\mathbf{r}\sigma)\hat{\Psi}(\mathbf{r}\sigma) \\
&+\Delta(\mathbf{r})\hat{\Psi}^\dagger(\mathbf{r}\uparrow)\hat{\Psi}^\dagger(\mathbf{r}\downarrow) + \Delta^*(\mathbf{r})\hat{\Psi}(\mathbf{r}\downarrow)\hat{\Psi}(\mathbf{r}\uparrow)\Bigg]
\end{aligned} \tag{1.62}$$

where $U(\mathbf{r})$ is the Hartree-Fock averaged Coulomb potentials and $\Delta(\mathbf{r})$ and $\Delta^*(\mathbf{r})$ are the pairing potentials. Both Hartree-Fock and pairing potentials should be determined self-consistently.

The effective Hamiltonian is quadratic in the quasiparticle creation and annihilation field operators. Therefore, one can diagonalize it by the Bogoliubov transformations (1.28). The diagonalized effective Hamiltonian attains the form [11]

$$\hat{H}_{eff} = E_G + \sum_{n\sigma} E_n \hat{\gamma}^\dagger_{n\sigma}\hat{\gamma}_{n\sigma} \tag{1.63}$$

Here, E_G is the ground state energy and E_n is the excitation energy. We can calculate the commutator $\left[\hat{\Psi}(\mathbf{r}\sigma), \hat{H}_{\text{eff}}\right]$ using Eq. (1.29) and the anticommutation rules of the operators $\hat{\Psi}^\dagger(\mathbf{r}\sigma)$ and $\hat{\Psi}(\mathbf{r}\sigma)$ as follows

$$\begin{aligned}
\left[\hat{\Psi}(\mathbf{r}\uparrow), \hat{H}_{eff}\right] &= \left[\hat{H}_0 + U(\mathbf{r})\right]\hat{\Psi}(\mathbf{r}\uparrow) + \Delta(\mathbf{r})\hat{\Psi}^\dagger(\mathbf{r}\downarrow) \\
\left[\hat{\Psi}(\mathbf{r}\downarrow), \hat{H}_{eff}\right] &= \left[\hat{H}_0 + U(\mathbf{r})\right]\hat{\Psi}(\mathbf{r}\downarrow) - \Delta^*(\mathbf{r})\hat{\Psi}^\dagger(\mathbf{r}\uparrow)
\end{aligned} \tag{1.64}$$

Applying the Bogoliubov transformations given by Eq. (1.28) to the above equations and using Eq. (1.30), a pair of equations are obtained by which one can derive the Bogoliubov equations by comparing the coefficients of $\hat{\gamma}_n$ and $\hat{\gamma}^\dagger_n$:

$$\begin{cases} Eu(\mathbf{r}) = \left[\hat{H}_0 + U(\mathbf{r})\right] u(\mathbf{r}) + \Delta(\mathbf{r}) v(\mathbf{r}) \\ Ev(\mathbf{r}) = -\left[\hat{H}_0^* + U(\mathbf{r})\right] v(\mathbf{r}) + \Delta^*(\mathbf{r}) u(\mathbf{r}) \end{cases} \tag{1.65}$$

In the matrix form these equations are shown as

$$\begin{bmatrix} \hat{H}_0 + U(\mathbf{r}) & \Delta(\mathbf{r}) \\ \Delta^*(\mathbf{r}) & -\hat{H}_0^* - U(\mathbf{r}) \end{bmatrix} \begin{bmatrix} u(\mathbf{r}) \\ v(\mathbf{r}) \end{bmatrix} = E \begin{bmatrix} u(\mathbf{r}) \\ v(\mathbf{r}) \end{bmatrix} \tag{1.66}$$

In momentum space, for a quadratic form of $\hat{H}_0$ and including the effect of $U(\mathbf{r})$ in the effective mass m_S, we can rewrite this as

$$\begin{bmatrix} \xi_{\mathbf{k}} & \Delta(\mathbf{k}) \\ \Delta^*(\mathbf{k}) & -\xi_{\mathbf{k}} \end{bmatrix} \begin{bmatrix} u(\mathbf{k}) \\ v(\mathbf{k}) \end{bmatrix} = E \begin{bmatrix} u(\mathbf{k}) \\ v(\mathbf{k}) \end{bmatrix} \tag{1.67}$$

where

$$\xi_{\mathbf{k}} = \frac{\hbar^2 \mathbf{k}^2}{2m_S} + \mu_S \tag{1.68}$$

and

$$E = \pm E_{\mathbf{k}} = \sqrt{\xi_{\mathbf{k}} + \Delta^2} \tag{1.69}$$

We define the functions $u(\mathbf{k}) = u_0(\mathbf{k}) e^{-i\varphi/2}$ and $v(\mathbf{k}) = v_0(\mathbf{k}) e^{i\varphi/2}$, so that we find

$$\begin{aligned} u_0^2(\mathbf{k}) &= \frac{1}{2}\left(1 + \frac{\xi_{\mathbf{k}}}{E_{\mathbf{k}}}\right) \\ v_0^2(\mathbf{k}) &= \frac{1}{2}\left(1 - \frac{\xi_{\mathbf{k}}}{E_{\mathbf{k}}}\right) \end{aligned} \tag{1.70}$$

Using

$$\operatorname{arccosh} x = \ln\left(x + \sqrt{x^2 - 1}\right) \tag{1.71}$$

we have, for $E_{\mathbf{k}}^2 > \Delta^2$

$$\begin{aligned} u_0^2(\mathbf{k}) &= \frac{1}{2}\left(1 + \frac{\xi_{\mathbf{k}}}{E_{\mathbf{k}}}\right) = \frac{1}{2E_{\mathbf{k}}}\left(E_{\mathbf{k}} + \sqrt{E_{\mathbf{k}}^2 - \Delta^2}\right) = \frac{\Delta}{2E_{\mathbf{k}}} e^{\operatorname{arccosh} \frac{E_{\mathbf{k}}}{\Delta}} \\ v_0^2(\mathbf{k}) &= \frac{1}{2}\left(1 - \frac{\xi_{\mathbf{k}}}{E_{\mathbf{k}}}\right) = \frac{\Delta^2}{2E_{\mathbf{k}}} \frac{1}{E_{\mathbf{k}} + \sqrt{E_{\mathbf{k}}^2 - \Delta^2}} = \frac{\Delta}{2E_{\mathbf{k}}} e^{-\operatorname{arccosh} \frac{E_{\mathbf{k}}}{(997)}} \end{aligned} \tag{1.72}$$

Instead, for $E_{\mathbf{k}}^2 < \Delta^2$ we use

$$\arccos z = -i \ln\left(z + \sqrt{z^2 - 1}\right) \tag{1.73}$$

to write

$$\begin{aligned} u_0^2(\mathbf{k}) &= \frac{\Delta}{2E_\mathbf{k}} e^{i \arccos \frac{E_\mathbf{k}}{\Delta}} \\ v_0^2(\mathbf{k}) &= \frac{\Delta}{2E_\mathbf{k}} e^{-i \arccos \frac{E_\mathbf{k}}{\Delta}} \end{aligned} \tag{1.74}$$

This will be sufficient for our purpose, for further notions on Superconductivity, we refer to [30].

1.3.2 Andreev Reflection

The process of Andreev reflection occurs when an electron from the normal state material strikes the interface with energies below the superconducting energy gap. This electron forms a Cooper pair in the superconductor, accompanied by the retro-reflection of a hole with opposite spin and velocity but the same momentum as the incident electron, as illustrated in Figure 1.11. The junction is considered ideal here, meaning it has no impurity potential. In a spin-singlet superconductor, the Cooper pair is composed of an $\uparrow$- and $\downarrow$-spin electron; thus, a second electron with opposite spin to the incident electron from the normal state forms the Cooper pair in the superconductor, resulting in the reflected hole. This process is also applicable to other pairing types, as shown in the previous figure. Due to time-reversal symmetry, the same process occurs with an incident hole, producing an Andreev-reflected electron.

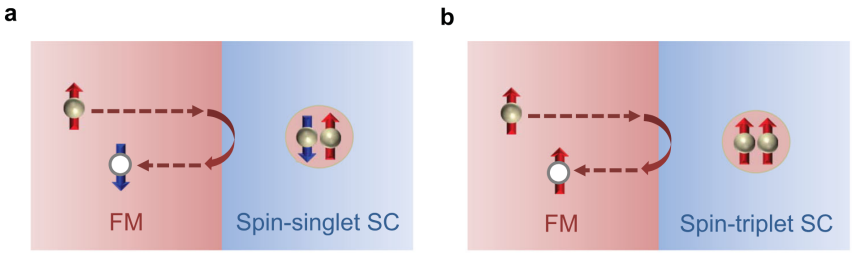

Figure 1.11: Visualization of the Andreev reflection process, for the case of a spin-singlet (a) and spin-triplet (b) superconductor. From [10].

This is a charge-transfer process by which normal current is converted to supercurrent in the superconductor. Each Andreev reflection transfers a charge $2e$ across the interface, avoiding the forbidden single-particle transmission within the superconducting energy gap.

1.3.3 METAL-SUPERCONDUCTOR JUNCTION AND BTK MODEL

Let us consider a planar NS interface lying in the xy-plane at $z = 0$ with a semi-infinite non-superconducting material (N) for $z < 0$ and a semi-infinite superconductor (S) for $z > 0$. The superconducting order parameter is assumed to vary in space only along the z-direction. In order to solve the BdG equations, we include only scattering at the NS interface. Following BTK [8], we model the scattering at the interface by a delta-function potential

$$U(\mathbf{r}) = V_0\delta(z)$$

where H is the strength of the potential barrier. For simplicity we neglect the phase of the pairing potential since only the absolute value is important for the considered geometry. Furthermore, to avoid self-consistent calculations, we take the superconducting order parameter to be zero in the normal conductor and uniform in the superconductor, i.e.

$$\Delta(\mathbf{r}) = \Delta_0\Theta(z),$$

where Δ_0 is the BCS value of the energy gap and $\Theta(z)$ is a Heaviside function. Similarly for the effective masses of the two materials, we assume that the mass changes abruptly across the interface

$$m^\star(\mathbf{r}) = m^{(\mathrm{N})}\Theta(-z) + m^{(\mathrm{S})}\Theta(z)$$

where $m^{(\mathbf{N})}$ and $m^{(\mathrm{S})}$ are the effective masses of the normal conductor and the superconductor, respectively.

Due to the simple form of the NS barrier potential, the superconducting order parameter and the effective mass, we can separate the variables and express the solutions in the parallel direction as plane waves, i.e. $\psi^{(\mathrm{N,S})}(\mathbf{r}) = \exp\left[i\left(k_x^{(\mathrm{N,S})}x + k_y^{(\mathrm{N,S})}y\right)\right]\psi^{(\mathrm{N,S})}(z)$, respectively. This yields the effective BdG equations for the z-direction

$$\begin{pmatrix} \left[-\frac{\hbar^2}{2m^{(\mathrm{N,S})}}\frac{\partial^2}{\partial z^2} + V_0\delta(z) - \mu_{\mathrm{eff}}^{(\mathrm{N,S})}\right] & \Delta_0\Theta(z) \\ \Delta_0\Theta(z) & -\left[-\frac{\hbar^2}{2m^{(\mathrm{N,S})}}\frac{\partial^2}{\partial z^2} + V_0\delta(z) - \mu_{\mathrm{eff}}^{(\mathrm{N,S})}\right] \end{pmatrix}\psi(z) = E\psi(z) \tag{1.75}$$

where the effective chemical potential is defined as

$$\mu_{\mathrm{eff}}^{(\mathrm{N,S})} \equiv \mu^{(\mathrm{N,S})} - \frac{\hbar^2}{2m^{(\mathrm{N,S})}}\left(\left[k_x^{(\mathrm{N,S})}\right]^2 + \left[k_y^{(\mathrm{N,S})}\right]^2\right) \tag{1.76}$$

We follow BTK and consider an electron-like quasiparticle incident on the NS inter-

face from the normal side. At the interface it has an amplitude r_{he} of undergoing Andreev reflection, r_{ee} of normal reflection, t_{ee} of normal transmission and t_{he} of Andreev transmission. The scattering amplitudes are obtained by matching the scattering states at the NS interface, using the appropriate boundary conditions for a delta-function potential barrier (see, e.g. [23]. The matching results in following linear system

$$\begin{pmatrix} 0 & 1 & -u_0 & -v_0 \\ 1 & 0 & -v_0 & -u_0 \\ 0 & \frac{2V_0}{\hbar^2} - i\frac{q_e^N}{m^{(\mathrm{N})}} & -i\frac{q_h^N}{m^{(\mathrm{S})}}u_0 & i\frac{q_h^S}{m^{(\mathrm{S})}}v_0 \\ \frac{2V_0}{\hbar^2} + i\frac{q_h^N}{m^{(\mathrm{N})}} & 0 & -i\frac{q_e^S}{m^{(\mathrm{S})}}v_0 & i\frac{q_h^S}{m^{(\mathrm{S})}}u_0 \end{pmatrix} \cdot \begin{pmatrix} r_{he} \\ r_{ee} \\ t_{he} \\ t_{ee} \end{pmatrix} = \begin{pmatrix} -1 \\ 0 \\ -\frac{2V_0}{\hbar^2} - i\frac{q_e^N}{m^{(\mathrm{N})}} \\ 0 \end{pmatrix} \tag{1.77}$$

Here, the quantities u_0 and v_0 read

$$\begin{aligned} u_0 &= \sqrt{\frac{1}{2}\left(1 + \sqrt{1 - \left(\frac{\Delta(\mathbf{r})}{E}\right)^2}\right)} \\ v_0 &= \sqrt{\frac{1}{2}\left(1 - \sqrt{1 - \left(\frac{\Delta(\mathbf{r})}{E}\right)^2}\right)} \end{aligned} \tag{1.78}$$

and the wavefunctions can in general be written as (we omit the N/S superscript and refer to the value of $\Delta(\mathbf{r})$) two electron-like solutions

$$\Psi_{\pm}^{e}(z) = \begin{pmatrix} u_0 \\ v_0 \end{pmatrix} e^{\pm i q_e z} \tag{1.79}$$

and two hole-like solutions

$$\Psi_{\pm}^{h}(z) = \begin{pmatrix} v_0 \\ u_0 \end{pmatrix} e^{\pm i q_h z} \tag{1.80}$$

where

$$\begin{aligned} q_e &= k_F \sqrt{1 + \sqrt{\frac{E^2 - \Delta(\mathbf{r})^2}{\mu_{\mathrm{eff}}^2}}} \\ q_h &= k_F \sqrt{1 - \sqrt{\frac{E^2 - \Delta(\mathbf{r})^2}{\mu_{\mathrm{eff}}^2}}} \end{aligned} \tag{1.81}$$

and

$$k_F = \frac{\sqrt{2m\mu_{\text{eff}}}}{\hbar} \tag{1.82}$$

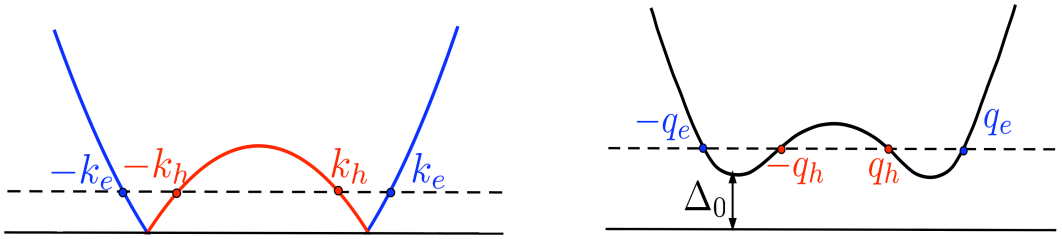

Figure 1.12: Solutions in the normal (left) and superconducting (right) region. Figures taken from [13].

The explicit solution of the linear set of equation is particularly simple in the so called **Andreev approximation**, which consists in envisaging low energies with respect to the Fermi level

$$E, \Delta_0 \ll \mu_{\text{eff}} \tag{1.83}$$

One can then approximate

$$q_{e/h} \simeq k_F \tag{1.84}$$

Under the Andreev approximation one finds for the transmission and reflection amplitudes

$$\begin{aligned} r_{he} &= \frac{u_0 v_0}{u_0^2 + Z^2\left(u_0^2 - v_0^2\right)} \\ r_{ee} &= \frac{\left(Z^2 + iZ\right)\left(v_0^2 - u_0^2\right)}{u_0^2 + Z^2\left(u_0^2 - v_0^2\right)} \\ t_{ee} &= \frac{(1 - iZ)u_0\sqrt{u_0^2 - v_0^2}}{u_0^2 + Z^2\left(u_0^2 - v_0^2\right)} \\ t_{he} &= \frac{iZv_0\sqrt{u_0^2 - v_0^2}}{u_0^2 + Z^2\left(u_0^2 - v_0^2\right)} \end{aligned} \tag{1.85}$$

Here

$$Z = \frac{V_0 m}{\hbar^2 k_F} \tag{1.86}$$

The corresponding transmission and reflection coefficients read

$$\begin{aligned} A &\doteq |r_{he}|^2 \\ B &\doteq |r_{ee}|^2 \\ C &\doteq |t_{ee}|^2 \\ D &\doteq |t_{he}|^2 \end{aligned} \tag{1.87}$$

In Figure 1.13 plot the two reflection coefficients A and B for different values of Z.

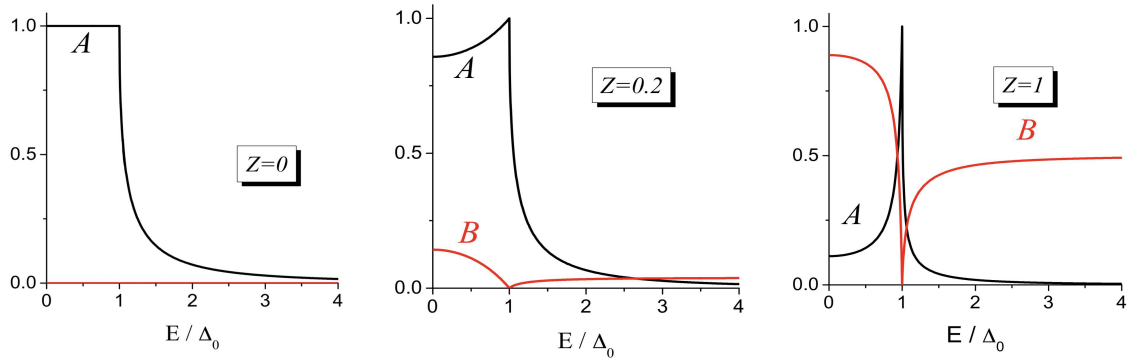

Figure 1.13: Normal (B) and Andreev (A) reflections for different values of renormalised barrier strength Z. Figures taken from [13].

1.3.4 Current and Conductance

Following BTK [8], the expression for the (single channel) current reads

$$I = \frac{2e^2}{h} \int dE \underbrace{T(E)}_{=1-R(E)} \left(f_L(E) - f_R(E)\right) \tag{1.88}$$

where $T(E)$ is the transmission coefficient of the sample, $R(E)$ its reflection coefficient, the pre-factor 2 stems from spin degeneracy, and $f_{L/R}(E)$ the Fermi functions of the Left and Right reservoirs

$$f_X(E) = \frac{1}{1+e^{(E-\mu_X)/k_BT}} \quad X = L/R \tag{1.89}$$

In the case of a (single channel) mesoscopic sample contacted to one normal and one superconducting electrode, the formula is modified as follows

$$I = \frac{2e^2}{h} \int dE(1 - B(E) + A(E)) \left(f_L(E) - f_R(E)\right) \tag{1.90}$$

The **non-linear conductance** at zero temperature then reads

$$G_{\mathrm{NS}}(V) \doteq \frac{dI}{dV} = \frac{2e^2}{h}(1 - B(eV) + A(eV)) \tag{1.91}$$

and we also note that

$$R_N = G_{\mathrm{NN}}^{-1} = \frac{h}{2e^2}\left(1 + Z^2\right) \tag{1.92}$$

is the resistance of the normal-normal junction. In Figure 1.14 there's a plot for it at some values of Z

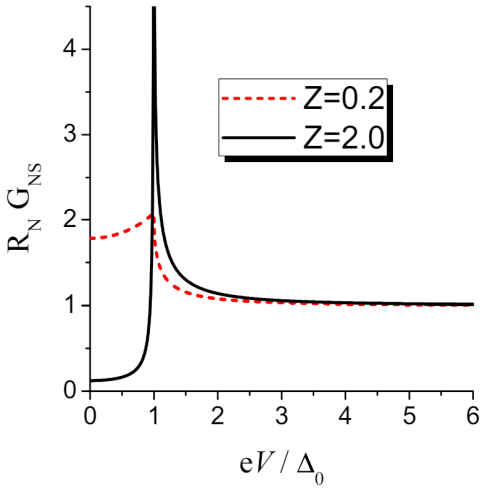

Figure 1.14: Zero temperature non-linear conductance for different values of the barrier strength. The cusp at $eV = \Delta_0$ corresponds to the singularity of the density of states of the superconductor at the gap. Figure taken from [13].

For high transparency the sub-gap regime is dominated by Andreev processes $(A \simeq 1)$ and therefore G_{NS} is finite, whereas at low transparency $(Z > 0)$ Andreev reflection is strongly suppressed in favor of normal reflection, yielding a strong reduction of $G_{\mathrm{NS}}(V)$. $G_{\mathrm{NS}}(V)$ exhibits a cusp at $\mathrm{eV} = \Delta_0$, corresponding to the singularity of the density of states of the superconductor at the gap.

2

Background and Motivations

2.1 Aim of this thesis

We study a W/S interface, where S is a BCS superconductor and W is a magnetic Weyl semimetal (i.e. with broken time-reversal symmetry). We are interested in the transport properties of the junction, with a focus on Andreev reflection, based on the BTK model briefly explained in the Introduction. More accurately, we are trying to understand the fate of Andreev reflection for different orientations of the Weyl node separation vector with respect to the interface. The existing literature predominantly addresses this topic by examining only two specific orientations of the Weyl nodes relative to the junction, i.e. the perpendicular and the parallel cases. In contrast, our model is designed to work for arbitrary orientations of the nodes and to minimise the need for simplifying assumptions. To better understand the purpose of this thesis, we first introduce what has already been done by two papers, one is by Uchida, Habe, Asano [32] (later referred to as UHA) and the other is by Bovenzi et al. [9]. The latter claims that Andreev reflection at the interface between a Weyl semimetal and a superconductor must involve a switch of chirality, otherwise it is blocked, defining the so-called **chirality blockade**. Instead, UHA do not claim to find any blockade and apply a slightly different model compared to Bovenzi et al..

We will now provide a more detailed explanation of what has been done by each team, to lay the basis for understanding our model, which will be described in the next section.

2.2 REVIEW OF THE PAPER BY UCHIDA, HABE, ASANO

2.2.1 MODEL BACKGROUND

To describe the electronic states in Weyl semimetals, UHA use a simple model given by

$$H_{\mathrm{W}} = \sum_{\alpha,\beta} \int dr \psi^{\dagger}_{\alpha}(r) \left[-\frac{\hbar^2}{2m_{\mathrm{W}}} \left(\nabla^2 + k_0^2\right) \hat{\sigma}_z \right. \\ \left. -i\lambda \left(\partial_x \hat{\sigma}_x + \partial_y \hat{\sigma}_y\right) - \mu_{\mathrm{W}} \hat{\sigma}_0 \right]_{\alpha,\beta} \psi_{\beta}(r), \tag{2.1}$$

where $\psi^{\dagger}_{\alpha}(r)$ and $\psi_{\alpha}(r)$ are the creation and annihilation operators of an electron with spin α at r, ∇ is the three-dimensional Laplacian, m_{W} is the effective mass of an electron, λ denotes the coupling constant of the spin-orbit interaction, and μ_{W} is the chemical potential measured from the Weyl nodes, which are found for $|k_z| = k_0$. The authors begin with a spin-degenerate two-band model as shown in Figure 2.1.

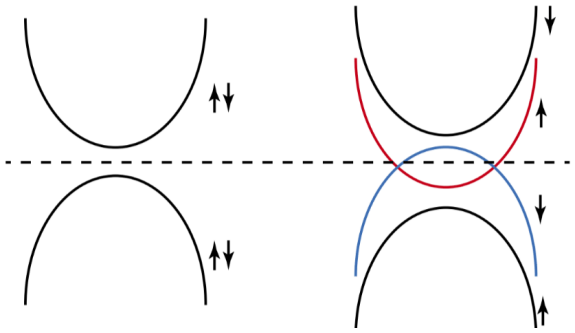

Figure 2.1: Schematic band structures of the original model. The Zeeman effect shifts the bands depending on the spin. Figure taken from [32].

The Zeeman field decreases (increases) the energy of the spin-up (spin-down) band. Large enough Zeeman fields result in the inverted band structure. The effects of the Zeeman field are taken into account through the k_0 term. The Pauli matrices $\hat{\sigma}_j$ for $j = x, y$, and z represent the real spins of an electron. The unit matrix in spin space is $\hat{\sigma}_0$. In the Fourier representation, Eq. (1) becomes

$$H_{\mathrm{W}}(k) = \begin{bmatrix} \varepsilon_k - \mu_{\mathrm{W}} & \lambda\left(k_x - ik_y\right) \\ \lambda\left(k_x + ik_y\right) & -\varepsilon_k - \mu_{\mathrm{W}} \end{bmatrix} \tag{2.2}$$

with $\varepsilon_k = \left(\hbar^2/2m_{\mathrm{W}}\right)\left(k^2 - k_0^2\right)$.

The Hamiltonian in a metallic superconductor, in the momentum space, was repre-

sented by

$$H_{\mathrm{S}}(k) = \begin{bmatrix} \xi_k \hat{\sigma}_0 & \Delta i \hat{\sigma}_y \\ -\Delta i \hat{\sigma}_y & -\xi^*_{-k} \hat{\sigma}_0 \end{bmatrix}, \qquad \xi_k = \frac{\hbar^2 k^2}{2m_{\mathrm{S}}} - \mu_{\mathrm{S}}, \tag{2.3}$$

where Δ is the amplitude of the pair potential, and m_{S} (μ_{S}) is the mass of an electron (the chemical potential) in the superconductor.

The wave functions on either sides of the junction are connected by the boundary conditions,

$$\begin{aligned} &\Psi_{\mathrm{W}}(z=0) = \Psi_{\mathrm{S}}(z=0), \\ &-\frac{\hbar^2}{2m_{\mathrm{W}}} \begin{bmatrix} \hat{\sigma}_z & 0 \\ 0 & \hat{\sigma}_z \end{bmatrix} \partial_z \Psi_{\mathrm{W}}(z)\Big|_{z=0} \\ &\quad = -\frac{\hbar^2}{2m_{\mathrm{S}}} \partial_z \Psi_{\mathrm{S}}(z)\Big|_{z=0} + [V_0 \hat{\sigma}_0 + V \cdot \hat{\sigma}]\, \Psi_{\mathrm{S}}(z=0), \end{aligned} \tag{2.4}$$

for the current in the z-direction. Here, the barrier potential $V_0 \delta(z)$ and the magnetic potential $V \cdot \hat{\sigma} \delta(z)$ at the interface are introduced. For the current in the x-direction, one needs to change z to x in the above conditions and add

$$\frac{\lambda}{2i} \begin{bmatrix} \hat{\sigma}_x & 0 \\ 0 & -\hat{\sigma}_x \end{bmatrix} \Psi_{\mathrm{W}}(x=0)$$

to satisfy the current conservation law.

2.2.2 RESULTS

By using the boundary conditions in the previous equation, UHA claim that for nodes orientation perpendicular to the junction, the results do not show significant differences with respect to the case of a normal metal / Superconductor junction. The differential conductance results (see Figure 2.3) confirm that indeed, for this orientation, transport properties are much like those of a normal Metal / Superconductor junction. However, we do notice an important difference: the Andreev reflected hole is in the **opposite node** with respect to the incoming electron, therefore having opposite sign of momentum (see Figure 2.2(a)), which differs from the normal metal case.

For nodes orientation parallel to the junction, the authors do not claim the presence of any chirality blockade, making the argument that spin-momentum conservation is still

possible for some incidence angles (see Figure 2.2(b)).

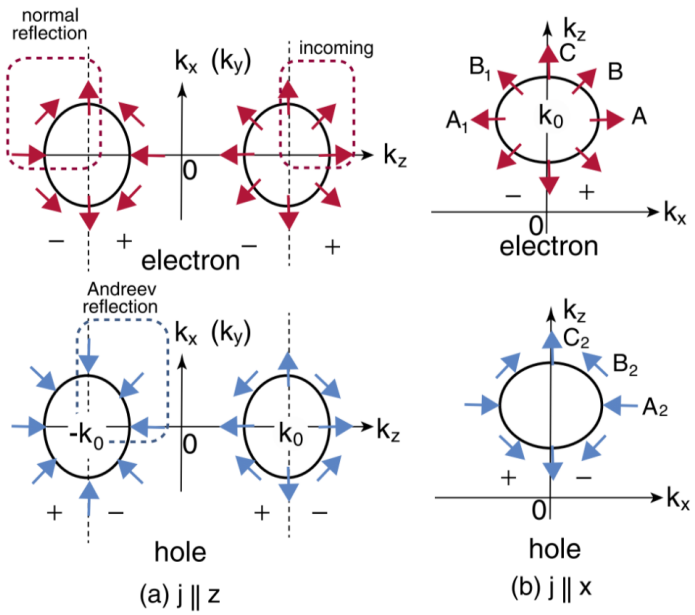

Figure 2.2: (Color online) Spin configuration on the Fermi surface within xz plane in spin space. We only show the spin configuration on the Fermi surface around $(0, 0, k_0)$ in (b). Spin is conserved in the normal reflection and it becomes opposite direction in the Andreev reflection. The $+(-)$ in the bottom of figures indicates the sign of the velocity in the current direction. Figures taken from [32].

However, the results for differential conductance do not support the claim of no blockade.

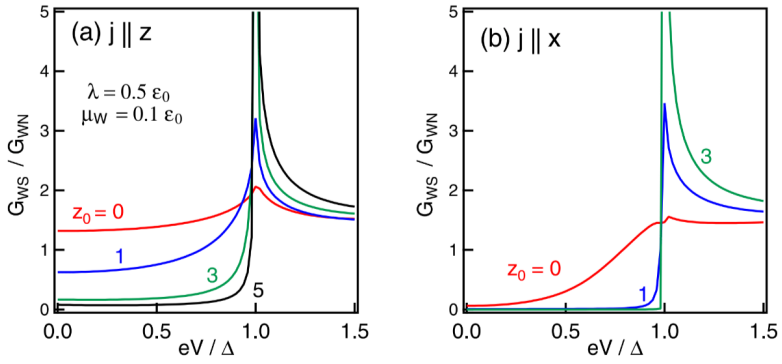

Figure 2.3: The differential conductance of Weyl-semimetal / superconductor junction is plotted as a function of the bias voltage for the current parallel to the z-axis in (a) and for the current parallel to the x-axis in (b). Figure taken from [32].

Indeed, by comparing the results in Figure 2.3 (b) with those in Figure 1.14 in Section 1.3.1, we see that almost only normal reflection is present for the configuration with

nodes orientation parallel to the junction and this implies that, by current conservation, **no Andreev reflection** is present in that configuration, i.e. the chirality blockade is actually present even though not claimed. However, the authors did not provide an analytical or numerical form for the reflection and transmission coefficients.

The way of showing the chirality texture seen in Figure 2.2 will be useful for the following.

2.3 BOVENZI ET AL. REVIEW

In the paper by Bovenzi et al.[9], the authors study the junction between a Weyl semimetal and a conventional (spin-singlet, s-wave) Superconductor by first considering separately the Hamiltonians in the two regions and then modelling the interface. In this paper, only the configuration of Weyl nodes parallel to the junction is studied. One major result claimed in this paper is the so-called chirality blockade, i.e. fully suppressed Andreev reflection due to a conservation of particle chirality in the Weyl semimetal. The system is depicted in Figure 2.4.

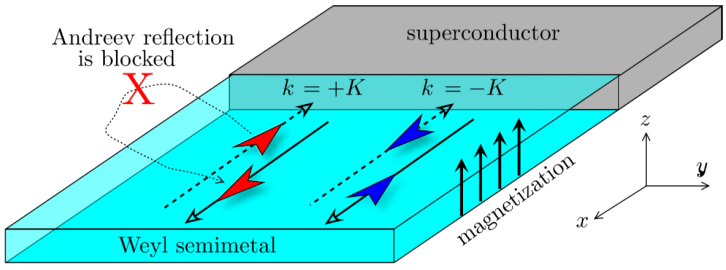

Figure 2.4: Andreev reflection (AR) from a superconductor in a Weyl semimetal. The red and blue wedges designate electron and hole quasiparticles (Weyl fermions) moving toward or away from the interface (solid vs dashed arrows indicate v in the $\pm x$ direction). The orientation of the wedge distinguishes the polarization $\sigma = \pm 1$ of the spin band, and the color indicates the chirality $C = \mathrm{sgn}(v\sigma)$. Andreev reflection switches σ and v, which is blocked if it must also switch C.Figure taken from [9].

2.3.1 MODEL BACKGROUND

The *first major difference* with respect to UHA's model is that in the present paper (as we will do later) **a four-band model** for the Weyl semimetal is considered, and therefore this allowed to add an *orbital* degree of freedom for the BCS superconductor as well.

The model relates the electron and hole degrees of freedom in the Weyl semimetal by the operation of time-reversal, with electron and hole Hamiltonians therefore given by:

$$H_{\mathrm{W}}^{(e)}(k) = H_{\mathrm{W}}(k), \quad H_{\mathrm{W}}^{(h)}(k) = \sigma_y H_{\mathrm{W}}^{*}(-k)\sigma_y \tag{2.5}$$

The two Hamiltonians are then incorporated in the 8x8 Bogoliubov-de Gennes (BdG) Hamiltonian

$$\begin{aligned} \mathscr{H}_{\mathrm{W}} &= \begin{pmatrix} H_{\mathrm{W}}^{(e)} & 0 \\ 0 & -H_{\mathrm{W}}^{(h)} \end{pmatrix} \\ &= v_z\tau_z\left(\sigma_x \sin k_x + \sigma_y \sin k_y + \sigma_z \sin k_z\right) \\ &\quad + m_W v_z \tau_x \sigma_0 + \beta v_0 \tau_0 \sigma_z - \mu_{\mathrm{W}} v_z \tau_0 \sigma_0. \end{aligned} \tag{2.6}$$

Electron-hole symmetry is expressed by

$$v_y\sigma_y \mathscr{H}_{\mathrm{W}}^{*}(-k) v_y \sigma_y = -\mathscr{H}_{\mathrm{W}}(k) \tag{2.7}$$

The region $x < 0$ contains a conventional spin-singlet s wave superconductor (real pair potential Δ_0), with the BdG Hamiltonian

$$\mathscr{H}_{\mathrm{S}} = \begin{pmatrix} p^2/2m - \mu_{\mathrm{S}} & \Delta_0 \\ \Delta_0 & -p^2/2m + \mu_{\mathrm{S}} \end{pmatrix} \tag{2.8}$$

For a chemical potential $\mu_{\mathrm{S}} \gg \mu_{\mathrm{W}}$, the momentum components p_y, p_z parallel to the NS interface at $x = 0$ can be neglected relative to the perpendicular component p_x.

The *second major difference* with respect to what done in the UHA paper is the expansion for $p_x = \pm p_{\mathrm{F}} + k_x$ around the Fermi momentum $p_{\mathrm{F}} = m v_{\mathrm{F}}$ (with $\mu_{\mathrm{S}} = p_{\mathrm{F}}^2/2m$) by carrying out the unitary transformation

$$\begin{aligned} \mathscr{H}_{\mathrm{S}} &\mapsto e^{-i\tau_z p_{\mathrm{F}} x} \mathscr{H}_{\mathrm{S}} e^{i\tau_z p_{\mathrm{F}} x} \\ &= v_{\mathrm{F}} k_x v_z \tau_z \sigma_0 + \Delta_0 v_x \tau_0 \sigma_0 + O\left(k_x^2\right) \end{aligned} \tag{2.9}$$

2.3.2 RESULTS

This **linearization** of the superconducting Hamiltonian leads to a different form of transfer matrix, due to the fact that now only one boundary condition is required (i.e. the continuity of the wavefunction at $x = 0$). This is because, once written in terms of differ-

ential operators, only linear derivative terms will appear in the Hamiltonian.

The analytical results for the reflection coefficients (see Section 1.3.3 for the meaning and origin of the coefficients in the BTK model) are found to be

$$|r_{ee}|^2 = 1 \quad , \quad |r_{he}|^2 = 0 \tag{2.10}$$

i.e., fully *suppressed Andreev reflection* at all energies (and also at all angles of incidence). This is what has been introduced as the **chirality blockade**. To better understand this definition, let us first consider the single-cone Weyl Hamiltonian centered at $k = (0,0,+K)$,

$$H_+ = v_x k_x \sigma_x + v_y k_y \sigma_y + v_z (k_z - K) \sigma_z. \tag{2.11}$$

where we remind the reader that its chirality is found as $C = sgn(v_x v_y v_z)$, see Section 1.2.5. For the second Weyl cone centered at $k = (0,0,-K)$ of opposite chirality, we can take either

$$H_- = -v_x k_x \sigma_x - v_y k_y \sigma_y - v_z (k_z + K) \sigma_z \tag{2.12}$$

or

$$H'_- = v_x k_x \sigma_x + v_y k_y \sigma_y - v_z (k_z + K) \sigma_z \tag{2.13}$$

or some permutation of x, y, z, but either all three signs or one single sign of the velocity components must flip.

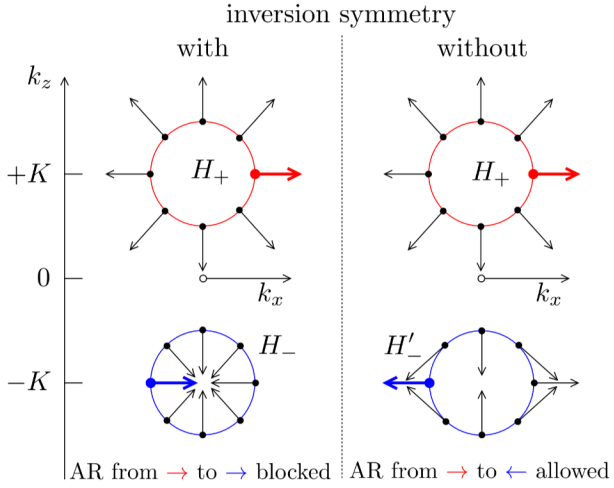

Figure 2.5: Illustration of the chiral texture for states at the Fermi energy in a pair of Weyl cones at $k = (0,0,\pm K)$. The arrows indicate the direction of the spin polarization for a momentum eigenstate at $k_y = 0$, as a function of k_x and k_z. The left column is for the Hamiltonian $H_W = (H_+, H_-)$ with inversion symmetry, the right column is for $H'_W = (H_+, H'_-)$ without inversion symmetry. Figure taken from [9].

The first choice satisfies inversion symmetry, $H_-(-k) = H_+(k)$, while the second choice does not. In Figure 2.5 the spin-momentum locking in the pair of Weyl cones with and without inversion symmetry is shown. Therefore, it is also claimed that the chirality blockade can be removed by breaking inversion symmetry.

Nevertheless, we point that from these results is also not entirely clear weather or not the authors assume that the hole sector has the same chiral texture as the nodes in the electron sector, which is not true in the case of $\mu_W \neq 0$. In addition, translational invariance across the junction requires conservation of the k_z component, and it is not clear from Figure 2.5 whether this is the case or not.

2.4 SUMMARY

To conclude this chapter, let us recap the main points and differences between the two papers presented and this thesis:

- Both papers deal with a two-node Weyl semimetal / superconducor junction, studying the transport properties of the latter.
- In UHA's paper, a simplified two-band model is used, excluding bands not displaying Weyl nodes. There is no claim of having a suppression of Andreev reflection for generic incidence, but the differential conductance results are actually showing it. No explicit form (either analytical or numerical) of the reflection/transmission coefficients is included.
- In Bovenzi et al., a less simplified four-band model is used for the Weyl side, but then the superconducting Hamiltonian is linearized, leading to only one boundary condition necessary. It is claimed a full suppression of Andreev reflection (i.e. chirality blockade), but the chiral texture argument seems to contradict the result. An explicit analytical expression for the reflection coefficients is provided in this paper. However, since the authors only consider a single orientation of the Weyl nodes, it remains unverified whether these reflection coefficients align with the results for the simpler case where the orientation is perpendicular to the junction or to those obtained by the BTK model.
- In this work, we will use a four-band model Weyl Hamiltonian (similar to the one of Bovenzi et al.), but we will not linearize the BCS superconductor one, keeping terms

(on both materials) of order $\mathbf{k}^2$. Consequently, our boundary conditions will lead to a more extensive system of equations compared to those found in existing literature. This thesis is also aimed at generalizing the formalism for a generic angle of Weyl nodes orientation with respect to the junction, which may help understand the origin and magnitude of the chirality blockade, if any is found. We will provide results for each reflection and transmission coefficient, for any generic orientation of Weyl nodes, along with the most important parameters that define the transport properties of a system.

We have now finished this section and will move on to presenting the theoretical framework we have created to explain what we mentioned in the last point.

3

Theory Development

3.1 Four-band Weyl Semimetal

3.1.1 Model Hamiltonian

As already mentioned in Section 1.2.3, the Hamiltonian model of a Weyl semimetal of our choice will be

$$H = \int d^3r \Psi^\dagger \left[-\sum_j i\gamma^0\gamma^j\partial_j + m_W(\mathbf{k})\gamma^0 + b_\mu\gamma^0\gamma^\mu\gamma^5 \right] \Psi \tag{3.1}$$

with $b = (b_0, \mathbf{b})$, which is the term that breaks time reversal T (and also parity P in the case where $b_0 \neq 0$) as presented in Section 1.2.3 and creates two Weyl nodes. For the rest of this work, we will deal with time-reversal broken (magnetic) Weyl semimetals. This requires that parity P is conserved, as explained in Section 1.2.3, and therefore we set $b_0 = 0$. Materials like this are those in the *XCrTe* class that we described in Section 1.2.10, with only two Weyl nodes, which is the minimum number of nodes and therefore represents an ideal system to study the transport properties of Weyl semimetals.

Note also that here we have left the Dirac mass term in its most generic form, i.e. with a possible dependence on $\mathbf{k}$. A more explicit form and explanation will be provided later in this chapter. The Hamiltonian in the chiral representation reads (see Section 1.2.3)

$$H_W = \tau_z[\sigma\cdot\mathbf{k}] + m_W(\mathbf{k})\tau_x + \sigma\cdot\mathbf{b} \tag{3.2}$$

In matrix form

$$H_W = \begin{pmatrix} H_+(\mathbf{k},\mathbf{b}) & m_W(\mathbf{k}) \\ m_W(\mathbf{k}) & H_-(\mathbf{k},\mathbf{b}) \end{pmatrix} \tag{3.3}$$

where

$$\begin{aligned} H_+(\mathbf{k},\mathbf{b}) &= (\mathbf{k}+\mathbf{b})\cdot\sigma \\ H_-(\mathbf{k},\mathbf{b}) &= -(\mathbf{k}-\mathbf{b})\cdot\sigma \end{aligned} \tag{3.4}$$

3.1.2 Block Diagonalization of the electronic sector

Following the idea of Bovenzi et al. [9], for $m_W(\mathbf{k}) \neq 0$, one can bring the Hamiltonian in block form using the transformation

$$\Omega_\theta = e^{-\frac{i}{2}\theta\tau_y(\hat{\mathbf{b}}\cdot\sigma)} = \cos\frac{\theta}{2} - i\tau_y(\hat{\mathbf{b}}\cdot\sigma)\sin\frac{\theta}{2} \tag{3.5}$$

for a conveniently chosen value of $\theta \in [0,\pi]$.

This is implemented as

$$\begin{aligned} \tilde{H}_W &= \Omega_\theta H_W \Omega_\theta^\dagger \\ &= \tau_z\left\{\sigma\cdot\mathbf{k}\cos\theta - \left[m_W(\mathbf{k})\sin\theta + \hat{\mathbf{b}}\cdot\mathbf{k}(1-\cos\theta)\right](\hat{\mathbf{b}}\cdot\sigma)\right\} \\ &\quad + \tau_x\left[m_W(\mathbf{k})\cos\theta + \hat{\mathbf{b}}\cdot\mathbf{k}\sin\theta(\hat{\mathbf{b}}\cdot\sigma)\sin\theta\right] + \sigma\cdot\mathbf{b} \end{aligned} \tag{3.6}$$

see Appendix A.1 for the detailed steps. In this way, one can choose

$$\cot\theta_{\mathbf{k}} = -\frac{\hat{\mathbf{b}}\cdot\mathbf{k}}{m_W(\mathbf{k})} \tag{3.7}$$

to make the off-diagonal term *vanish*. More explicitly, we take

$$\sin\theta_{\mathbf{k}} = \frac{m_W(\mathbf{k})}{d_{\mathbf{k}}} \quad \cos\theta_{\mathbf{k}} = -\frac{\hat{\mathbf{b}}\cdot\mathbf{k}}{d_{\mathbf{k}}} \tag{3.8}$$

with

$$d_{\mathbf{k}} = \sqrt{m_W(\mathbf{k})^2 + (\hat{\mathbf{b}}\cdot\mathbf{k})^2} \tag{3.9}$$

Therefore, one is left with

$$\begin{aligned}\tilde{H}_W &= \Omega_\theta H_W \Omega_\theta^\dagger \\ &= \tau_z \sigma \cdot \left\{ \mathbf{k} + \left[d_\mathbf{k} - \hat{\mathbf{b}} \cdot \mathbf{k} + \tau_z b \right] \hat{\mathbf{b}} \right\} = \tau_z \left\{ \sigma_\perp \cdot \mathbf{k}_\perp + \sigma_b \left[d_\mathbf{k} + \tau_z b \right] \right\}\end{aligned} \tag{3.10}$$

where it was convenient to define the direction " b " along $\mathbf{b}$ and the directions $\perp$, which are orthogonal to the first. It follows that there are **two Weyl nodes** at

$$k_W = \pm \sqrt{b^2 - m_W(\mathbf{k})^2} \tag{3.11}$$

coming from the $\tilde{H}_-$ block, as long as $b > m_W(\mathbf{k})$.

Let us rewrite the rotation matrix explicitly

$$\Omega_{\theta_\mathbf{k}} = \frac{1}{\sqrt{2 d_\mathbf{k}}} \left\{ \sqrt{d_\mathbf{k} - k_b} + i \tau_y (\hat{\mathbf{b}} \cdot \sigma) \sqrt{d_\mathbf{k} + k_b} \right\} \tag{3.12}$$

The block-diagonalized electron Hamiltonian therefore takes the form

$$\tilde{H}_W = \Omega_\theta H_W \Omega_\theta^\dagger = \begin{pmatrix} \tilde{H}_+ & \\ & \tilde{H}_- \end{pmatrix} \tag{3.13}$$

where the high- and low-energy transformed Hamiltonians now are

$$\begin{aligned}\tilde{H}_+ &= \sigma_\perp \cdot \mathbf{k}_\perp + \left[d_\mathbf{k} + b \right] \sigma_b \\ \tilde{H}_- &= \sigma_\perp \cdot \mathbf{k}_\perp + \left[d_\mathbf{k} - b \right] \sigma_b\end{aligned} \tag{3.14}$$

The energy spectrum of the previous Hamiltonian is shown in Figure 3.1.

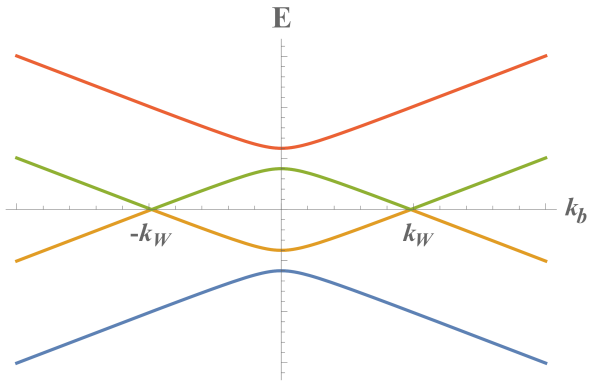

Figure 3.1: Energy spectrum of the Hamiltonian in Eq. (3.13). Here, $m_W(\mathbf{k}) \neq 0$ and $|\mathbf{b}| > m_W(\mathbf{k})$, $\forall \mathbf{k}$, so that two Weyl nodes of opposite chirality appear at $k_b \equiv \hat{\mathbf{b}} \cdot \mathbf{k} = \pm k_W$ and a gap is opened between the low-energy bands coming from the $\tilde{H}_-$ block and the high-energy ones coming from the $\tilde{H}_+$ block.

3.1.3 HOLES SECTOR

We define the hole Hamiltonian using the property that a hole is a T-reversed electron, meaning that we can write

$$H_W^h = -T\left[H_W\left(\mathbf{k},\mathbf{b}\right)\right] = -\left[\tau_z\left[\sigma\cdot\mathbf{k}\right] + m_W\left(\mathbf{k}\right)\tau_x - \sigma\cdot\mathbf{b} - \mu_W\right] = -H_W\left(\mathbf{k},-\mathbf{b}\right) \tag{3.15}$$

where we have introduced a chemical potential term μ_W. Note that this term actually signals the distance of the Weyl nodes from the Fermi energy, which was set here to be $E = 0$. The shape of the Fermi pockets for the electronic sector at different values of μ_W is shown in Figure 3.2.

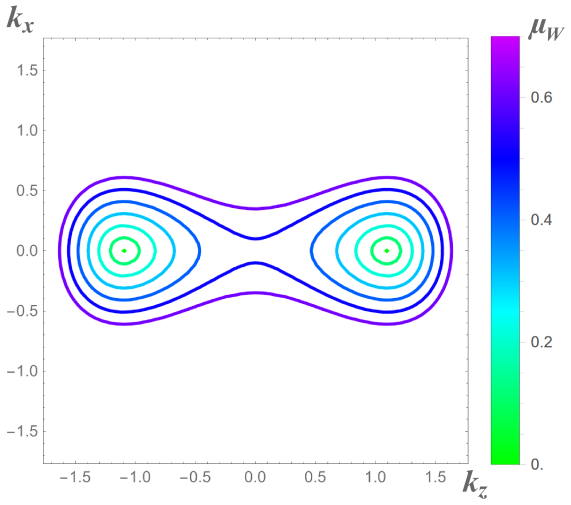

Figure 3.2: Fermi surfaces of the electronic sector in the (k_z, k_x)-plane for different values of μ_w

One needs now to extend the transformation to the holes part, in order to make that block diagonal as well. We can directly obtain the hole Hamiltonian transformation by taking the time-reversal of the whole rotated electron Hamiltonian, since the latter is already block diagonal, i.e.

$$\tilde{H}_W^h = -T\left[\tilde{H}_W\left(\mathbf{k}\right)\right] \tag{3.16}$$

Then, since

$$\tilde{H}_W(\mathbf{k}) = \Omega_{\theta(\mathbf{k})} H_W(\mathbf{k}) \Omega_{\theta(\mathbf{k})}^{-1} \tag{3.17}$$

we can write

$$\Omega_\theta(\mathbf{k}) = \begin{pmatrix} \Omega_{\theta(\mathbf{k})} & \\ & T\left[\Omega_{\theta(\mathbf{k})}\right] \end{pmatrix} = \begin{pmatrix} \Omega_{\theta(\mathbf{k})} & \\ & \sigma_y \Omega^*_{\theta(-\mathbf{k})} \sigma_y \end{pmatrix} \tag{3.18}$$

that acts on the BdG extension of the Weyl Hamiltonian (i.e. on the full 8x8 Electrons+Holes Matrix). Here

$$\sigma_y \Omega^*_\theta \sigma_y = \cos\frac{\theta}{2}\sigma_y \left(\mathbb{1} + i\tan\frac{\theta}{2}\tau_y(\hat{\mathbf{b}}\cdot\sigma)\right)^* \sigma_y = \Omega^\dagger_\theta \tag{3.19}$$

The last step in the time reversal operation is the **inversion of the momenta**, that acts as

$$\sin\theta_k \to \sin\theta_{-k} = \sin\theta_k \quad \cos\theta_k \to \cos\theta_{-k} = -\cos\theta_k$$

In other words

$$\theta \to \pi - \theta : \begin{cases} \sin\frac{\theta_k}{2} \to \cos\frac{\theta_k}{2} \\ \cos\frac{\theta_k}{2} \to \sin\frac{\theta_k}{2} \\ \tan\frac{\theta_k}{2} \to \cot\frac{\theta_k}{2} \end{cases}$$

We conclude that

$$T\left[\Omega_{\theta(\mathbf{k})}\right] = \sigma_y \Omega^*_{\theta(-\mathbf{k})} \sigma_y = \Omega^\dagger_{\pi-\theta(\mathbf{k})} \tag{3.20}$$

Grouping the terms and making some trigonometric simplifications, the transformed holes Hamiltonian becomes

$$\begin{aligned} \Omega^\dagger_{\theta(-\mathbf{k})} T[H(\mathbf{k},\mathbf{b})]\Omega_{\theta(-\mathbf{k})} =& \tau_x\left[-m_W(\mathbf{k})\cos\theta_{\mathbf{k}} - \sin\theta_{\mathbf{k}}(\hat{\mathbf{b}}\cdot\mathbf{k})\right] - \sigma\cdot\mathbf{b} - \mu_W \\ &+\tau_z\left[-\sigma\cdot\mathbf{k} - [(1+\cos\theta_{\mathbf{k}})(\hat{\mathbf{b}}\cdot\mathbf{k}) - 2m_W(\mathbf{k})\sin\theta_{\mathbf{k}}](\hat{\mathbf{b}}\cdot\sigma)\right] \end{aligned} \tag{3.21}$$

Using the choice made for the electron sector and one has

$$m_W(\mathbf{k})\cos\theta_{\mathbf{k}} + \sin\theta_{\mathbf{k}}(\hat{\mathbf{b}}\cdot\mathbf{k}) = m_W(\mathbf{k})\,\frac{-\hat{\mathbf{b}}\cdot\mathbf{k}}{\sqrt{m_W(\mathbf{k})^2 + (\hat{\mathbf{b}}\cdot\mathbf{k})^2}} + \frac{m_W(\mathbf{k})}{\sqrt{m_W(\mathbf{k})^2 + (\hat{\mathbf{b}}\cdot\mathbf{k})^2}}\,\hat{\mathbf{b}}\cdot\mathbf{k} = 0 \tag{3.22}$$

so we can extend the rotation matrix to

$$\hat{\Omega}_{\theta_{\mathbf{k}}} = \begin{pmatrix} \Omega_{\theta_{\mathbf{k}}} & \\ & \Omega^{\dagger}_{\theta_{-\mathbf{k}}} \end{pmatrix} = \begin{pmatrix} \cos\frac{\theta_{\mathbf{k}}}{2}\mathbb{1} - i\tau_y \hat{\mathbf{b}}\cdot\sigma \sin\frac{\theta_{\mathbf{k}}}{2} & \\ & \sin\frac{\theta_{\mathbf{k}}}{2}\mathbb{1} + i\tau_y \hat{\mathbf{b}}\cdot\sigma\cos\frac{\theta_{\mathbf{k}}}{2} \end{pmatrix} \tag{3.23}$$

The holes Hamiltonian is therefore given by

$$\begin{aligned} H^h_W &= -\Omega^{\dagger}_{\theta(-\mathbf{k})} T[H(\mathbf{k},\mathbf{b})]\Omega_{\theta(-\mathbf{k})} = \\ &= -\tau_z \left[\mathbf{k} - (\hat{\mathbf{b}}\cdot\mathbf{k})\hat{\mathbf{b}} - \frac{(\hat{\mathbf{b}}\cdot\mathbf{k})^2 + m_W(\mathbf{k})^2}{\sqrt{m_W(\mathbf{k})^2 + (\hat{\mathbf{b}}\cdot\mathbf{k})^2}}\hat{\mathbf{b}} - \tau_z \mathbf{b}\right]\cdot\sigma + \mu_W = -\tau_z\left\{\mathbf{k}_\perp - (d_{\mathbf{k}} + \tau_z b)\,\hat{\mathbf{b}}\right\} + \mu_W \end{aligned} \tag{3.24}$$

In conclusion, the complete Hamiltonian in the rotated˜basis is (we also re-introduce the chemical potential term $c_0 = \mu_W \neq 0$)

$$\tilde{H}_W = \begin{pmatrix} \mathbf{k}_\perp\cdot\sigma_\perp & & & \\ +(d_k+b)\,\sigma_z - \mu_W & & & \\ & -\mathbf{k}_\perp\cdot\sigma_\perp & & \\ & -(d_k-b)\,\sigma_z - \mu_W & & \\ & & -\mathbf{k}_\perp\cdot\sigma_\perp & \\ & & +(d_k+b)\,\sigma_z + \mu_W & \\ & & & \mathbf{k}_\perp\cdot\sigma_\perp \\ & & & -(d_k-b)\,\sigma_z + \mu_W \end{pmatrix}$$

$$= \tau_z\left[\nu_z\,\mathbf{k}_\perp + \nu_0\,(d_{\mathbf{k}} + \tau_z b)\,\hat{\mathbf{b}}\right] - \mu_W \nu_z \tag{3.25}$$

3.1.4 MASS TERM DEFINITION

The last equation is very general, but we now provide an explicit form for $m_W(\mathbf{k})$, which will be exploited in the following. For topological materials, the Dirac mass term can take the form [12]:

$$m_W(\mathbf{k}) = m_0 + g_m \mathbf{k}^2 \tag{3.26}$$

The particular value of g_m is not particularly relevant, as long as $g_m > -1$. Its sign is

the signal of the trivial (+) or topological (-) insulator phase when $\mathbf{b} = 0$ [12], which is not something we will focus on in this work. In this thesis we will make the assumption that

$$m_0 >> |\mathbf{k}| \tag{3.27}$$

and keep terms to the order of $O(\mathbf{k}^2)$. In this way, we can rewrite (3.9) by expanding, obtaining

$$d_{\mathbf{k}} \simeq m_0 + \frac{(\hat{\mathbf{b}} \cdot \mathbf{k})^2}{2m_0} + g_m \mathbf{k}^2 + O(\mathbf{k}^4) \tag{3.28}$$

by redifining $g_m \to \frac{g_m}{2m_0}$, this becomes

$$d_{\mathbf{k}} \simeq m_0 + \frac{\left[(\hat{\mathbf{b}} \cdot \mathbf{k})^2 + g_m \mathbf{k}^2\right]}{2m_0} \tag{3.29}$$

together with a redefinition of the Weyl nodes momentum

$$k_W \simeq \sqrt{2m_0 \left[\frac{b - m_0}{1 + g_m}\right]} \tag{3.30}$$

This approximation enables us to derive a transformed Hamiltonian that is **quadratic** in k_z for any orientation of the Weyl nodes, which is of the same order that we will maintain in the superconducting Hamiltonian, therefore allowing us to impose better matching conditions at the interface.

3.1.5 WEYL SEMIMETAL WAVEFUNCTIONS

Each block in the full Hamiltonian is a 2x2 matrix in momentum space, therefore can be written in the form

$$\tilde{H}_{\pm} = d_x \sigma_x + d_y \sigma_y + d_z \sigma_z \tag{3.31}$$

The eigenvectors for each 2x2 block are then found to be

$$\tilde{\Psi}_{\eta,\nu} = \frac{(\sigma_x)^{1-\frac{\eta}{2}-\frac{\nu}{2}}}{N_{\eta,\nu}} \begin{pmatrix} \eta |E \pm \mu_W| - d_z \\ \eta \nu d_x - i d_y \end{pmatrix} \tag{3.32}$$

where $\pm$ here stands for electron/hole and

$$N_\eta = \sqrt{2|E \pm \mu_W| \left(|E \pm \mu_W| - \eta d_z\right)} \tag{3.33}$$

and we define the two indices

$$\eta = Sign(d_z) \quad , \quad \nu = Sign(E \pm \mu_W) \tag{3.34}$$

and

$$|E \pm \mu_W| = \sqrt{d_x^2 + d_y^2 + d_z^2} \tag{3.35}$$

is the energy band eigenvalue (modulus) with respect to the Fermi energy.

For $\theta_b = 0$ $\left(i.e.\ \hat{b} = \hat{e}_z\right)$ we have that, for the low energy electronic bands (those described by $\tilde{H}_-$)

$$\begin{aligned} d_x &= -k_x, \\ d_y &= -k_y, \\ d_z &= -\left[m_0 - b + \frac{(1+g_m)}{2m_0}k_z^2 + \frac{g_m}{2m_0}k_x^2\right] \end{aligned} \tag{3.36}$$

As a reference, the sign of d_z for the low-energy bands is highlighted in the following graph.

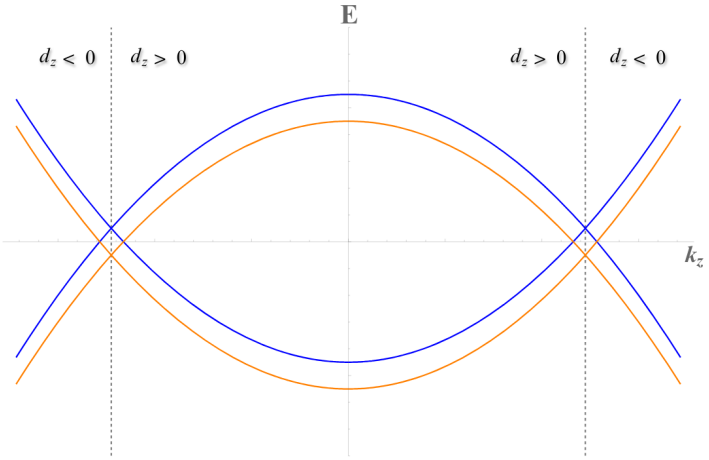

Figure 3.3: Low energy bands for the Electrons (orange) and Holes (blue) sectors, showing the sign of d_z for $\hat{b} = \hat{e}_z$. The vertical dashed lines are at $k_z = \pm k_W$.

We see that d_z changes sign whether $|k_z|$ is larger or smaller than the Weyl node momentum k_W, the magnitude of which we remind the reader to be

$$k_W \simeq \sqrt{2m_0\left[\frac{b - m_0}{g_m + 1}\right]} \tag{3.37}$$

Introducing the notation

$$\chi_+ = \lambda_+ = \begin{pmatrix} 1 \\ 0 \end{pmatrix} \quad , \quad \chi_- = \lambda_- = \begin{pmatrix} 0 \\ 1 \end{pmatrix}$$

with χ referring to the Nambu space and λ to the orbital space. We can generalise the previous eignefucntion to any block of the Weyl Hamiltonian by writing it as

$$\tilde{\Psi}_{\alpha,\beta,\eta,\nu} = \chi_\alpha \lambda_\beta \frac{(\sigma_x)^{1-\frac{\eta}{2}-\frac{\nu}{2}}}{N_{\eta,\nu}} \begin{pmatrix} \eta |E + \alpha\ \mu_W| - d_z \\ \eta\nu d_x - i d_y \end{pmatrix} \tag{3.38}$$

Having defined this, one can then build particle wavevectors as

$$\psi^W_{\alpha,\beta,\gamma}(z) = \tilde{\Psi}_{\alpha,\beta,\eta,\nu}\ e^{i k^W_{\alpha,\beta,\gamma}\, z} \tag{3.39}$$

Where we define the index $\gamma = \pm$, which, also for generic orientation, has the meaning of signaling a momentum $|k_z|$ that is either larger or smaller than the value of $k_W \cos\theta_b$. The index η can be found once the index γ has been fixed, therefore it is discarded from the notation we will use to label particles. The index ν is fixed by the energy E and by the index α and therefore is excluded from the notation as well. Each particle wavefunction can then be expressed through the combination of *only three indices* α, β, γ.
The momenta $k^W_{\alpha,\beta,\gamma}$ used in the exponential in the wavefunctions are given by the solutions of the dispersion relation. For example, for an orientation of Weyl nodes given by $\hat{\mathbf{b}} = \hat{\mathbf{e}}_z$, they have the form

$$k^W_{\alpha,\beta,\gamma}\left[\hat{\mathbf{b}} = \hat{\mathbf{e}}_z\right] = \pm\sqrt{k_W^2 + \eta\ \beta\ 2m_0\sqrt{(E + \alpha\ \mu_W)^2 - \left(k_x^2 + k_y^2\right)}} \tag{3.40}$$

Note the now-evident meaning of the index γ, signaling a momentum $|k_z| \gtrless k_W \cos\theta_b$. Notice also that we have generalised the form of k_W also for the higher energy bands, i.e.

$$k_W = \sqrt{2m_0\left(\frac{-\beta\ b - m_0}{1 + g_m}\right)} \tag{3.41}$$

although one clearly sees that these bands do not present Weyl nodes, having no real solution for $\beta = +$ for any energy. Nevertheless, this form is beneficial for maintaining a more concise index notation.

As an example of the previous notation, let us fix the orientation of Weyl nodes with $\hat{\mathbf{b}} = \hat{\mathbf{e}}_z$ and take an electron ($\alpha = +$) in the low energy bands from the $\tau_z = -$ block ($\beta = -$) with momentum greater than $k_z > k_W$ ($\gamma = +$, $\eta = -$) with $E > \mu_W$ ($\nu = +$), one has that

$(\sigma_x)^{1-\frac{\eta}{2}-\frac{\nu}{2}} = \sigma_x$ and the electronic wavefunction is given by

$$\psi^W_{+,-,+}(z) = \frac{1}{N}\begin{pmatrix} 0 \\ 0 \\ -d_x - id_y \\ -|E+\mu_W| - d_z \\ 0 \\ 0 \\ 0 \\ 0 \end{pmatrix} e^{ik^W_{+,-,+}\, z} \tag{3.42}$$

Similarly, for a hole ($\alpha = -$) in the low energy bands from the $\tau_z = -$ block ($\beta = -$) with momentum $k_z > k_W$ ($\gamma = +$, $\eta = -$) with $E < \mu_W$ ($\nu = -$), one has that

$$\psi^W_{-,-,+}(z) = \frac{1}{N}\begin{pmatrix} 0 \\ 0 \\ 0 \\ 0 \\ 0 \\ 0 \\ -d_x - id_y \\ |E-\mu_W| - d_z \end{pmatrix} e^{ik^W_{-,-,+}\, z} \tag{3.43}$$

To make the last results clearer, in Figure 3.4 we re-plot the low-energy bands with the momenta chosen in the earlier example.

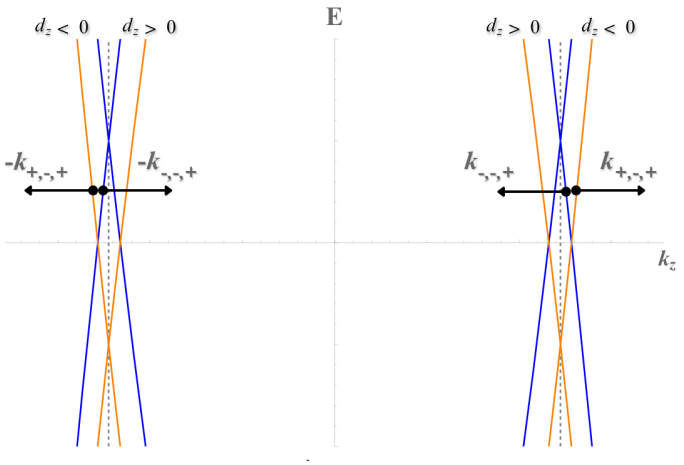

Figure 3.4: Example of momenta used in equations (3.42) and (3.43). The vertical dashed lines are at $k_z = \pm k_W$. Note that the electronic and hole bands are non-degenerte because of the term $\mu_W \neq 0$, indicating the energy separation of the Weyl nodes from the Fermi energy, that is set to zero in this context.

We trust that Section 4.2 will help to provide more clarity to the notation just used.

3.2 SUPERCONDUCTOR

On the superconducting side, we also construct a matrix that includes two orbitals and two spins. The electronic component is based on a quadratic dispersion relation. We assume the pairing to be *diagonal* in the orbital index and of *spin-singlet* type. Although different effective masses, pairing parameters, and pairing types could be employed, which would certainly affect the outcomes, we will adhere to the basic BCS framework and use m_S and Δ_0 for both orbitals. Therefore, the BdG Hamiltonian with this choice is

$$H_S = \begin{pmatrix} \xi_{\mathbf{k}}\tau_0\sigma_0 & -\Delta_0 e^{i\varphi}\tau_0 i\sigma_y \\ \Delta_0 e^{-i\varphi}\tau_0 i\sigma_y & -\xi_{\mathbf{k}}\tau_0\sigma_0 \end{pmatrix} \tag{3.44}$$

(note that $\nu_0 = \tau_0 = \sigma_0 = \mathbb{1}$). As a check, the Hamiltonian in second quantization is

$$\begin{aligned} H_S &= \frac{1}{2}\sum_{\mathbf{k}} \Psi^\dagger H_S \Psi = \frac{1}{2}\sum_{\mathbf{k}} \left(\psi^\dagger_{\mathbf{k}}, \psi_{-\mathbf{k}}\right) \begin{pmatrix} \xi_{\mathbf{k}}\tau_0\sigma_0 & -\Delta_0 e^{i\varphi}\tau_0 i\sigma_y \\ \Delta_0 e^{-i\varphi}\tau_0 i\sigma_y & -\xi_{\mathbf{k}}\tau_0\sigma_0 \end{pmatrix} \begin{pmatrix} \psi_{\mathbf{k}} \\ \psi^\dagger_{-\mathbf{k}} \end{pmatrix} \\ &= \sum_{a=1,2}\sum_{\mathbf{k}} \left\{ \xi_k \sum_{s=\uparrow\downarrow} \psi^\dagger_{a,\mathbf{k},s}\psi_{a,\mathbf{k},s} + \Delta_0 \left[e^{i\varphi}\psi^\dagger_{a,\mathbf{k},\downarrow}\psi^\dagger_{a,-\mathbf{k},\uparrow} + e^{-i\varphi}\psi^T_{a,-\mathbf{k},\uparrow}\psi_{a,\mathbf{k},\downarrow} \right] \right\} \end{aligned} \tag{3.45}$$

Let us write explicitly the eight-component nambu spinor

$$\Psi = \begin{pmatrix} \psi_{\mathbf{k}} \\ \psi^{\dagger}_{-\mathbf{k}} \end{pmatrix} = \left(\psi_{+\uparrow}, \psi_{+\downarrow}, \psi_{-\uparrow}, \psi_{-\downarrow}, \psi^{*}_{+\uparrow}, \psi^{*}_{+\downarrow}, \psi^{*}_{-\uparrow}, \psi^{*}_{-\downarrow}\right)^{T} \tag{3.46}$$

so that it has the **same ordering** for both orbitals and spin degrees of freedom as in the Weyl semimetal. The energy eigenvalues of any orbital have the same form that has been derived in Section 1.3.1, as well as $\xi_{\mathbf{k}}$. The energy bands are plotted in Figure 3.5

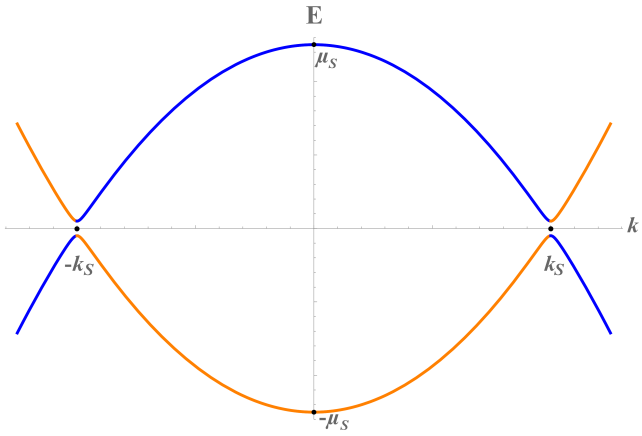

Figure 3.5: Energy bands in the superconductor. Electron-like excitations are the orange lines while hole-like ones are the blue lines. Note that the bands are degenerate for the orbital and spin degrees of freedom, therefore the total number is actually eight.

3.2.1 EIGENSTATES

For both fermionic species, we can write the eigenstates in terms of the functions $u(\mathbf{k}) = u_0(\mathbf{k})e^{-i\varphi/2}$ and $v(\mathbf{k}) = v_0(\mathbf{k})e^{i\varphi/2}$ as for those obtained in Section 1.3.1. An excitation with positive energy E will be a superposition of a spin- s particle and spin- $(-s)$ anti-particle in orbital $c = \pm$ and $s = \uparrow, \downarrow$. which is described by the spinor

$$\psi^{(S)}_{(c=1,2),(s=\uparrow,\downarrow)} = \begin{pmatrix} u_0(\mathbf{k})e^{i\varphi/2}\eta_c\chi_s \\ v_0(\mathbf{k})e^{-i\varphi/2}\eta_c\chi_s \end{pmatrix} \tag{3.47}$$

where we define

$$\eta_+ = \chi_\uparrow = \begin{pmatrix} 1 \\ 0 \end{pmatrix} \quad \eta_- = \chi_\downarrow = \begin{pmatrix} 0 \\ 1 \end{pmatrix} \tag{3.48}$$

and similarly for an excitation with energy $-E$

$$\psi_{c,s}^{(S)} = \begin{pmatrix} -v_0(\mathbf{k})e^{i\varphi/2}\eta_c\chi_s \\ u_0(\mathbf{k})e^{-i\varphi/2}\eta_c\chi_s \end{pmatrix} \tag{3.49}$$

For a given energy, the form of the momenta solutions found by inverting the dispersion relation in the superconductor is

$$k_{e(h)}^S = \pm\sqrt{2m_S\left(\mu_S + (-)\sqrt{E^2-\Delta_0^2}\right)} \tag{3.50}$$

Of course, one should note that for $E < \Delta_0$ the previous equation can be analytically continued to the form

$$k_{e(h)}^S = \pm\sqrt{2m_S\left(\mu_S + (-)i\sqrt{\Delta_0^2-E^2}\right)} \tag{3.51}$$

Note that we have

$$u_0(\mathbf{k}) = \begin{cases} \frac{1}{2}\left(1+\frac{\xi_\mathbf{k}}{E_\mathbf{k}}\right) & \text{if } |\mathbf{k}| = k_e^S \\ \frac{1}{2}\left(1-\frac{\xi_\mathbf{k}}{E_\mathbf{k}}\right) & \text{if } |\mathbf{k}| = k_h^S \end{cases} \tag{3.52}$$

and

$$v_0(\mathbf{k}) = \begin{cases} \frac{1}{2}\left(1-\frac{\xi_\mathbf{k}}{E_\mathbf{k}}\right) & \text{if } |\mathbf{k}| = k_e^S \\ \frac{1}{2}\left(1+\frac{\xi_\mathbf{k}}{E_\mathbf{k}}\right) & \text{if } |\mathbf{k}| = k_h^S \end{cases} \tag{3.53}$$

This can be rewritten as $v_0(k_h^S) = u_0(k_e^S)$ and $u_0(k_h^S) = v_0(k_e^S)$, for any energy.

3.2.2 SUPERCONDUCTOR IN THE TRANSFORMED BASIS

To derive the matching conditions for our junction interface, we need to first transform the superconductor Hamiltonian using the same matrix that was employed to block diagonalize the Weyl part of the Hamiltonian. This ensures that we are working within the same basis for the entire system (often referred to as the 'tilde' basis). Hence, the transformation acts as

$$\tilde{H}_S(\mathbf{k}) = \hat{\Omega}_{\theta_\mathbf{k}} H_S(\mathbf{k}) \hat{\Omega}^\dagger_{\theta_\mathbf{k}} = \begin{pmatrix} \xi_\mathbf{k} & -e^{i\varphi}\Delta_0\ \Omega_{\theta_\mathbf{k}}\ \tau_0 i\sigma_y\ \Omega_{\pi-\theta_\mathbf{k}} \\ e^{-i\varphi}\Delta_0\ \Omega^\dagger_{\pi-\theta_\mathbf{k}}\ \tau_0 i\sigma_y\ \Omega^\dagger_{\theta_\mathbf{k}} & -\xi_\mathbf{k} \end{pmatrix} \tag{3.54}$$

then, for $\varphi = 0$, we can rewrite it as

$$\begin{aligned} \tilde{H}_S(\mathbf{k}) =& \xi_\mathbf{k} \nu_z \tau_0 \sigma_0 + \Delta_0 \nu_y \left[2 f_+(\mathbf{k}) f_-(\mathbf{k}) \tau_0 i\sigma_y \right. \\ & \left. - \left(f_+^2(\mathbf{k}) - f_-^2(\mathbf{k}) \right) i\tau_y \left(\sigma_x \cos\theta_b - \sigma_z \sin\theta_b \right) \right] \end{aligned} \tag{3.55}$$

where the angle θ_b gives the orientation of Weyl nodes and will be better defined in the next section. We have also defined

$$f_\pm(\mathbf{k}) = \sqrt{\frac{\sqrt{m_0^2 + k_b^2 + g_m \mathbf{k}^2} \pm k_b}{2\sqrt{m_0^2 + k_b^2 + g_m \mathbf{k}^2}}} \tag{3.56}$$

Note that the superconductor Hamiltonian is not invariant under the transformation, i.e. $\tilde{H}_S \neq H_S$. In particular, the form of the pairing parameter matrix has now changed and displays an *orbital mixing* τ_y factor as well as a Weyl nodes *orientation dependent* $\sigma_{\perp,1}$ factor.

Note that we define the transformed basis "tilde" through a rotation of the whole Hamiltonian, i.e.

$$(H_W + H_S)\Psi \longrightarrow \left(\tilde{H}_W + \tilde{H}_S \right) \tilde{\Psi} \tag{3.57}$$

where Ψ has the ordering provided by Eq. (3.46) and was defined to maintain the same orbital and spin ordering in both materials. The explicit form of the superconductor eigenstates in the "tilde" basis depends on the orientation of Weyl nodes and will be addressed in the next section.

3.3 Generic Weyl Nodes Orientation

3.3.1 Generic orientation of the Weyl Hamiltonian

We now compute both Hamiltonians in the coordinates in which the future interface will be fixed at the $z = 0$ plane. We fix the initial position with an orientation of Weyl nodes perpendicular to the junction (i.e. $\hat{\mathbf{e}}_z$) and we rotate the vector $\mathbf{b}$ with respect to the interface, i.e. write the versor $\hat{\mathbf{b}}$ as

$$\hat{\mathbf{b}} = \begin{pmatrix} \cos\theta_b & 0 & \sin\theta_b \\ 0 & 1 & 0 \\ -\sin\theta_b & 0 & \cos\theta_b \end{pmatrix} \begin{pmatrix} 0 \\ 0 \\ 1 \end{pmatrix} \tag{3.58}$$

We remind the reader that this is easily achieved experimentally by rotating the magnetic field which is responsible for the separation of Weyl nodes, as explained in Section 1.2.10. We define $\theta_b = 0$ for when the Weyl node separation in momentum space is perpendicular to the interface.

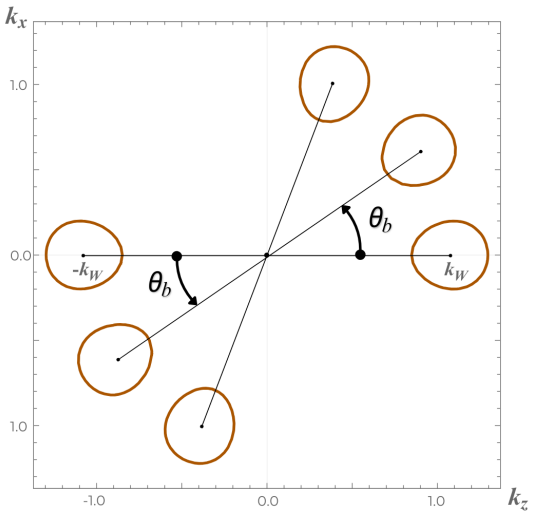

Figure 3.6: Fermi surfaces (not in scale) in the k_x, k_z plane for different values of Weyl nodes orientations, i.e. different values of θ_b.

As we can still perform the transformation $\hat{\Omega}_{\theta_\mathbf{k}}$, the Weyl Hamiltonian will preserve its block diagonal form, which translates, in general, to a second-order differential equation.

Clearly, the direction y is not affected, so $\hat{e}_{\perp,2} = \hat{e}_y$ and $\sigma_{\perp,2} = \sigma_y$. On the other hand, the other two components are

$$\begin{aligned} k_{\perp,1} &= \mathbf{k} \cdot \hat{e}_{\perp,1} = \cos\theta_b k_x - \sin\theta_b k_z \\ sk_b &= \mathbf{k} \cdot \hat{\mathbf{b}} = k_x \sin\theta_b + k_z \cos\theta_b \end{aligned} \tag{3.59}$$

and the same holds for the σ matrices

$$\begin{aligned} \sigma_{\perp,1} &= \sigma_x \cos\theta - \sigma_z \sin\theta \\ \sigma_b &= \sigma_z \cos\theta + \sigma_x \sin\theta \end{aligned} \tag{3.60}$$

Now, substituting this into (3.9), we have that

$$d_{\mathbf{k}} \approx m_0 + \frac{1}{2m_0}\left[k_x^2 \sin^2\theta_b + k_z^2 \cos^2\theta_b + 2k_x k_z \sin\theta_b \cos\theta_b + g_m\left(k_x^2 + k_z^2\right)\right] \tag{3.61}$$

and the transformed Weyl Hamiltonian takes the form

$$\begin{aligned}
\tilde{H}_W =& \tau_z\left[v_z\,\mathbf{k}_\perp + v_0\left(d_{\mathbf{k}} + \tau_z b\right)\hat{\mathbf{b}}\right] + \mu_W v_z, \\
=& \tau_z\left\{\sigma_x\left[v_z k_x \cos^2\theta_b + (m_0 + \tau_z b)\sin\theta_b + \frac{k_x^2}{2m_0}\sin^3\theta_b + \right.\right. \\
&+ \left.\left(\frac{k_x}{m_0}\sin\theta_b - v_z\right)\sin\theta_b\cos\theta_b k_z + \frac{1}{2m_0}\sin\theta_b\cos^2\theta_b k_z^2 + \sin\theta_b\frac{g_m}{2m_0}\left(k_x^2 + k_z^2\right)\right] \\
&+ v_z\sigma_y k_y \\
&+ \sigma_z\left[\left(m_0 + \tau_z b - v_z k_x \sin\theta_b + \frac{k_x^2}{2m_0}\sin^2\theta_b\right)\cos\theta_b\right. \\
&+ \left.\left.\left(v_z\sin\theta_b + \frac{k_x}{m_0}\cos^2\theta_b\right)\sin\theta_b k_z + \frac{\cos^3\theta_b}{2m_0}k_z^2 + \cos\theta_b\frac{g_m}{2m_0}\left(k_x^2 + k_z^2\right)\right]\right\}
\end{aligned} \tag{3.62}$$

In terms of the indices α, β, one can write

$$\begin{aligned}
d_x =& \beta\left[\alpha k_x \cos^2\theta_b + (m_0 + \beta b)\sin\theta_b + \frac{k_x^2}{2m_0}\sin^3\theta_b\right. \\
&+ \left.\left(\frac{k_x}{m_0}\sin\theta_b - \alpha\right)\sin\theta_b\cos\theta_b k_z + \frac{\sin\theta_b\cos^2\theta_b}{2m_0}k_z^2 + \sin\theta_b\frac{g_m}{2m_0}\left(k_x^2 + k_z^2\right)\right] \\
d_y =& \alpha\beta k_y \\
d_z =& \beta\left[\left(m_0 + \beta b - \alpha k_x \sin\theta_b + \frac{k_x^2}{2m_0}\sin^2\theta_b\right)\cos\theta_b\right. \\
&+ \left.\left(\alpha\sin\theta_b + \frac{k_x}{m_0}\cos^2\theta_b\right)\sin\theta_b k_z + \frac{\cos^3\theta_b}{2m_0}k_z^2 + \cos\theta_b\frac{g_m}{2m_0}\left(k_x^2 + k_z^2\right)\right]
\end{aligned} \tag{3.63}$$

The structure of the Weyl eigenfunctions remains **unchanged**, as it holds for any general form of d_x, d_y, and d_z.

3.3.2 GENERIC ORIENTATION FOR THE SUPERCONDUCTOR

On the superconducting side, the dependence on θ_b is limited to the transformed pairing term. We remind the reader that $\tilde{H}_S$ is given by

$$\begin{aligned}\tilde{H}_S(\mathbf{k}) =& \xi_{\mathbf{k}} \nu_z \tau_0 \sigma_0 + \Delta_0 \nu_y \left[2 f_+(\mathbf{k}) f_-(\mathbf{k}) \tau_0 i\sigma_y \right. \\ & \left. - \left(f_+^2(\mathbf{k}) - f_-^2(\mathbf{k}) \right) i\tau_y \left(\sigma_x \cos\theta_b - \sigma_z \sin\theta_b \right) \right]\end{aligned} \tag{3.64}$$

The generic form of the superconducting eigenfunctions with positive energy E is

$$\psi_{c,s}^{(S)} = \begin{pmatrix} u_0(\mathbf{k}) \eta_c \chi_s \\ v_0(\mathbf{k}) \left[2 f_+(\mathbf{k}) f_-(\mathbf{k}) \eta_c s \chi_{-s} - \left(f_+^2(\mathbf{k}) - f_-^2(\mathbf{k}) \right) c \eta_{-c} \left(\cos\theta_b \chi_{-s} - \sin\theta_b s \chi_s \right) \right] \end{pmatrix} \tag{3.65}$$

while for those with negative energy $-E$ is

$$\psi_{c,s}^{(S)} = \begin{pmatrix} -v_0(\mathbf{k}) \eta_c \chi_s \\ u_0(\mathbf{k}) \left[2 f_+(\mathbf{k}) f_-(\mathbf{k}) \eta_c s \chi_{-s} - \left(f_+^2(\mathbf{k}) - f_-^2(\mathbf{k}) \right) c \eta_{-c} \left(\cos\theta_b \chi_{-s} - \sin\theta_b s \chi_s \right) \right] \end{pmatrix} \tag{3.66}$$

As previously discussed, the pairing structure in the "tilde" basis causes the superconductor eigenfunctions to exhibit a mixing in both orbital and spin degrees of freedom. Nevertheless, as demonstrated in the Results section, this does not limit the study of the transport properties of the junction with a Weyl semimetal.

3.4 MATCHING CONDITIONS

The starting point to derive matching conditions at the junction interface is the generic Schrödinger equation

$$H\Psi = E\Psi$$

which we rewrite in the rotated basis

$$\tilde{H}\tilde{\Psi} = E\tilde{\Psi} \tag{3.67}$$

In this context, $\tilde{H}$ denotes the overall Hamiltonian of the entire system, which is partitioned into a $z < 0$ Weyl semimetal region and a $z > 0$ superconductor region. Essentially, this is

$$\tilde{H} = \tilde{H}_W\ \Theta(-z) + \tilde{H}_S\ \Theta(z) \tag{3.68}$$

It is important to observe that for a hetero-junction the quadratic term in the Hamiltonian takes the form [19]

$$\int dz \tilde{\Psi}^{\dagger}(z)\partial_z[\hat{M}(z)\partial_z]\tilde{\Psi}(z) \tag{3.69}$$

where $\hat{M}(z)$ can be seen as a generic space-dependent mass mattrix term. Therefore, we can write the complete Hamiltonian in differential form as

$$\begin{aligned}\tilde{H}\tilde{\Psi}(z) = \Big\{ \partial_z \Big[\hat{M}_W^{(2)}\Theta(-z) + \hat{M}_S^{(2)}\Theta(z)\Big]\,\partial_z \\ \Big[\hat{M}_W^{(1)}\Theta(-z) + \hat{M}_S^{(1)}\Theta(z)\Big]\,\partial_z + Const.\Big\}\,\tilde{\Psi}(z)\end{aligned} \tag{3.70}$$

where, in general, $\hat{M}_{W/S}^{(n)}$ are matrices of coefficients that are in front of the k_z^n term. Their form can be directly obtained from the results of the previous section in Eq. (3.62) and (3.63), and it is found to be

$$\begin{aligned}\hat{M}_S^{(2)} &= \frac{v_z\tau_0\sigma_0}{2m_S} \\ \hat{M}_S^{(1)} &= 0 \\ \hat{M}_W^{(2)} &= v_0\tau_z\left[\frac{\cos^2\theta_b + g_m}{2m_0}\right](\sigma_z\cos\theta_b + \sigma_x\sin\theta_b) \\ \hat{M}_W^{(1)} &= \tau_z\left[\sigma_z\left(\sin\theta_b + \frac{k_x}{m_0}\cos^2\theta_b\right) + \sigma_x\left(\frac{k_x}{m_0}\sin\theta_b - 1\right)\cos\theta_b\right]\sin\theta_b\end{aligned} \tag{3.71}$$

3.4.1 PROBABILITY CURRENT

The general form for the probability current is given by

$$\mathbf{j}(\mathbf{r},t) = \frac{\hbar}{2im}\left[\Psi^*(\nabla\Psi) - \Psi(\nabla\Psi^*)\right] \tag{3.72}$$

We then impose the continuity of the wavefunction at $z = 0$,

$$\tilde{\Psi}\left(0^-\right) = \tilde{\Psi}\left(0^+\right) = \tilde{\Psi}(0) \tag{3.73}$$

and derive a condition on the derivatives by imposing the continuity of the probability

current at $z = 0$,

$$\mathbf{j}_W(0^-) = \mathbf{j}_S(0^+) \tag{3.74}$$

Adding a delta-like potential $V_0\delta(z)$ to model the transparency of the interface, this results in

$$\left[\hat{M}_S^{(2)}\partial_z\tilde{\Psi}\left(0^+\right) - \hat{M}_W^{(2)}\partial_z\tilde{\Psi}\left(0^-\right)\right] - V_0\tilde{\Psi}(0) = 0 \tag{3.75}$$

Equations (3.73) and (3.75) will therefore build a system of *sixteen equations* that will provide the value of the coefficients of the **Transfer Matrix**.

Note that there is no dependence on the linear term coefficients $\hat{M}_{W/S}^{(1)}$, which is a result of conservation of the probability current, see Appendix A.2 for details.

NOTE: The inclusion of the g_m factor is crucial. Without it, the $\hat{M}_W^{(2)}$ coefficient matrix would decrease according to $\cos^2\theta_b$ (for $\theta_b \in [0, \pi/2]$) and would completely disappear in the case of parallel orientation of Weyl nodes with $\theta_b = \pi/2$. This would **significantly affect the matching conditions** conceptually, particularly causing Eq. (3.75) to become

$$\hat{M}_S^{(2)}\partial_z\tilde{\Psi}\left(0^+\right) - V_0\tilde{\Psi}(0) = 0 \tag{3.76}$$

leaving the derivative term of the superconductor unmatched by that of the other material. Consequently, this would result in misleading or incomplete outcomes, as merely ensuring the continuity of the wavefunction would be insufficient to accurately describe the transport properties of a junction, lacking any momentum dependence. Instead, for $g_m \neq 0$, the derivative term is present also on Weyl side for $\forall\theta_b$, therefore matching the superconducting one and providing a non trivial form of Eq. (3.75).

3.5 TRANSFER MATRIX

Let us now describe the formalism used to study the scattering processes across a generic junction interface. The following argument is valid for any choice of orientation of Weyl nodes and serves as an introduction for the notation used in the results section.

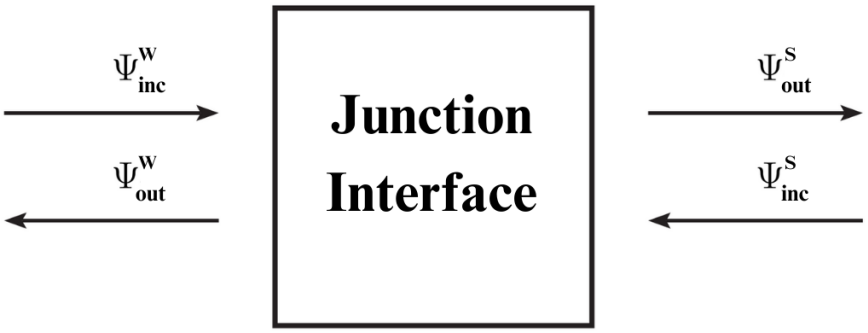

Figure 3.7: Junction interface relating the outgoing waves to the incoming waves.

In general, linear relations between outgoing and incoming waves can be written as

$$\begin{pmatrix} \Psi^{W}_{inc}(z=0) \\ \Psi^{S}_{inc}(z=0) \end{pmatrix} = \hat{\mathscr{S}} \begin{pmatrix} \Psi^{W}_{out}(z=0) \\ \Psi^{S}_{out}(z=0) \end{pmatrix}, \tag{3.77}$$

where the matrix $\hat{\mathscr{S}}$ is the *scattering matrix*. By definition, the matrix $\hat{\mathscr{S}}$ relates the outgoing waves to the incoming waves as shown in figure 3.7. We can also define the *transfer matrix* $\hat{\mathscr{T}}$ by the relation

$$\begin{pmatrix} \Psi^{W}_{inc}(z=0) \\ \Psi^{S}_{inc}(z=0) \end{pmatrix} = \hat{\mathscr{T}} \begin{pmatrix} \Psi^{W}_{out}(z=0) \\ \Psi^{S}_{out}(z=0) \end{pmatrix}. \tag{3.78}$$

In our case, it turns out that it is much more efficient to write a transfer matrix in terms of the probability with which each process contributes to the transport. To do this, we take the most general case and write the wavefunctions as a superposition of all possible processes, i.e. we define:

$$\begin{aligned} \Psi^{W}_{inc} &= \sum_{i=1}^{8} a_i \, \Psi^{W}_{inc,i} \\ \psi^{W}_{refl} &= \sum_{i=1}^{8} c_i \, \psi^{W}_{refl,i} \\ \Psi^{S}_{inc} &= \sum_{i=9}^{16} a_i \, \Psi^{S}_{inc,i} \\ \psi^{S}_{tot} &= \sum_{i=9}^{16} c_i \, \psi^{S}_{trans,i} \end{aligned} \tag{3.79}$$

where $|a_i|^2$ provides the probability of each incoming process and $|c_i|^2$ the probability of each reflected/transmitted. The number of possible processes is given by the nuber of

degrees of freedom: having defined a four-band model and having added the BdG formalism, the total degrees of freedom are 8. Furthermore, we note that for the superconductor wavevectors we use index numbering $i = 9, ..., 16$ to avoid defining a new set of coefficients.

In this way, we can rewrite (3.78) as

$$\begin{pmatrix} a_1 \\ \vdots \\ a_{16} \end{pmatrix} = \hat{\mathscr{T}} \begin{pmatrix} c_1 \\ \vdots \\ c_{16} \end{pmatrix} \tag{3.80}$$

As we already pointed out, the transfer matrix (and also the scattering matrix) can be derived by imposing the matching conditions equations (3.73) and (3.75) on each wavevector. Writing them in matrix notation, we obtain

$$\hat{\mathscr{M}}_{inc} \begin{pmatrix} a_1 \\ \vdots \\ a_{16} \end{pmatrix} = \hat{\mathscr{M}}_{out} \begin{pmatrix} c_1 \\ \vdots \\ c_{16} \end{pmatrix} \tag{3.81}$$

Where

$$\hat{\mathscr{M}}_{inc} = \begin{pmatrix} \Psi^W_{inc,1} & \cdots & \Psi^W_{inc,8} & \Psi^S_{inc,9} & \cdots & \Psi^S_{inc,16} \\ \left[ik_{inc,1}\hat{M}^{(2)}_W + V_0\right]\Psi^W_{inc,1} & & \left[ik_{inc,8}\hat{M}^{(2)}_W + V_0\right]\Psi^W_{inc,8} & \left[ik_{inc,9}\hat{M}^{(2)}_S\right]\Psi^S_{inc,9} & & \left[ik_{inc,16}\hat{M}^{(2)}_S\right]\Psi^S_{inc,16} \end{pmatrix} \tag{3.82}$$

and

$$\hat{\mathscr{M}}_{out} = \begin{pmatrix} \Psi^W_{refl,1} & \cdots & \Psi^W_{refl,8} & \Psi^S_{trans,9} & \cdots & \Psi^S_{trans,16} \\ \left[ik_{refl,1}\hat{M}^{(2)}_W + V_0\right]\Psi^W_{refl,1} & & \left[ik_{refl,8}\hat{M}^{(2)}_W + V_0\right]\Psi^W_{refl,8} & \left[ik_{trans,9}\hat{M}^{(2)}_S\right]\Psi^S_{trans,9} & & \left[ik_{trans,16}\hat{M}^{(2)}_S\right]\Psi^S_{trans,16} \end{pmatrix} \tag{3.83}$$

where, from here on, we leave out the z-dependence for conciseness. Note that since each wavevector has 8x1 dimensions, the two matrices $\hat{\mathscr{M}}_{inc}$ and $\hat{\mathscr{M}}_{out}$ are 16x16 square matrices.

Therefore, the generic transfer matrix $\hat{\mathscr{T}}$ for our junction interface is found to be:

$$\hat{\mathscr{T}} = \left[\hat{\mathscr{M}}_{inc}\right]^{-1} \hat{\mathscr{M}}_{out} \tag{3.84}$$

which is, of course, a 16x16 matrix as well. This formalism is the most general one and can basically provide all the transport properties of the system.

In the case of a **single incoming particle**, all we have to do is select the type of incoming particle by taking one of the a_i coefficients with unit value. For example, let us take $a_3 = 1$ (so that $a_j = 0$ for $j \neq 3$), which will later be identified as an incoming electron from the $c = 1$ Weyl node. What we obtain is an easier system to solve, i.e.

$$\begin{pmatrix} \Psi^W_{inc,3} \\ \\ \left[ik_{inc,3}\hat{M}^{(2)}_W + V_0\right]\Psi^W_{inc,3} \end{pmatrix} = \hat{\mathscr{M}}_{out} \begin{pmatrix} c_1 \\ \vdots \\ c_{16} \end{pmatrix}, \tag{3.85}$$

therefore significantly reducing the computational time required.

NOTE: it is important to mention that the momenta appearing in each wavefunction (and therefore also in the last equations) can in general be complex-valued, i.e. $k_{type,i} \in \mathbb{C}$, hence giving rise to **localized states** (i.e. $\propto e^{-k_z z}$) and therefore are regarded as evanescent waves. However, these states must still be included in the matching conditions, as done by Bovenzi et al. [9], in order to avoid having an *over-determined* system of equations, which in turn might give null solutions. For example, we have seen in Section 3.1.5 that for $\theta_b = 0$, the form of the momentum solutions at a given energy is given by Eq. (3.40). In this limit case, for

$$k^2_W\,[\beta = +] > \gamma\, 2m_W \sqrt{(E + \alpha\ \mu_W)^2 - \left(k_x^2 + k_y^2\right)} \tag{3.86}$$

one has complex-valued solutions. We will see that, for our choice of energy, the high-energy bands (those with $\beta = +$) will always have complex-valued momenta and, therefore, only give rise to localized states.

In addition, one can define a "threshold" angle θ_b^{th} after which only two k_z solutions are real-valued. For the range of energies of our interests, we can approximate Fermi pockets with spheres in the (k_x, k_y, k_z)-space of radius $|E + \alpha\mu_W|$. Therefore, the threshold angle is expected to behave as

$$\theta_b^{th} \sim \alpha |E + \alpha\mu_W| \tag{3.87}$$

For the high-energy bands, the concept of a threshold angle is not applicable, as it pertains to the presence of two distinct Fermi pockets forming the Fermi surface. Indeed, the high-energy bands lack Weyl nodes, resulting in a Fermi surface (in 2D) that is of single ellipse shape.

This concludes our discussion of the theory. We are now prepared to present the results derived from applying the formalism just described.

4 Results

The entirety of results presented in this chapter were obtained using the Mathematica software, in which we applied the analytical model described in the previous section. Before presenting the results, some introduction is necessary.

4.1 Parameters definition

We begin this section by specifying several numerical values for some of the key parameters.

As previously stated, the minimum quantity in the system is identified as the superconducting gap parameter Δ_0. We will restrict our results to energies within the range

$$|E| \in [0, 2\Delta_0] \tag{4.1}$$

since this is enough to capture low-energy transport properties of Weyl semimetals. For the sake of clarity, in this section we will rename $m_0 \doteq m_W$, so that it makes clearer the material to which it belongs and we will set $m_W = m_S$. Then, we also set

$$b = m_W + \delta_b \tag{4.2}$$

with $\delta_b < m_W$. Hence, substituting in (3.30), we find that the Weyl momenta is

$$k_W = \sqrt{2m_W \frac{\delta_b}{1+g_m}} < m_W \tag{4.3}$$

as requested by our approximation (see Eq. (3.27)). The particular value of g_m is not relevant for us, as already mentioned in Section 3.1.4. Although for normal incidence it can be proven that there is no dependence on μ_W, we still opt to set it with a finite value and bigger than the energy range we are considering, i.e. $\mu_W > 2\Delta_0$.

To reduce momenta discrepancies between the Weyl semimetal and the superconductor, we have tuned the values of the parameters in such a way that

$$k_S \simeq k_W \tag{4.4}$$

This decision equates to assuming that the Fermi momentum is identical for both materials. This approach allows us to more efficiently compare our findings with existing literature. Given that $\mu_S = \frac{k_S^2}{2m_S}$, this finalizes our parameter selection.

4.2 RESULTS NOTATION

To ensure the reader fully understands the results, we provide definitions for the notation that will be used subsequently.

As we described in the Theory section, all of the transport properties of the junction can be extrapolated from the solution of the system of equations

$$\begin{pmatrix} a_1 \\ \vdots \\ a_{16} \end{pmatrix} = \hat{\mathscr{T}} \begin{pmatrix} c_1 \\ \vdots \\ c_{16} \end{pmatrix} \tag{4.5}$$

where $|a_i|^2$ gives the probability of having an incoming particle described by the wavevector $\Psi^{W/S}_{inc,i}$, while $|c_i|^2$ for $i = 1,...,8$ gives the probability of having an outgoing particle described by the wavevector $\Psi^{W}_{refl,i}$ and $|c_i|^2$ for $i = 9,...,16$ the probability of having an outgoing particle described by the wavevector $\Psi^{S}_{trans,i}$.

On the Weyl side, we build particle wavevectors as

$$\psi^W_{\alpha,\beta,\gamma}(z) = \tilde{\Psi}_{\alpha,\beta,\eta,\nu}\, e^{ik^W_{\alpha,\beta,\gamma} z} \tag{4.6}$$

which has been properly defined in Section 3.1.5. We recall that each coefficient $\alpha, \beta, \gamma, \eta, \nu = \pm$, and they represent:

- α = electrons/holes
- β = high-energy / low-energy bands
- $\gamma = |k_z| \gtrless k_W \cos\theta_b$
- $\eta = Sign(d_z)$
- $\nu = Sign(E + \alpha\mu)$

The index ν is fixed once we fix the energy. The range of energies of our interest is with $|E| < \mu_W$, since for higher energies one would not see the presence of Weyl nodes and would retrieve the known results of Normal metals. Therefore, for this range of energies, we have that $\nu = \alpha$. The index η is only relevant for the definition of wavefunctions and can be found once the index γ has been fixed, therefore it is discarded from the notation we will use to label particles.

This leaves us with *eight possible combinations* for the remaining indices. Consequently, we can consolidate the indices α, β, η into a single i-index notation. This notation is briefly outlined in Table 4.1 and will be applied to all particle types in the Weyl semimetal, including both reflected and incoming ones.

i	α	β	γ	Description
1	+	+	+	High bands electron, with $\|k_z\| > k_W$
2	+	+	-	High bands electron, with $\|k_z\| < k_W$
3	+	-	+	Low bands electron, with $\|k_z\| > k_W$
4	+	-	-	Low bands electron, with $\|k_z\| < k_W$
5	-	+	+	High bands hole, with $\|k_z\| > k_W$
6	-	+	-	High bands hole, with $\|k_z\| < k_W$
7	-	-	+	Low bands hole, with $\|k_z\| > k_W$
8	-	-	-	Low bands hole, with $\|k_z\| < k_W$

Table 4.1: Synthetic description of index notation in the Weyl side. We remind that we are in the normal incidence case, i.e. $k_x = k_W \sin\theta_b$.

The same reasoning can be applied to the superconductor and we are again left with eight possible wave vectors, the meaning of which is underlined in Table 4.2.

i	Description
9	Electron-like particle from Orbital + with Spin-Z $\uparrow$
10	Electron-like particle from Orbital + with Spin-Z $\downarrow$
11	Electron-like particle from Orbital - with Spin-Z $\uparrow$
12	Electron-like particle from Orbital - with Spin-Z $\downarrow$
13	Hole-like particle from Orbital + , with Spin-Z $\uparrow$
14	Hole-like particle from Orbital + , with Spin-Z $\downarrow$
15	Hole-like particle from Orbital - , with Spin-Z $\uparrow$
16	Hole-like particle from Orbital - , with Spin-Z $\downarrow$

Table 4.2: Synthetic description of index notation in the superconductor side.

Note that this convention is only meaningful for the superconductor in the **non-transformed** basis, because, once the transformation $\hat{\Omega}_{\mathbf{k}}$ is applied, orbitals get mixed by the τ_y factor in the transformation.

To conclude, we want to properly weigh the coefficients c_i in such a way as to give them a more physical meaning. To do so we opted for using the continuity of the current, which we rewrite in terms of incoming / outgoing components es

$$\mathbf{j}_{tot}^{inc}(0) = \mathbf{j}_{W}^{inc}(0^-) + \mathbf{j}_{S}^{inc}(0^+) = \mathbf{j}_{tot}^{out}(0) = \mathbf{j}_{W}^{refl}(0^-) + \mathbf{j}_{S}^{trans}(0^+) \tag{4.7}$$

The unitarity of the current is then expressed by

$$1 = \frac{\mathbf{j}_{tot}^{out}(0)}{\mathbf{j}_{tot}^{inc}(0)} = \frac{\mathbf{j}_{W}^{refl}(0^-) + \mathbf{j}_{S}^{trans}(0^+)}{\mathbf{j}_{W}^{inc}(0^-) + \mathbf{j}_{S}^{inc}(0^+)} \tag{4.8}$$

By implementing the explicit form of each term in the continuity current (see Appendix A.3), this allows us to define a new series of positive-definite coefficients

$$\tilde{c}_i = \sqrt{\left| \frac{Re\left\{k_{refl/trans,i}\right\} \ |c_i|^2}{\mathbf{j}_{tot}^{inc}(0)} \right|} \tag{4.9}$$

It is important to note that, in order to obtain transport properties of finite-size objects, all momenta in the previous equations must be of the form $k_{type,i} \in \mathbb{R}$. As already explained, complex-valued momenta give rise to localized state, with evanescent wavevectors, and therefore they do not contribute to the current of finite-size materials.

Indeed, we remind the reader that (see Section 1.3.4) the **non-linear differential conductance** at zero temperature reads

$$G_{\mathrm{WS}}(V) \doteq \frac{dI}{dV} = \frac{2e^2}{h}(1 - NR(eV) + AR(eV)) \tag{4.10}$$

where WS stands for "Weyl semimetal / superconductor" junction and we also define

$$G_{\mathrm{WN}} = \lim_{\Delta_0 \to 0} G_{\mathrm{WS}} \tag{4.11}$$

is the differential conductance of the WSM-normal metal junction, which will be used as a reference value in presenting the results. In addition, $NR(eV)$ represents the total of all normal reflection processes, while $AR(eV)$ denotes the total of all Andreev reflection processes.

This concludes this notation section, which we hope will meet the reader's needs for understanding the results in their entirety. Let us therefore start presenting them.

4.3 Scattering of a single Weyl electron with transparent interface

To start presenting our results, we will initially concentrate on the two simplest orientations of the Weyl nodes relative to the junction: the perpendicular orientation case ($\theta_b = 0$) and the parallel orientation case ($\theta_b = \frac{\pi}{2}$). For the moment, we also assume a **transparent interface**, which means setting $V_0 = 0$.

4.3.1 Weyl Semimetal part of the junction

The momenta of the reflected wavevectors are found with the following procedure:

1. Fix an energy value E and an orientation angle θ_b.
2. Choose the value of k_x and k_y according to the intended electron incidence angle wrt. the junction. For the rest of this section we will focus on *normal incidence* with $k_y = 0$, so that we have
$$\begin{aligned} k_x &= k_W \sin\theta_b \\ k_y &= 0 \end{aligned} \tag{4.12}$$
3. Then, invert the eigenvalue equation
$$d_x^2 + d_y^2 + d_z^2 = (E \pm \mu_W)^2 \tag{4.13}$$
to find the possible values of the k_z-component of the momentum and select the proper one according to the reflection type. The analytical expression for k_z when

$\theta_b \neq 0$ is complicated, which makes it more practical to compute it numerically during each iteration of this procedure.

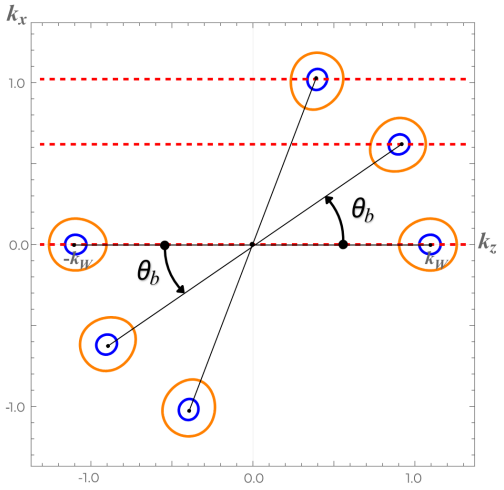

Figure 4.1: Depiction of the procedure for finding k_z values. Orange (Blue) contours are for electrons (holes) Fermi surfaces. Red dashed lines represent the value of $k_x = k_W \sin\theta_b$. The intersect of the red dashed lines and the orange (blue) contours gives the possible real-valued solutions for k_z.

In the case we are exploring now, one can write the total wavevector on the Weyl side as a superposition of the single incoming particle and all the possible reflections, i.e.

$$\psi^W_{tot} = \psi^W_{inc} + \psi^W_{refl} = \psi^W_{inc} + \sum_{i=1}^{8} c_i \, \psi^W_{refl,i} \tag{4.14}$$

where $|c_i|^2$ give the probability of being reflected as a particle described by the i^{th} wavevector.

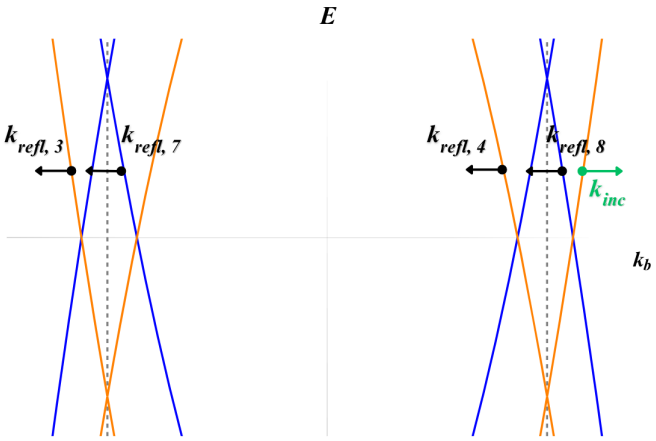

Figure 4.2: Depiction of momenta of the reflected particles (only real valued ones), for a fixed value of energy and $\theta_b = 0$.

4.3.2 SUPERCONDUCTOR PART OF THE JUNCTION

In the superconductor, the situation is quite a bit easier. We already derived the wavefunctions in the transformed "tilde" basis and, for positive energies, they are given by Eq. (3.65). For the choices of parameters we have made, we have set μ_S to be much larger than E, Δ_0. This is the so-called **Andreev approximation**, as already mentioned in Section 1.3.3, which slightly simplifies the system. In particular, under the Andreev approximation, we have that

$$k_S \simeq \sqrt{2m_S\mu_S}. \tag{4.15}$$

In addition to this, **translational invariance** through the junction is required for the k_X and k_y components of the momenta. Since k_S is a conserved quantity under rotation (it is a scalar), we can apply translational invariance $k_x^W \doteq k_x^S$ and, remembering that we are under the assumption of normal incidence (i.e. $k_x^W = k_W \sin\theta_b$), we can write:

$$k_z^S = \sqrt{k_S^2 - (k_x^S)^2 - (k_y^S)^2} = \sqrt{k_S^2 - (k_W \sin\theta_b)^2 - (k_y^S)^2} \tag{4.16}$$

Furthermore, since we imposed a choice of parameters such that $k_S \doteq k_W$, we obtain:

$$k_z^S = \sqrt{(k_W \cos\theta_b)^2 - (k_y^S)^2} \tag{4.17}$$

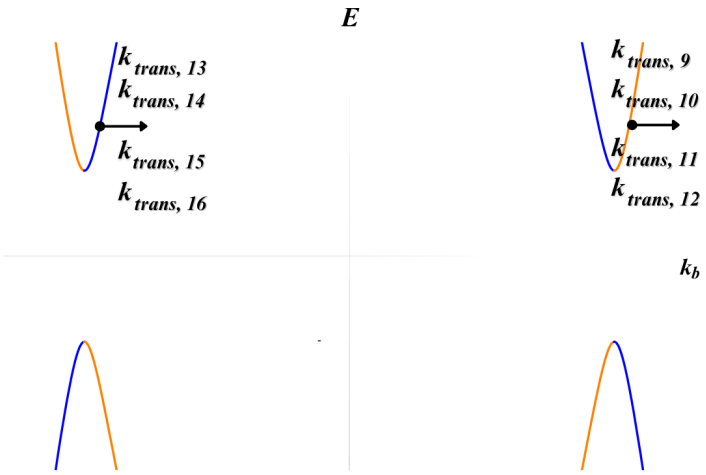

Figure 4.3: Depiction of momenta of the transmitted particles, for a fixed value of energy $E > \Delta_0$.

In Figure 4.3 one can see that, for $E > \Delta_0$, there are eight solutions for outgoing (transmitted) momenta, four degenerate electron-like ones and four degenerate hole-like ones, i.e. one for each orbital, spin and type of particle.

4.3.3 RESULTS FOR ZERO BARRIER POTENTIAL

With the help of Table 4.1, we see that to study the case of the scattering of a single electron coming from the $C = 1$ Weyl node (low-energy bands), it all reduces to solving the linear system of equations given by

$$\begin{pmatrix} \Psi^{W}_{inc,3} \\ \\ \left[ik_{inc,3}\hat{M}^{(2)}_{W} + V_0\right]\Psi^{W}_{inc,3} \end{pmatrix} = \hat{\mathscr{M}}_{out} \begin{pmatrix} c_1 \\ \vdots \\ c_{16} \end{pmatrix}, \tag{4.18}$$

The solution of this system returns the value of each coefficient c_i, which, once squared, provides the probability of a process to occur after the scattering.

As already pointed in Section 4.2, the quantities that we will plot are actually the modified coefficients $\tilde{c}_i$, which in the present case are given by

$$\tilde{c}_i = \sqrt{\left| \frac{k_{reflt/trans,i}}{k_{inc,3}} |c_i|^2 \right|} \tag{4.19}$$

According to our notation (see Table 4.1,) for electrons incoming from any band, the normal reflection and Andreev reflection components are then expressed as follows:

$$\begin{aligned} NR &= \sum_{i=1}^{4} |\tilde{c}_i|^2 \\ AR &= \sum_{i=5}^{8} |\tilde{c}_i|^2 \end{aligned} \tag{4.20}$$

WEYL NODES PERPENDICULAR TO THE JUNCTION

In Figure 4.4, we plot all the non-zero coefficients $\tilde{c}_i$ for fixed orientation $\theta_b = 0$, for positive energies in the range $E \in [0, 2\Delta_0]$. It is evident that they **closely resemble** the results of the BTK model presented in Section 1.3.3 for a Normal Metal / Superconductor junction (NS). Specifically, the only reflection coefficients that are non-zero are $\tilde{c}_3$ (normal reflection in the opposite Weyl node, resulting in negative momentum) and $\tilde{c}_8$ (Andreev reflection in the same Weyl node, resulting in positive momentum). It is observed that for energies below the gap, Andreev reflection is by far the dominant process. The non-zero probability of normal reflection, which was not present in the simple BTK model for the case $V_0 = 0$, is only due to a small, but hard to avoid in our model, mismatch in momentum magnitude between the Weyl and superconductor sides, which generates the same effect as

having an higher barrier strength $V_0 \neq 0$, as already studied and quantified by Blonder and Tinkam [7].

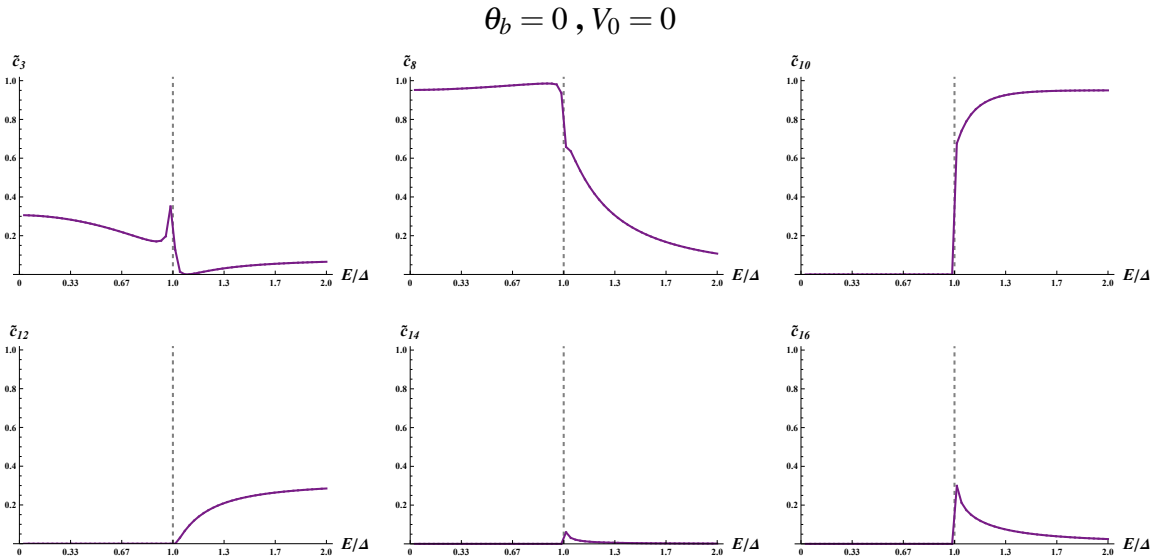

Figure 4.4: Non-zero coefficients $\tilde{c}_i$ with $V_0 = 0$, fixed orientation $\theta_b = 0$, for positive energies in the range $E \in [0, 2\Delta_0]$. Vertical grey-dashed lines are at $E = \Delta_0$.

On the superconductor side, for $E < \Delta_0$ there is no transmitted process allowed, due to the term $u_0^2 - v_0^2$ in the superconductor current, and only localized states are therefore allowed. For $E > \Delta_0$, to better understand the results, we sum all the wavevectors (weighted with the apposite coefficients) to see what type of particle is transmitted in the superconductor. This is because, after the transformation Ω, each wavevector obtains both an Orbital "+" and an Orbital "-" component, due to the transformed pairing that has a τ_y dependence. However, summing all weighted wavevectors, we find that the total transmitted particle in the superconductor is a spin-$\downarrow$ *electron-like* excitation, with only Orbital "-" components, because the Orbital "+" components exactly cancel out. This is in agreement with spin-momentum conservation, therefore allowing for the formation of a spin-$\downarrow\uparrow$ Cooper pair in the (spin-singlet) superconductor thanks to an Andreev reflected hole with spin-$\uparrow$ in the Weyl semimetal with an incoming spin-$\downarrow$ electron.

These initial results validate the hypothesis that when Weyl nodes are orientated perpendicular to the junction, the transport properties of the WS junction are very similar to those of the NS junction. In fact, the differential conductance for the WS case at $V_0 = 0$, shown in Figure 4.5, is almost the same as that of the NS case.

We note, however, that the Andreev reflected hole belongs to the same Weyl node of the incoming electron, in contrast to what found by UHA [32], but in agreement with the case of a NS junction.

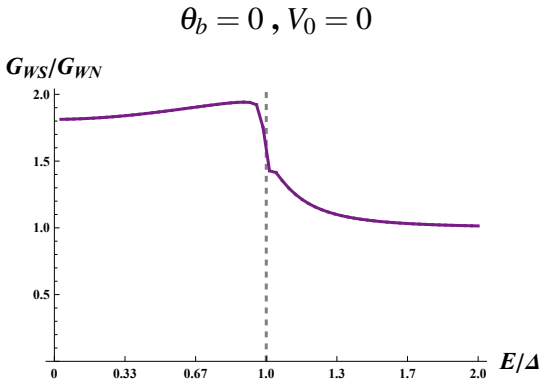

Figure 4.5: Normalized differential conductance G_{WS}/G_{WN} with $V_0 = 0$, fixed orientation $\theta_b = 0$, for positive energies in the range $E \in [0, 2\Delta_0]$. The vertical grey-dashed line is at $E = \Delta_0$.

WEYL NODES PARALLEL TO THE JUNCTION

In Figure 4.6, we plot all the non-zero coefficients $\tilde{c}_i$ for fixed orientation $\theta_b = \pi/2$, for positive energies in the range $E \in [0, 2\Delta_0]$.

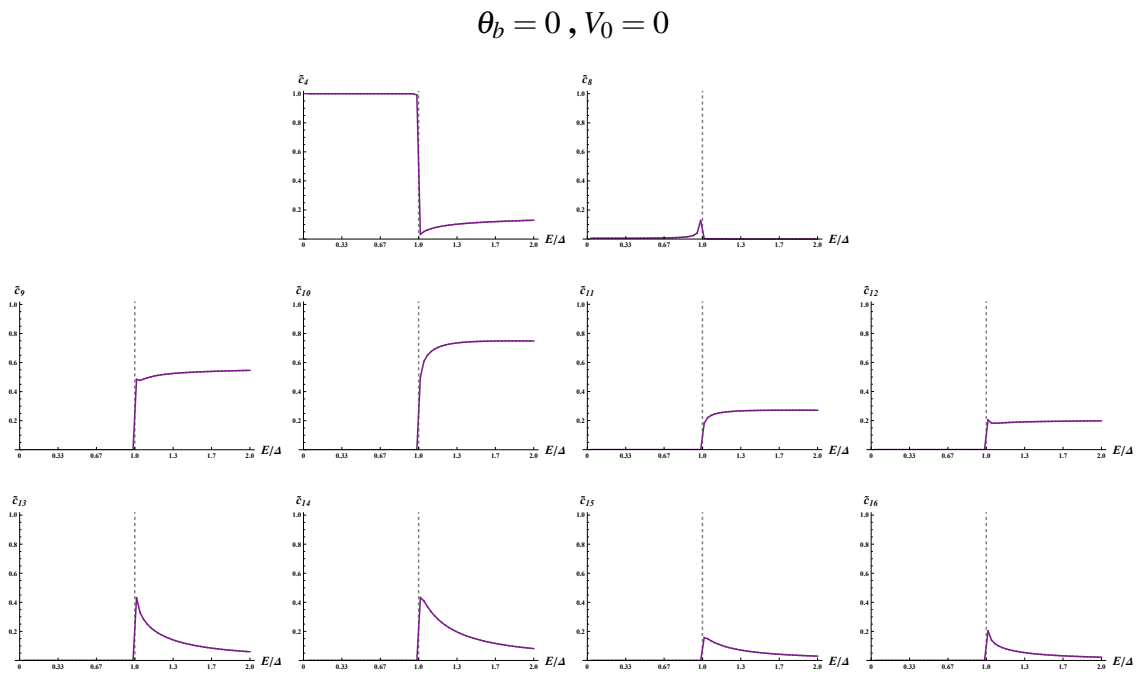

Figure 4.6: Non-zero coefficients $\tilde{c}_i$ with $V_0 = 0$, fixed orientation $\theta_b = 0$, for positive energies in the range $E \in [0, 2\Delta_0]$. Vertical grey-dashed lines are at $E = \Delta_0$.

From this figure, we see that the Andreev reflection coefficient $\tilde{c}_8$ is basically zero for any energy, and the dominant process for $E < \Delta_0$ is now the normal reflection, given by $\tilde{c}_4$. This is exactly what Bovenzi et al. [9] defined as **chirality blockade**. Note that the coefficient $\tilde{c}_4$ is related to a normal reflected electron in the same Weyl node as the incoming

electron, which is the expected result due to the conservation of the k_x components across the junction, which indeed fixes the chirality of the Weyl particles.

$$\theta_b = \pi/2\,,\, V_0 = 0$$

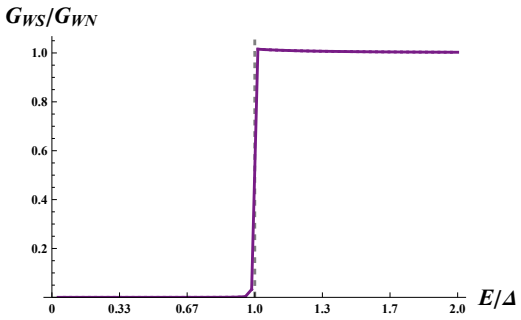

Figure 4.7: Normalized differential conductance G_{WS}/G_{WN} with $V_0 = 0$, fixed orientation $\theta_b = \pi/2$, for positive energies in the range $E \in [0, 2\Delta_0]$. The vertical grey-dashed line is at $E = \Delta_0$.

In Figure 4.7, we see that due to the fact that for $E < \Delta_0$ there is almost only normal reflection probability, which contributes negatively to the differential conduction, the latter is basically null up to $E = \Delta_0$. This means that the chirality blockade also results in a vanishing value for the current. For $E > \Delta_0$, the differential conductance reaches its asymptotic value of $G_{WS} = G_{WN}$, as expected, since excitation with energies above the superconductor's gap are always allowed.

The spin texture plot in Figure 4.8 for some possible angles θ_b may help to better understand the previous results.

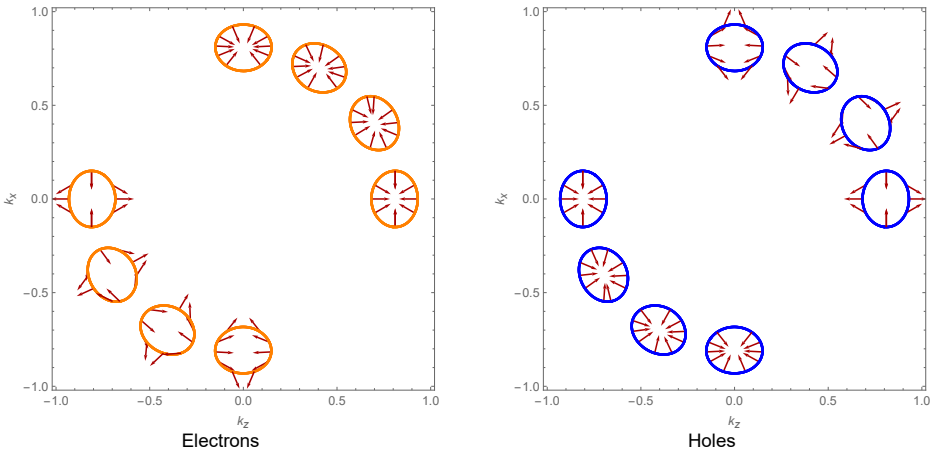

Figure 4.8: Spin texture of the low-energy bands, for an arbitrary positive energy $E < \mu_W$, for both types of particle and for different angle θ_b.

In the following argument, we refer to normal incidence only, i.e. fixing $k_x = k_W \sin\theta_b$.

For $\theta_b = 0$, the only normal reflection process allowed by spin-momentum conservation occurs in the opposite Weyl node relative to the incoming particle. In the case of spin-singlet superconductors, the Andreev reflected particle must have an opposite spin and velocity compared to the incoming particle, as described in Section 1.3.2. Based on our spin texture, this reflection must occur in the Weyl node with the same chirality as the incoming particle. This is exactly what we have reported above in the previous section. Conversely, for $\theta_b = \pi/2$, it is impossible to find an Andreev reflection process that respects the aforementioned spin-momentum characteristics. This is indeed what leads to the emergence of the chirality blockade, confirming the findings of Bovenzi et al. [9].

4.3.4 Results for non-zero barrier potential

In the following, we provide the same type of plots as presented in the previous section, but with non-zero potential barrier V_0. The results for the $\theta_b = 0$ case show that the normal reflection process becomes now the dominant one for most of the energy values, due to a non-zero barrier potential V_0, which is the expected behaviour, as described by the BTK model for the NS junction (see Figure 1.13(b)-(c) and Figure 1.14).

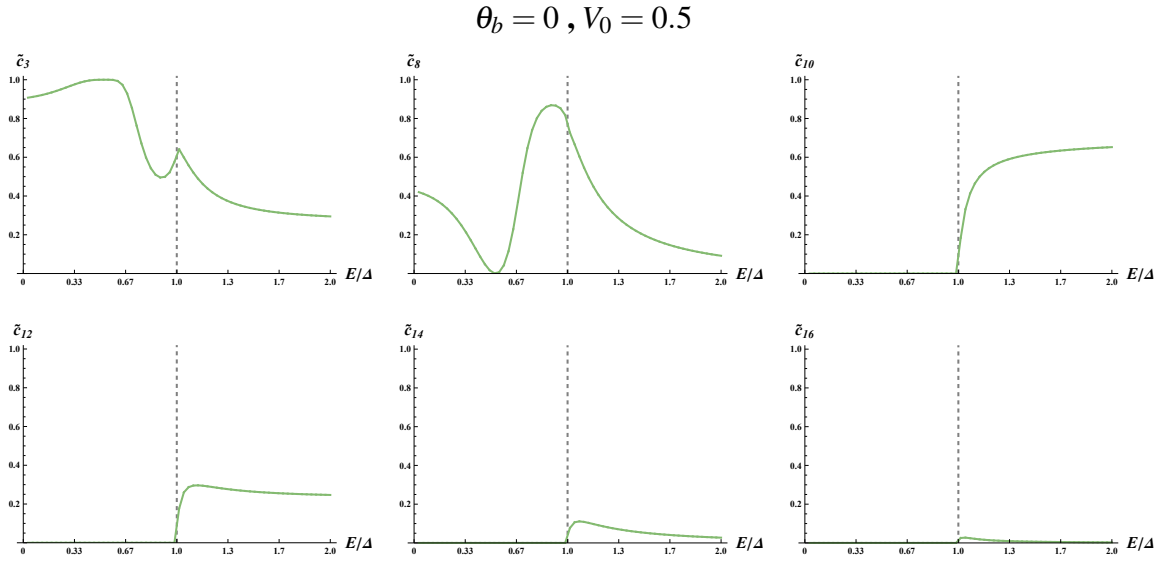

Figure 4.9: Non-zero coefficients $\tilde{c}_i$ with $V_0 = 0.5$, fixed orientation $\theta_b = 0$, for positive energies in the range $E \in [0, 2\Delta_0]$. Vertical grey-dashed lines are at $E = \Delta_0$.

$$\theta_b = 0\,,\, V_0 = 0.5$$

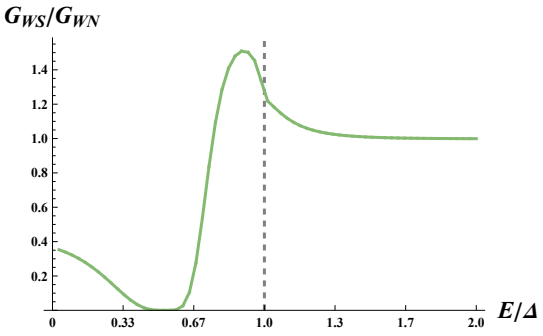

Figure 4.10: Normalized differential conductance G_{WS}/G_{WN} with $V_0 = 0.5$, fixed orientation $\theta_b = 0$, for positive energies in the range $E \in [0, 2\Delta_0]$. The vertical grey-dashed line is at $E = \Delta_0$.

Andreev reflection still has an important slice of the total probability for $E < \Delta_0$, while for energies above the gap it is more suppressed. The transmission processes have the same for as before, with some attenuation, because these type of processes are governed by a tunnelling effect, which naturally depends on the strength of the barrier potential.

The results for the $\theta_b = \pi/2$ case show that the normal reflection process is still the dominant process. Due to the presence of a non-zero barrier potential V_0, it remains dominant even when $E > \Delta_0$.

$$\theta_b = 0\,,\, V_0 = 0$$

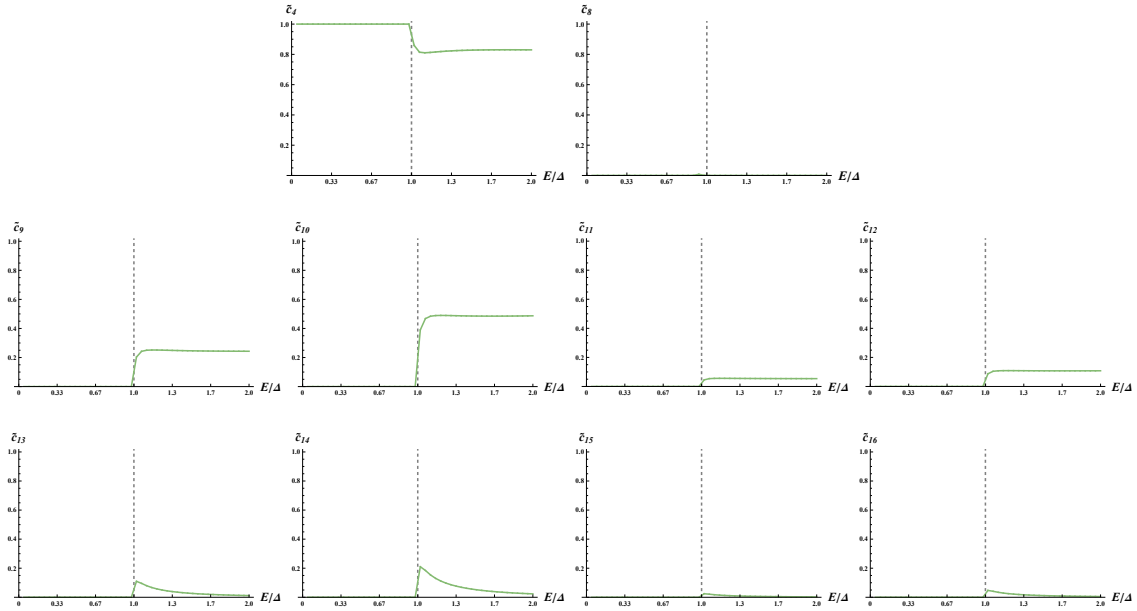

Figure 4.11: Non-zero coefficients $\tilde{c}_i$ with $V_0 = 0.5$, fixed orientation $\theta_b = \pi/2$, for positive energies in the range $E \in [0, 2\Delta_0]$. Vertical grey-dashed lines are at $E = \Delta_0$.

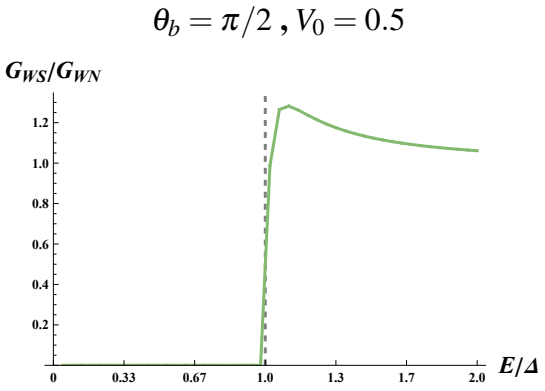

Figure 4.12: Normalized differential conductance G_{WS}/G_{WN} with $V_0 = 0.5$, fixed orientation $\theta_b = \pi/2$, for positive energies in the range $E \in [0, 2\Delta_0]$. The vertical grey-dashed line is at $E = \Delta_0$.

Andreev reflection is still completely suppressed due to the chirality blockade. The transmission coefficients retain the same structure as in the scenario without a potential barrier, experiencing attenuation for the same reason as explained for the $\theta_b = 0$ case. In addition, a small pike in the differential conductance in Figure 4.12 confirms the increase in the tunnelling barrier and the subsequent decrease in the transmission process.

4.3.5 CRITICAL ANGLE OF ORIENTATION

In this section, the energy is set to an arbitrary $E < \Delta_0$ to examine the behaviour of the reflection coefficients in the Weyl semimetal for various orientation angles θ_b.

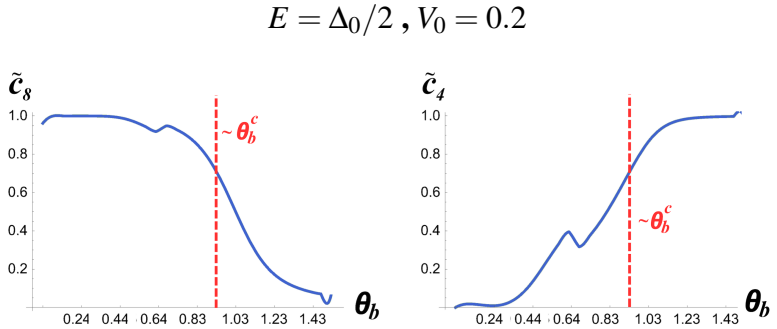

Figure 4.13: Non-zero reflection coefficients $\tilde{c}_4$ (normal reflection) and $\tilde{c}_4$ (Andreev reflection) with $V_0 = 0.2$, fixed energy $E = \Delta_0/2$, for orientation angles in the range $\theta_b \in [0, \pi/2]$.

From the results in Figure 4.13, it is observed that beyond a specific angle, the Andreev reflection coefficient $\tilde{c}_8$ becomes significantly suppressed. This enables us to define (at least numerically) a specific "critical" angle θ_b^c, beyond which normal reflection becomes

the predominant process as the chirality blockade starts to take effect. We define it as the angle at which the total of non-zero normal reflection coefficients exceeds the total of non-zero Andreev reflection coefficients (that is, when $NR(\theta_b^c) > AR(\theta_b^c)$), as shown in Figure 4.13. This angle certainly depends on the energy that we fix, but it also varies with the barrier potential V_0. This dependence is illustrated in Figure 4.14.

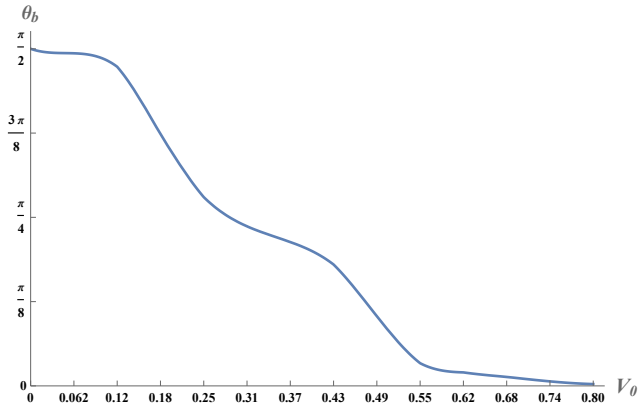

Figure 4.14: Critical angle θ_b^c at which the chirality blockade becomes effective, for different values of barrier potential V_0.

It is evident that the critical angle θ_b^c decreases monotonically with increasing V_0. This clearly indicates that the chirality blockade effect is highly dependent on the interface potential, which may lead to some possible experimental applications.

4.4 OTHER TYPES OF INCOMING PARTICLES

In this section, we present, in a form similar to what we have just done, the results for the other possible particles behaving as Weyl fermions, i.e. for electrons and holes with dispersion around a Weyl node of chirality $C = \pm 1$. The case we presented in the previous section was arbitrarily chosen to be the one of an electron coming from the Weyl node with $C = 1$. Let us now focus on the other possibilities.

ELECTRON INCOMING FROM WEYL NODE WITH $C = -1$

In Figures 4.15 and 4.16 we plot the case of an electron incoming from the node with opposite chirality with respect to the previous case, i.e. $C = -1$. Note that the incoming particle **spin-Z is switched** in the present case, as can be confirmed by the spin texture in Figure 4.8. It is evident that the only non-zero reflection coefficients are now $\tilde{c}_4$ and

$\tilde{c}_7$. This implies that the results are analogous to the scenario where an electron arrives from the Weyl node with $C = 1$, i.e., normal reflection occurs at the opposite Weyl node and Andreev reflection occurs at the same node. The transmission coefficients also yield similar results to the previous scenario; however, it is important to note that they now correspond to wavefunctions with the spin-Z component inverted, as expected.

$$\theta_b = 0\ ,\ V_0 = 0$$

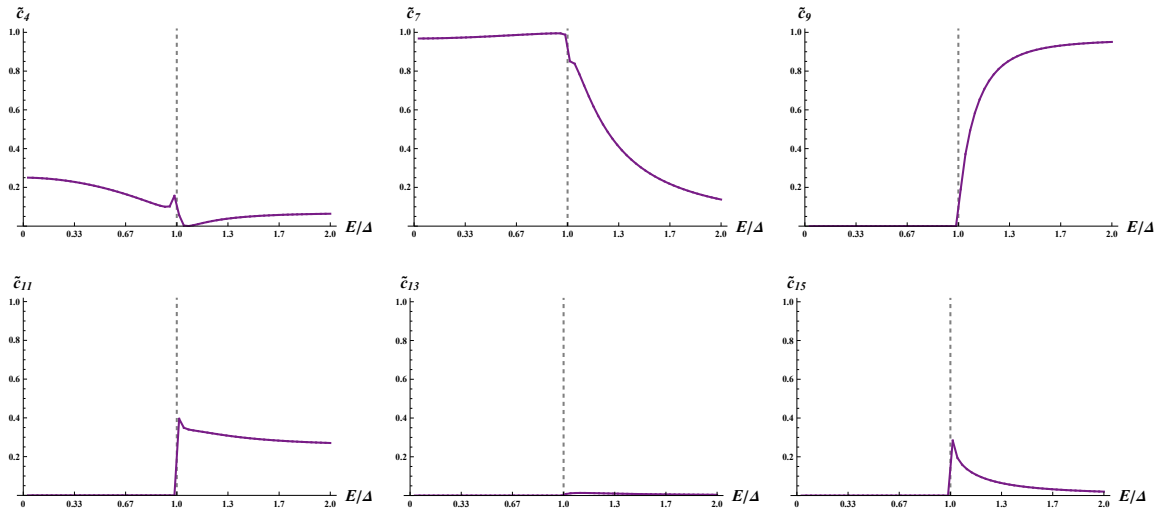

Figure 4.15: Non-zero coefficients with $V_0 = 0$, fixed orientation $\theta_b = 0$, for positive energies in the range $E \in [0, 2\Delta_0]$ for an electron incoming from Weyl node with $C = -1$. Vertical grey-dashed lines are at $E = \Delta_0$.

$$\theta_b = 0\ ,\ V_0 = 0$$

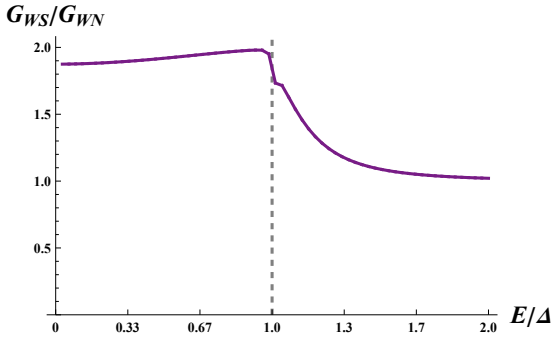

Figure 4.16: Normalized differential conductance G_{WS}/G_{WN} with $V_0 = 0$, fixed orientation $\theta_b = 0$, for positive energies in the range $E \in [0, 2\Delta_0]$ for an electron incoming from Weyl node with $C = -1$. The vertical grey-dashed line is at $E = \Delta_0$.

For the case where $\theta_b = \pi/2$, we obtain the results shown in Figures 4.17 and 4.18.

Note that since the superconducting side does not provide significant insight, we will no longer plot the transmission coefficients.

$$\theta_b = \pi/2 \, , V_0 = 0$$

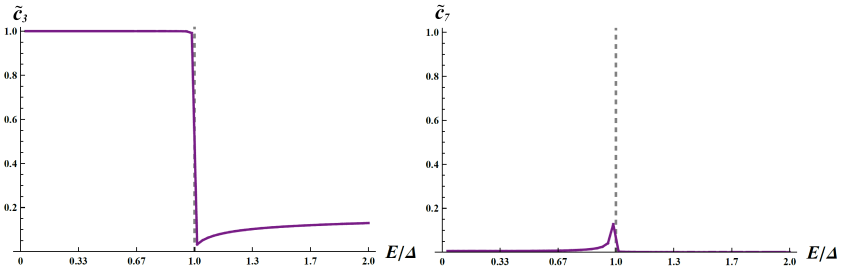

Figure 4.17: Non-zero reflection coefficients with $V_0 = 0$, fixed orientation $\theta_b = pi/2$, for positive energies in the range $E \in [0, 2\Delta_0]$ for an electron incoming from Weyl node with $C = -1$. Vertical grey-dashed lines are at $E = \Delta_0$.

$$\theta_b = 0 \, , V_0 = 0$$

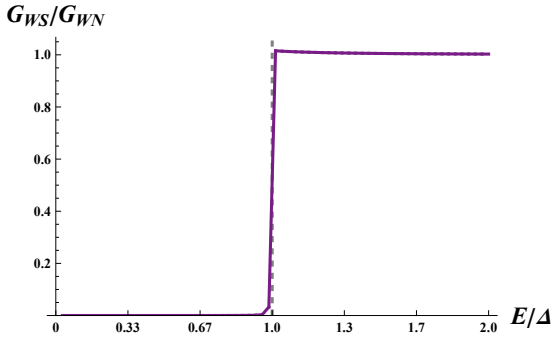

Figure 4.18: Normalized differential conductance G_{WS}/G_{WN} with $V_0 = 0$, fixed orientation $\theta_b = \pi/2$, for positive energies in the range $E \in [0, 2\Delta_0]$ for an electron incoming from Weyl node with $C = -1$. The vertical grey-dashed line is at $E = \Delta_0$.

It is evident that, also for this Weyl nodes orientation, the scenario is comparable to what was previously described for the other electron. Specifically, normal reflection at the same node ($\tilde{c}_3$) prevails, while Andreev reflection ($\tilde{c}_7$) is entirely suppressed at all energies, indicating that the chirality blockade is also effective in this case.

HOLE INCOMING FROM WEYL NODE WITH $C = 1$

In Figures 4.19 and 4.20 we plot the case of a hole incoming from the node with chirality $C = 1$, with $\theta_b = 0$. Also for this case of scattering, normal reflection (of a hole)

occurs at the opposite Weyl node ($\tilde{c}_7$) and the dominant process is Andreev reflection (of an electron), which occurs at the same node ($\tilde{c}_4$).

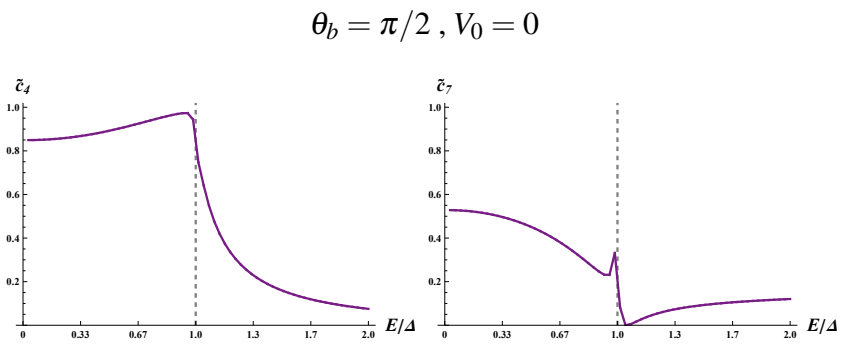

Figure 4.19: Non-zero coefficients with $V_0 = 0$, fixed orientation $\theta_b = 0$, for positive energies in the range $E \in [0, 2\Delta_0]$ for a hole incoming from Weyl node with $C = 1$. Vertical grey-dashed lines are at $E = \Delta_0$.

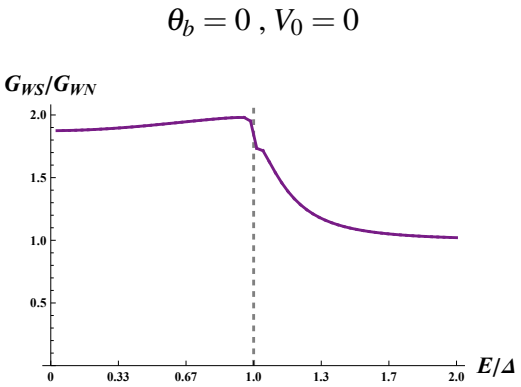

Figure 4.20: Normalized differential conductance G_{WS}/G_{WN} with $V_0 = 0$, fixed orientation $\theta_b = 0$, for positive energies in the range $E \in [0, 2\Delta_0]$ for hole incoming from Weyl node with $C = 1$. The vertical grey-dashed line is at $E = \Delta_0$.

Also for this case of scattering, normal reflection (of a hole) occurs at the opposite Weyl node ($\tilde{c}_7$) and the dominant process is Andreev reflection (of an electron), which occurs at the same node ($\tilde{c}_4$).

$$\theta_b = \pi/2 \, , V_0 = 0$$

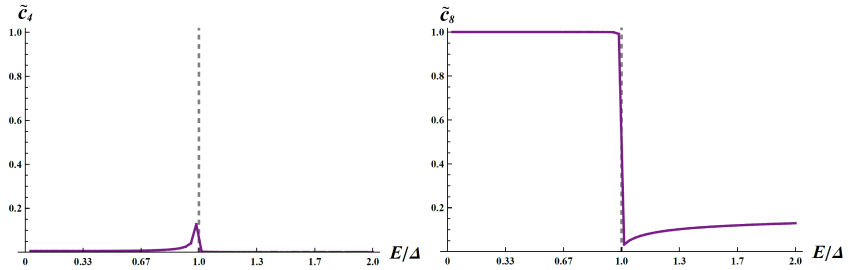

Figure 4.21: Non-zero reflection coefficients with $V_0 = 0$, fixed orientation $\theta_b = pi/2$, for positive energies in the range $E \in [0, 2\Delta_0]$ for a hole incoming from Weyl node with $C = 1$. Vertical grey-dashed lines are at $E = \Delta_0$.

$$\theta_b = 0 \, , V_0 = 0$$

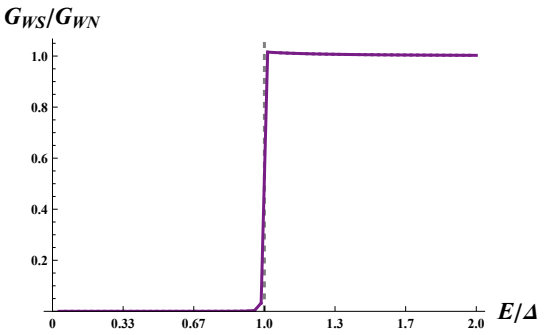

Figure 4.22: Normalized differential conductance G_{WS}/G_{WN} with $V_0 = 0$, fixed orientation $\theta_b = \pi/2$, for positive energies in the range $E \in [0, 2\Delta_0]$ for a hole incoming from Weyl node with $C = 1$. The vertical grey-dashed line is at $E = \Delta_0$.

For this incoming particle, we see from Figures 4.21 and 4.22 that in the $\theta_b = \pi/2$ orientation of Weyl nodes, normal reflection (of a hole) at the same node ($\tilde{c}_8$) prevails, while Andreev reflection ($\tilde{c}_4$) is completely suppressed at all energies, indicating that the chirality blockade has taken place.

HOLE INCOMING FROM WEYL NODE WITH $C = -1$

In Figures 4.23 and 4.24 we plot the coefficients for a hole incoming from the node with chirality $C = -1$. Again, normal reflection (of a hole) occurs at the opposite Weyl node ($\tilde{c}_8$) and the dominant process is Andreev reflection (of an electron), which occurs at the same node ($\tilde{c}_3$).

$$\theta_b = 0\ ,\ V_0 = 0$$

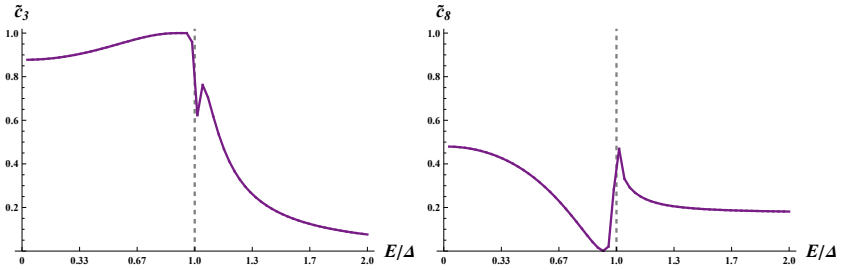

Figure 4.23: Non-zero coefficients with $V_0 = 0$, fixed orientation $\theta_b = 0$, for positive energies in the range $E \in [0, 2\Delta_0]$ for a hole incoming from Weyl node with $C = -1$. Vertical grey-dashed lines are at $E = \Delta_0$.

$$\theta_b = 0\ ,\ V_0 = 0$$

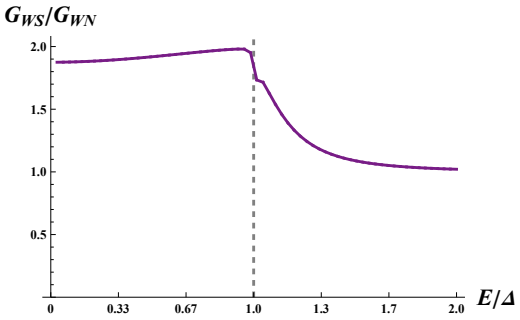

Figure 4.24: Normalized differential conductance G_{WS}/G_{WN} with $V_0 = 0$, fixed orientation $\theta_b = 0$, for positive energies in the range $E \in [0, 2\Delta_0]$ for hole incoming from Weyl node with $C = -1$. The vertical grey-dashed line is at $E = \Delta_0$.

In Figures 4.25 and 4.26 we plot the results for the $\theta_b = \pi/2$ case.

$$\theta_b = \pi/2\ ,\ V_0 = 0$$

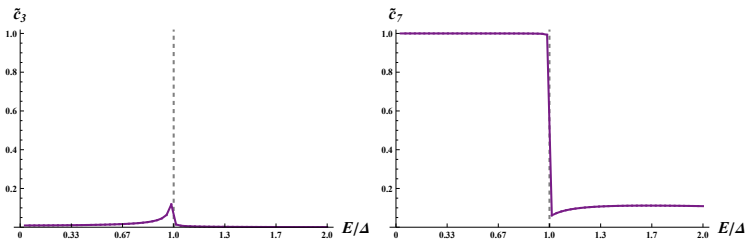

Figure 4.25: Non-zero reflection coefficients with $V_0 = 0$, fixed orientation $\theta_b = pi/2$, for positive energies in the range $E \in [0, 2\Delta_0]$ for a hole incoming from Weyl node with $C = 1$. Vertical grey-dashed lines are at $E = \Delta_0$.

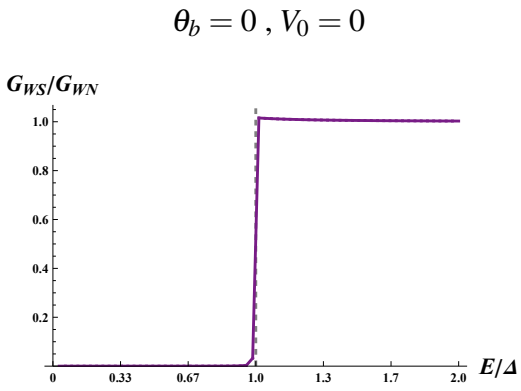

Figure 4.26: Normalized differential conductance G_{WS}/G_{WN} with $V_0 = 0$, fixed orientation $\theta_b = \pi/2$, for positive energies in the range $E \in [0, 2\Delta_0]$ for a hole incoming from Weyl node with $C = -1$. The vertical grey-dashed line is at $E = \Delta_0$.

For this particle, in the $\theta_b = \pi/2$ orientation of Weyl nodes, normal reflection (of a hole) at the same node ($\tilde{c}_7$) prevails, while Andreev reflection ($\tilde{c}_3$) is completely suppressed at all energies, indicating that the chirality blockade has taken place.

4.5 DIFFERENT TYPES OF SUPERCONDUCTOR PAIRINGS

In the most general case, we define the superconductor pairing matrix $\hat{\Delta}$ as an Hermitian 8×8 matrix that satisfies the electron-hole symmetry relation

$$v_y \sigma_y \hat{\Delta}^* v_y \sigma_y = -\hat{\Delta} \tag{4.21}$$

In choosing a form of the pairing matrix, we make the following additional assumptions:

1. $\hat{\Delta}$ anticommutes with v_z (so it is fully off-diagonal in the electron-hole degree of freedom).
2. $\hat{\Delta}$ is independent of the momentum perpendicular to the NS interface.
3. $\hat{\Delta}$ squares to a scalar Δ_0^2.

For example, under this notation, the spin-singlet pairing used in the initial (untransformed) basis is

$$\hat{\Delta} = \Delta_0 v_y \tau_0 \sigma_y \tag{4.22}$$

Table 4.3 shows a summary of the key results, as in those discussed earlier, based on various pairing matrices choices, for an electron incoming from the Weyl node with $C = 1$.

Pairing matrix (in the initial basis)	Dominant process at $\theta_b = 0$	Dominant process at $\theta_b = \pi/2$	Chirality Blockade
$\Delta_0 \nu_y \tau_x \sigma_y$	AR	NR	Yes
$\Delta_0 \nu_y \tau_z \sigma_y$	NR	NR	No
$\Delta_0 \nu_y \tau_y \sigma_x$	AR	NR	Yes
$\Delta_0 \nu_y \tau_y \sigma_z$	AR	NR	Yes
$\Delta_0 \nu_y \tau_y \sigma_y$	NR	NR	No

Table 4.3: Schematic view of the key results for different initial pairing matrices. AR = "Andreev Reflection" and NR = "Normal Reflection".

We note to the reader that we are considering the scenario of normal incidence only. Observe that for $\theta_b = \pi/2$, it appears that normal reflection is the only allowed reflection process. This is likely due to spin-momentum conservation, which prevents Andreev reflection from occurring, at this incidence angle. However, although Andreev reflection seems to always be suppressed for $\theta_b = \pi/2$, we only talk about chirality blockade when Andreev reflection is the dominant process for the opposite Weyl nodes orientation (i.e. $\theta_b = 0$). From Table 4.3, we can see that the chirality blockade does not occur for the pairing matrices $\Delta_0 \nu_y \tau_y \sigma_y$ and $\Delta_0 \nu_y \tau_z \sigma_y$. In particular, the latter is a *pseudoscalar* spin-singlet pairing, which is *not* inversion symmetric $\tau_x \hat{\Delta} \tau_x = \hat{\Delta}$, and since this is essentially the pairing used in [11], [16], and [22], this, as already pointed out by Bovenzi et al. [9], explains why no chirality blockade was obtained in these studies. Notice also that the pairings $\Delta_0 \nu_y \tau_y \sigma_x$ and $\Delta_0 \nu_y \tau_y \sigma_z$ are of *spin-triplet* type; however, they still display the chirality blockade effect. This type of pairing has found applications in Majorana physics and in quantum computation, as briefly described in the next section.

5

Conclusions and Future Works

This thesis explores the transport properties of a junction between a topological Weyl semimetal with broken time-reversal symmetry and a BCS superconductor. Our model extends the existing literature by generalizing the orientation of Weyl nodes relative to the junction interface and accounting for higher energy bands in the construction of the Transfer Matrix. Consequently, it is applicable to any junction system that has the same degrees of freedom.

Initially, we showed the results for the simpler scenario where the Weyl nodes are oriented perpendicular to the junction. This setup is anticipated to closely resemble the results of a normal metal/superconductor junction because of the comparable band structure. In fact, our results confirmed this alignment, validating the functionality of the model.

As a second major result, our model indicates that, as hypothesised by Bovenzi et al. [9], when the Weyl nodes are oriented parallel to the junction, a phenomenon called chirality blockade occurs. This implies that the probability of Andreev reflection vanishes across all energy ranges and interface impurity strengths, allowing only alternative scattering processes to occur. This was observed to hold true for all kinds of incoming particles, thereby reinforcing the result.

Due to the general structure of our framework, we could examine the probability of each scattering process across various intermediate angles of Weyl node orientations. This allowed us to define a novel quantity, previously unreported in the literature, referred to as the critical angle of orientation (of Weyl nodes). Beyond this angle, the Andreev reflection process becomes rapidly suppressed, thanks to the effect of the chirality blockade. Additionally, we presented a numerical plot illustrating the behaviour of this parameter for different interface potential strengths.

Given the considerable tunability of Weyl nodes orientation via a magnetizing field, demonstrated as experimentally feasible in Section 1.2.10, we anticipate our findings to have potential applications in spintronics and quantum information. Specifically, by altering the magnetization of the Weyl semimetal, one could "switch" on or off the Andreev reflection process, which is a spin-dependent process, thereby making such systems valuable for spintronics technology.

As a concluding remark, we presented a diagrammatic overview of the aforementioned results for various types of superconducting pairings, which were readily derived by simply modifying the pairing matrix in the superconductor segment of our model. This is particularly relevant for experiments, due to the diversity of pairings already observed in nature, but also links to the theoretical exploration of unconventional superconductivity, which has sustained considerable interest over the last years. In particular, we note that some of the pairings that we mentioned in Table 4.3 are of spin-triplet type, which have found recent interest in Majorana fermions physics and fault-tolerant quantum computing [29].

In this thesis, our analysis was restricted to the special case of particles hitting the junction at normal incidence. Consequently, our results should not be interpreted as representing transport properties in their entirety. Investigating the full spectrum of incidence angles might be the goal of our future research. Nevertheless, the scenario of normal incidence is expected to be the most influential on the transport properties, as indicated in [23] for a normal metal/superconductor junction.

A

Appendix

A.1 Steps to obtain the block-diagonalization of the Weyl Hamiltonian

Here we denote some steps to derive the transformed Hamiltonian in Eq. (3.6). Explicitly, we have that

$$\begin{aligned} H(\tilde{\mathbf{k}},\mathbf{b}) &= \Omega_{\theta(\mathbf{k})} H(\mathbf{k},\mathbf{b}) \Omega^{\dagger}_{\theta(\mathbf{k})} \\ &= \left[\cos\frac{\theta_{\mathbf{k}}}{2} - i\tau^{y}(\hat{\mathbf{b}}\cdot\sigma)\sin\frac{\theta_{\mathbf{k}}}{2}\right](\tau^{z}\sigma\cdot\mathbf{k} + m_0\tau^{x} + \sigma\cdot\mathbf{b})\left[\cos\frac{\theta_{\mathbf{k}}}{2} + i\tau^{y}(\hat{\mathbf{b}}\cdot\sigma)\sin\frac{\theta_{\mathbf{k}}}{2}\right] \end{aligned} \tag{A.1}$$

Let us break it down. The first term is

$$\cos^2\frac{\theta_{\mathbf{k}}}{2}(\tau^{z}\sigma\cdot\mathbf{k} + m_0\tau^{x} - \sigma\cdot\mathbf{b}) \tag{A.2}$$

Then we have the mixed terms,

$$
\begin{aligned}
&\left[i\tau^y(\hat{\mathbf{b}}\cdot\sigma),\tau^z(\sigma\cdot\mathbf{k})+m_0\tau^x-\sigma\cdot\mathbf{b}\right]\sin\frac{\theta_\mathbf{k}}{2}\cos\frac{\theta_\mathbf{k}}{2}\\
&=\left(i\tau^y\tau^z(\hat{\mathbf{b}}\cdot\sigma)(\sigma\cdot\mathbf{k})-i\tau^z\tau^y(\sigma\cdot\mathbf{k})(\hat{\mathbf{b}}\cdot\sigma)\right)\sin\frac{\theta_\mathbf{k}}{2}\cos\frac{\theta_\mathbf{k}}{2}\\
&\quad+im_0\left[\tau^y(\hat{\mathbf{b}}\cdot\sigma),\tau^x\right]\sin\frac{\theta_\mathbf{k}}{2}\cos\frac{\theta_\mathbf{k}}{2}-i\tau^y[(\hat{\mathbf{b}}\cdot\sigma),\sigma\cdot\mathbf{b}]\sin\frac{\theta_\mathbf{k}}{2}\cos\frac{\theta_\mathbf{k}}{2}\\
&=-\tau^x\{(\hat{\mathbf{b}}\cdot\sigma),(\sigma\cdot\mathbf{k})\}\sin\frac{\theta_\mathbf{k}}{2}\cos\frac{\theta_\mathbf{k}}{2}+2m_0\tau^z(\hat{\mathbf{b}}\cdot\sigma)\sin\frac{\theta_\mathbf{k}}{2}\cos\frac{\theta_\mathbf{k}}{2}\\
&=-2\tau^x(\hat{\mathbf{b}}\cdot\mathbf{k})\sin\frac{\theta_\mathbf{k}}{2}\cos\frac{\theta_\mathbf{k}}{2}+2m_0\tau^z(\hat{\mathbf{b}}\cdot\sigma)\sin\frac{\theta_\mathbf{k}}{2}\cos\frac{\theta_\mathbf{k}}{2}\\
&=-\tau^x(\hat{\mathbf{b}}\cdot\mathbf{k})\sin\theta_\mathbf{k}+m_0\tau^z(\hat{\mathbf{b}}\cdot\sigma)\sin\theta_\mathbf{k}
\end{aligned}
\tag{A.3}
$$

Finally, we have the three terms proportional to $\sin^2\frac{\theta_k}{2}$

$$
\begin{aligned}
&\tau^y(\hat{\mathbf{b}}\cdot\sigma)\tau^z(\sigma\cdot\mathbf{k})\tau^y(\hat{\mathbf{b}}\cdot\sigma)\sin^2\frac{\theta_\mathbf{k}}{2}\\
&=-\tau^z(\hat{\mathbf{b}}\cdot\sigma)(\sigma\cdot\mathbf{k})(\hat{\mathbf{b}}\cdot\sigma)\sin^2\frac{\theta_\mathbf{k}}{2}=-\tau^z(\hat{\mathbf{b}}\cdot\sigma)[(\hat{\mathbf{b}}\cdot\mathbf{k})+i(\mathbf{k}\times\hat{\mathbf{b}})\cdot\sigma]\sin^2\frac{\theta_\mathbf{k}}{2}\\
&=-\tau^z\{(\hat{\mathbf{b}}\cdot\sigma)(\hat{\mathbf{b}}\cdot\mathbf{k})+i[\hat{\mathbf{b}}\cdot(\mathbf{k}\times\hat{\mathbf{b}})+i[\hat{\mathbf{b}}\times(\mathbf{k}\times\hat{\mathbf{b}})]\cdot\sigma]\}\sin^2\frac{\theta_\mathbf{k}}{2}\\
&=-\tau^z\{(\hat{\mathbf{b}}\cdot\mathbf{k})(\hat{\mathbf{b}}\cdot\sigma)+[\hat{\mathbf{b}}\times(\hat{\mathbf{b}}\times\mathbf{k})]\cdot\sigma\}\sin^2\frac{\theta_\mathbf{k}}{2}\\
&=-\tau^z\{(\hat{\mathbf{b}}\cdot\mathbf{k})(\hat{\mathbf{b}}\cdot\sigma)+[\hat{\mathbf{b}}(\hat{\mathbf{b}}\cdot\mathbf{k})-\mathbf{k}]\cdot\sigma\}\sin^2\frac{\theta_\mathbf{k}}{2}\\
&=-\tau^z\{2(\hat{\mathbf{b}}\cdot\mathbf{k})(\hat{\mathbf{b}}\cdot\sigma)-(\mathbf{k}\cdot\sigma)\}\sin^2\frac{\theta_\mathbf{k}}{2}
\end{aligned}
\tag{A.4}
$$

and also the remaining two terms

$$
m_0\tau^y(\hat{\mathbf{b}}\cdot\sigma)\tau^x\tau^y(\hat{\mathbf{b}}\cdot\sigma)\sin^2\frac{\theta_\mathbf{k}}{2}=-m_0\tau^x(\hat{\mathbf{b}}\cdot\sigma)(\hat{\mathbf{b}}\cdot\sigma)\sin^2\frac{\theta_\mathbf{k}}{2}=-m_0\tau^x\sin^2\frac{\theta_\mathbf{k}}{2} \tag{A.5}
$$

and

$$
\tau^y(\hat{\mathbf{b}}\cdot\sigma)\sigma\cdot\mathbf{b}\tau^y(\hat{\mathbf{b}}\cdot\sigma)\sin^2\frac{\theta_\mathbf{k}}{2}=\sigma\cdot\mathbf{b}\sin^2\frac{\theta_\mathbf{k}}{2} \tag{A.6}
$$

Joining all the contributions, we obtain

$$\begin{aligned}\Omega_{\theta(\mathbf{k})}H(\mathbf{k},\mathbf{b})\Omega^{\dagger}_{\theta(\mathbf{k})} =& \cos^2\frac{\theta_{\mathbf{k}}}{2}\left(\tau^z\sigma\cdot\mathbf{k}+m_0\tau^x+\sigma\cdot\mathbf{b}\right)\\ &+\sin^2\frac{\theta_{\mathbf{k}}}{2}\left[-2\tau^z(\hat{\mathbf{b}}\cdot\mathbf{k})(\hat{\mathbf{b}}\cdot\sigma)+\tau^z(\mathbf{k}\cdot\sigma)-m_0\tau^x+\sigma\cdot\mathbf{b}\right]\\ &-\tau^x(\hat{\mathbf{b}}\cdot\mathbf{k})\sin\theta_{\mathbf{k}}+m_0\tau^z(\hat{\mathbf{b}}\cdot\sigma)\cos\theta_{\mathbf{k}}\end{aligned} \tag{A.7}$$

Simplifying

$$\begin{aligned}\Omega_{\theta(\mathbf{k})}H(\mathbf{k},\mathbf{b})]\Omega^{\dagger}_{\theta(\mathbf{k})} =& \tau^x\left[-m_0\cos\theta_{\mathbf{k}}-(\hat{\mathbf{b}}\cdot\mathbf{k})\cos\theta_{\mathbf{k}}\right]+\sigma\cdot\mathbf{b}\\ &+\tau^z\left[(\sigma\cdot\mathbf{k})-(\hat{\mathbf{b}}\cdot\mathbf{k})(\hat{\mathbf{b}}\cdot\sigma)\left(1+\cos\theta_{\mathbf{k}}\right)+m_0(\hat{\mathbf{b}}\cdot\sigma)\cos\theta_{\mathbf{k}}\right]\end{aligned} \tag{A.8}$$

From this we can go back to Eq. (3.6).

A.2 DIGRESSION ABOUT THE LINEAR TERM IN THE PROBABILITY CURRENT

In this section, we give an argument to why we did not include a linear term in the probability current.

The probability density function is in general given by

$$\rho(\mathbf{r},t)=\Psi^*(\mathbf{r},t)\Psi(\mathbf{r},t)=|\Psi(\mathbf{r},t)|^2. \tag{A.9}$$

which must satisfy the continuity equation:

$$\nabla\cdot\mathbf{j}+\frac{\partial|\Psi|^2}{\partial t}=0 \tag{A.10}$$

where $\mathbf{j}$ is the probability current.

For a generic Hamiltonian (in 1D for simplicity) of the form

$$H=\partial_z\hat{M}_2(z)\,\partial_z+i\hat{M}_1(z)\,\partial_z+const. \tag{A.11}$$

One obtains that

$$\begin{aligned}\partial_t \Psi \int dz \Psi^{+} \Psi &= \int dz \, (\Psi i H)^{\dagger} \Psi + \Psi^{+} (i H \Psi) \\ &= -i \int dz \Psi^{\dagger} \left[\underset{\leftarrow}{\partial_z} \hat{M}_2 \underset{\leftarrow}{\partial_z} - i \underset{\leftarrow}{\partial_z} \hat{M}_1 - \underset{\rightarrow}{\partial_z} \hat{M}_2 \underset{\rightarrow}{\partial_z} - i \hat{M}_1 \underset{\rightarrow}{\partial_z} \right] \Psi\end{aligned} \tag{A.12}$$

The linear term reads

$$- \int dz \Psi^{\dagger} \left[\underset{\leftarrow}{\partial_z} \hat{M}_1 + \hat{M}_1 \underset{\rightarrow}{\partial_z} \right] \Psi \tag{A.13}$$

Taking $\Psi \propto e^{i k_z z}$, this is

$$- \int dz \Psi^{\dagger} \left[-i k_z \hat{M}_1 + i \hat{M}_1 k_z \right] \Psi = 0 \tag{A.14}$$

Hence, the linear term will not contribute to the probability current, as we wanted to prove.

Note that if instead we take an Hamiltonian of the form

$$H' = \partial_z \hat{M}_2 (z) \, \partial_z + i \partial_z \hat{M}_1 (z) + const. \tag{A.15}$$

where now ∂_z also acts on the the space-dependent coefficient $\hat{M}_1$, the linear term would result in

$$- \int dz \Psi^{\dagger} \left[\hat{M}_1 \underset{\leftarrow}{\partial_z} + \underset{\rightarrow}{\partial_z} \hat{M}_1 \right] \Psi = - \int dz \Psi^{\dagger} \left[2 \partial_z \hat{M}_1 \right] \Psi \tag{A.16}$$

For coefficients of the form $\hat{M}_1 = \hat{M}_1^W \Theta(-z) + \hat{M}_1^S \Theta(z)$, this becomes

$$- \int dz \Psi^{\dagger} \left[2 \partial_z \hat{M}_1 \right] \Psi = - \int dz \Psi^{\dagger} \left[2 \delta(0) \left(\hat{M}_1^S - \hat{M}_1^W \right) \right] \Psi \tag{A.17}$$

Which is in general non-zero for $\hat{M}_1^S \neq \hat{M}_1^W$ and would break the conservation of probability density by adding a source term in the continuity equation. Therefore, in the main text, we discard this form and exploit the result obtained with Eq. (A.14).

A.3 EXPLICIT FORM OF THE UNITARITY OF THE CURRENT

We remind the reader that the second-order coefficient matrices are given by

$$\begin{aligned}\hat{M}_S^{(2)} &= \frac{v_z \tau_0 \sigma_0}{2m_S} \\ \hat{M}_W^{(2)} &= v_0 \tau_z \left[\frac{\cos^2\theta_b + g_m}{2m_0}\right](\sigma_z \cos\theta_b + \sigma_x \sin\theta_b)\end{aligned} \tag{A.18}$$

The first-order ones are not relevant for this section, since they do not appear in the probability current as explained in A.2. The current for each type of process (incoming, reflected or transmitted) can be re-written as

$$\mathbf{j}_i(z) = -\frac{i}{m} Im\left\{\Psi_i^\dagger(z)\hat{M}_2\partial_z\Psi_i(z)\right\} \tag{A.19}$$

where i is a generic index for identifying a particular process, and

$$\Psi_i(z) = c_i\psi_i\, e^{ik_i z} \tag{A.20}$$

We therefore obtain that

$$\mathbf{j}_i(0) = -\frac{iRe\{k_i\}|c_i|^2}{m}\left[\psi_i^\dagger \hat{M}_2 \psi_i\right] \tag{A.21}$$

Following the notation introduced in the Results section, the unitarity of the current is expressed by

$$1 = \frac{\mathbf{j}_{tot}^{out}(0)}{\mathbf{j}_{tot}^{inc}(0)} = \frac{\mathbf{j}_W^{refl}(0^-) + \mathbf{j}_S^{trans}(0^+)}{\mathbf{j}_W^{inc}(0^-) + \mathbf{j}_S^{inc}(0^+)} \tag{A.22}$$

With the use of Eq. (A.21), this becomes

$$1 = \frac{\sum_{i=1}^{8} Re\{k_i^W\}|c_i|^2\left[\psi_i^\dagger \hat{M}_2^W \psi_i\right] + \left(|u_0|^2 - |v_0|^2\right)\sum_{i=9}^{16} Re\{k_i^S\}|c_i|^2\left[\psi_i^\dagger \hat{M}_2^S \psi_i\right]}{\sum_{i=1}^{8} Re\left\{k_{inc,i}^W\right\}|a_i|^2\left[\psi_i^\dagger \hat{M}_2^W \psi_i\right] + \left(|u_0|^2 - |v_0|^2\right)\sum_{i=9}^{16} Re\left\{k_{inc,i}^S\right\}|a_i|^2\left[\psi_i^\dagger \hat{M}_2^S \psi_i\right]} \tag{A.23}$$

This allows us to define a new series of positive-definite coefficients

$$\tilde{c}_i = \sqrt{\left|\frac{Re\left\{k_{refl/trans,i}\right\}\,|c_i|^2}{\mathbf{j}_{tot}^{inc}(0)}\right|} \tag{A.24}$$

so the the unitarity of the current becomes

$$1 = \sum_{i=1}^{8} |\tilde{c}_i|^2 \frac{Sign\left(Re\left\{k_{refl,i}\right\}\right)}{Sign\left(\mathbf{j}_{tot}^{inc}(0)\right)} \left[\psi_i^{\dagger} \hat{M}_2^W \psi_i\right] + \left(|u_0|^2 - |v_0|^2\right) \sum_{i=9}^{16} |\tilde{c}_i|^2 \frac{Sign\left(Re\left\{k_{trans,i}\right\}\right)}{Sign\left(\mathbf{j}_{tot}^{inc}(0)\right)} \left[\psi_i^{\dagger} \hat{M}_2^S \psi_i\right] \tag{A.25}$$

In this way, we recovered the same form of the unitarity of the probability current as defined in the BTK model [8].

References

[1] N. P. Armitage, E. J. Mele, and Ashvin Vishwanath. "Weyl and Dirac semimetals in three-dimensional solids". In: *Rev. Mod. Phys.* 90 (1 Jan. 2018), p. 015001. DOI: 10.1103/RevModPhys.90.015001. URL: https://link.aps.org/doi/10.1103/RevModPhys.90.015001.

[2] C. W. J. Beenakker. "Colloquium: Andreev reflection and Klein tunneling in graphene". In: *Reviews of Modern Physics* 80.4 (Oct. 2008), pp. 1337–1354. DOI: 10.1103/revmodphys.80.1337. URL: https://doi.org/10.1103%2Frevmodphys.80.1337.

[3] C. W. J. Beenakker. "Specular Andreev Reflection in Graphene". In: *Physical Review Letters* 97.6 (Aug. 2006). DOI: 10.1103/physrevlett.97.067007. URL: https://doi.org/10.1103%2Fphysrevlett.97.067007.

[4] Ilya Belopolski et al. "Discovery of topological Weyl fermion lines and drumhead surface states in a room temperature magnet". In: *Science* 365.6459 (2019), pp. 1278–1281. ISSN: 0036-8075. DOI: 10.1126/science.aav2327. URL: https://science.sciencemag.org/content/365/6459/1278.

[5] B. Andrei Bernevig, Claudia Felser, and Haim Beidenkopf. "Progress and prospects in magnetic topological materials". In: *Nature* 603.7899 (Mar. 2022), pp. 41–51. ISSN: 1476-4687. DOI: 10.1038/s41586-021-04105-x. URL: http://dx.doi.org/10.1038/s41586-021-04105-x.

[6] B.A. Bernevig and T.L. Hughes. *Topological Insulators and Topological Superconductors*. Princeton University Press, 2013. ISBN: 9780691151755. URL: https://books.google.it/books?id=wOn7JHSSxrsC.

[7] G. E. Blonder and M. Tinkham. "Metallic to tunneling transition in Cu-Nb point contacts". In: *Phys. Rev. B* 27 (1 Jan. 1983), pp. 112–118. DOI: 10.1103/PhysRevB.27.112. URL: https://link.aps.org/doi/10.1103/PhysRevB.27.112.

[8] G. E. Blonder, M. Tinkham, and T. M. Klapwijk. “Transition from metallic to tunneling regimes in superconducting microconstrictions: Excess current, charge imbalance, and supercurrent conversion”. In: *Phys. Rev. B* 25 (7 Apr. 1982), pp. 4515–4532. DOI: 10.1103/PhysRevB.25.4515. URL: https://link.aps.org/doi/10.1103/PhysRevB.25.4515.

[9] N. Bovenzi et al. “Chirality blockade of Andreev reflection in a magnetic Weyl semimetal”. In: *Phys. Rev. B* 96 (3 July 2017), p. 035437. DOI: 10.1103/PhysRevB.96.035437. URL: https://link.aps.org/doi/10.1103/PhysRevB.96.035437.

[10] Ranran Cai et al. “Evidence for anisotropic spin-triplet Andreev reflection at the 2D van der Waals ferromagnet/superconductor interface”. In: *Nature Communications* 12.1 (Nov. 2021). ISSN: 2041-1723. DOI: 10.1038/s41467-021-27041-w. URL: http://dx.doi.org/10.1038/s41467-021-27041-w.

[11] Wei Chen et al. “Specular Andreev reflection in inversion-symmetric Weyl semimetals”. In: *Europhysics Letters* 103.2 (Aug. 2013), p. 27006. DOI: 10.1209/0295-5075/103/27006. URL: https://dx.doi.org/10.1209/0295-5075/103/27006.

[12] Gil Young Cho. “Possible topological phases of bulk magnetically doped Bi2Se3: turning a topological band insulator into the Weyl semimetal”. In: (2012). arXiv: 1110.1939. URL: https://arxiv.org/abs/1110.1939.

[13] F. Dolcini. *Lecture Notes on Andreev Reflection*. 2009. URL: https://gsfp.physi.uni-heidelberg.de/graddays_oktober_2009/content/en/zubehoer/anhaenge/dolcini/.

[14] Pallab Goswami and Sumanta Tewari. “Axionic field theory of (3+1)-dimensional Weyl semimetals”. In: *Physical Review B* 88.24 (Dec. 2013). DOI: 10.1103/physrevb.88.245107. URL: https://doi.org/10.1103%2Fphysrevb.88.245107.

[15] Satyaki Kar and Arun M. Jayannavar. “A Primer on Weyl Semimetals: Down the Discovery of Topological Phases”. In: *Asian Journal of Research and Reviews in Physics* (Feb. 2021), pp. 34–45. ISSN: 2582-5992. DOI: 10.9734/ajr2p/2021/v4i130136. URL: http://dx.doi.org/10.9734/ajr2p/2021/v4i130136.

[16] Udit Khanna et al. “Chiral nodes and oscillations in the Josephson current in Weyl semimetals”. In: *Phys. Rev. B* 93 (12 Mar. 2016), p. 121409. DOI: 10.1103/PhysRevB.93.121409. URL: https://link.aps.org/doi/10.1103/PhysRevB.93.121409.

[17] Udit Khanna et al. “Proximity-induced superconductivity in Weyl semimetals”. In: *Physical Review B* 90.19 (Nov. 2014). DOI: 10.1103/physrevb.90.195430. URL: https://doi.org/10.1103%2Fphysrevb.90.195430.

[18] Mikito Koshino and Intan Fatimah Hizbullah. “Magnetic susceptibility in three-dimensional nodal semimetals”. In: *Phys. Rev. B* 93 (4 Jan. 2016), p. 045201. DOI: 10.1103/PhysRevB.93.045201. URL: https://link.aps.org/doi/10.1103/PhysRevB.93.045201.

[19] R.M. Lima and H.R. Christiansen. “The kinetic Hamiltonian with position-dependent mass”. In: *Physica E: Low-dimensional Systems and Nanostructures* (2023). DOI: 10.1016/j.physe.2023.115688. URL: http://dx.doi.org/10.1016/j.physe.2023.115688.

[20] Hongshuang Liu et al. “Ideal spin-polarized Weyl half-semimetal with a single pair of Weyl points in the half-Heusler compounds XCrTe (X = K, Rb)”. In: *Phys. Rev. B* 109 (17 May 2024), p. 174426. DOI: 10.1103/PhysRevB.109.174426. URL: https://link.aps.org/doi/10.1103/PhysRevB.109.174426.

[21] Junwei Liu, Chen Fang, and Liang Fu. *Tunable Weyl fermions and Fermi arcs in magnetized topological crystalline insulators*. 2016. DOI: 10.48550/ARXIV.1604.03947. URL: https://arxiv.org/abs/1604.03947.

[22] Kevin A. Madsen, Emil J. Bergholtz, and Piet W. Brouwer. “Josephson effect in a Weyl SNS junction”. In: *Phys. Rev. B* 95 (6 Feb. 2017), p. 064511. DOI: 10.1103/PhysRevB.95.064511. URL: https://link.aps.org/doi/10.1103/PhysRevB.95.064511.

[23] Niels Asger Mortensen, Karsten Flensberg, and Antti-Pekka Jauho. “Angle dependence of Andreev scattering at semiconductorsuperconductor interfaces”. In: *Physical Review B* 59.15 (Apr. 1999), pp. 10176–10182. DOI: 10.1103/physrevb.59.10176. URL: https://doi.org/10.1103%2Fphysrevb.59.10176.

[24] Shuichi Murakami et al. “Emergence of topological semimetals in gap closing in semiconductors without inversion symmetry”. In: *Science Advances* 3.5 (May 2017). ISSN: 2375-2548. DOI: 10.1126/sciadv.1602680. URL: http://dx.doi.org/10.1126/sciadv.1602680.

[25] H.B. Nielsen and M. Ninomiya. “A no-go theorem for regularizing chiral fermions”. In: *Physics Letters B* 105.2 (1981), pp. 219–223. ISSN: 0370-2693. DOI: https://doi.org/10.1016/0370-2693(81)91026-1. URL: https://www.sciencedirect.com/science/article/pii/0370269381910261.

[26] K. S. Novoselov et al. “Electric Field Effect in Atomically Thin Carbon Films”. In: *Science* 306.5696 (Oct. 2004), pp. 666–669. ISSN: 1095-9203. DOI: 10.1126/science.1102896. URL: http://dx.doi.org/10.1126/science.1102896.

[27] Michael Edward Peskin and Daniel V. Schroeder. *An Introduction to Quantum Field Theory*. Reading, USA: Addison-Wesley (1995) 842 p. Westview Press, 1995.

[28] Xiao-Liang Qi, Taylor L. Hughes, and Shou-Cheng Zhang. “Topological field theory of time-reversal invariant insulators”. In: *Phys. Rev. B* 78 (19 Nov. 2008), p. 195424. DOI: 10.1103/PhysRevB.78.195424. URL: https://link.aps.org/doi/10.1103/PhysRevB.78.195424.

[29] Masatoshi Sato and Yoichi Ando. “Topological superconductors: a review”. In: *Reports on Progress in Physics* 80.7 (May 2017), p. 076501. DOI: 10.1088/1361-6633/aa6ac7. URL: https://dx.doi.org/10.1088/1361-6633/aa6ac7.

[30] Michael Tinkham. *Introduction to Superconductivity*. 2nd ed. Dover Publications, June 2004. ISBN: 0486435032. URL: http://www.worldcat.org/isbn/0486435032.

[31] Maximilian Trescher. “Tilted Weyl Semimetals”. Dissertation. 2018. URL: http://dx.doi.org/10.17169/refubium-46.

[32] Shuhei Uchida, Tetsuro Habe, and Yasuhiro Asano. “Andreev Reflection in Weyl Semimetals”. In: *Journal of the Physical Society of Japan* 83.6 (June 2014), p. 064711. DOI: 10.7566/jpsj.83.064711. URL: https://doi.org/10.7566%2Fjpsj.83.064711.

[33] Kentaro Ueda et al. “Spontaneous Hall effect in the Weyl semimetal candidate of all-in all-out pyrochlore iridate”. In: *Nature Communications* 9 (Aug. 2018). DOI: 10.1038/s41467-018-05530-9.

[34] Wikipedia. “DOS materials”. In: (). URL: https://commons.wikimedia.org/wiki/File:Band_filling_diagram.svg.

[35] Edward Witten. “Three Lectures On Topological Phases Of Matter”. In: *Riv. del Nuovo Cim.* 39 (2015), pp. 313–370. DOI: 10.1393/ncr/i2016-10125-3.

[36] J.X. Zhu. *Bogoliubov-de Gennes Method and Its Applications*. Lecture Notes in Physics. Springer International Publishing, 2016. ISBN: 9783319313146. URL: https://books.google.se/books?id=Tep6DAAAQBAJ.